OPTO-THERMAL MICRO-TRANSPORTATION FOR CELLULAR MICROBIOLOGY

A DISSERTATION SUBMITTED TO THE GRADUATE DIVISION OF THE UNIVERSITY OF HAWAIʻI AT MĀNOA IN PARTIAL FULFILLMENT OF THE REQUIREMENTS FOR THE DEGREE OF

DOCTOR OF PHILOSOPHY

IN

ELECTRICAL ENGINEERING

MAY 2014

By

Wenqi Hu

Dissertation Committee:

Aaron Ohta, Chairperson
Wayne Shiroma
Victor Lubecke
Olga Boric-Lubecke
John Allen

Keywords : Bubble, Micro-transportation, Thermocapillary, Optical

ACKNOWLEDGEMENT

First, I have to express gratitude to my advisor Dr. Aaron Ohta. During last five year, Dr. Ohta permited me maximum freedom in my research; meanwhile, he was always ready for offering invaluable guidance. Such mentorship allowed me to try every possibility, and then being aided by him to condense my results to useful knowledge. In addition, I have to thank Dr. Wayne Shiroma for recommending me to Dr. Ohta as a graduate assistant, and allowing me to use anything in his lab. I would also like to acknowledge Dr. Victor Lubecke, Dr. John Allen and Dr. Olga-Boric Lubecke for their constructive advice to my dissertation.

To my colleagues at the UH Microdevices & Microfluidics Lab (Swapnil Namekar, Alexander Nicholas, Michael C. Hagenow) and at the MMRL Lab (Junlei Bao, Wade Tonaki, Ryan Gough, Andy Morishita, Jonathan Dang), I have to thank you for the support on the every detail of my research. I especially have to acknowledge Ashley Fan for the help in cell culturing, and Kelly Ishii for being the teammate on both 2011 and 2012 Microrobotic Competitions. It was all because of this competition that I started the research on cellular micro-transportation.

At last, I am particularly grateful to my parents. As the only child, it must be challenging for them to allow me to study aboard. I also have to thank my wife for understanding me to get up during the midnight to check the proliferation of my cell. As a life-long friend and economist, her perspective constantly refreshes my rigid mind stalled in experiment. The talk with her greatly refines my publication, conference presentation and the dissertation.

ABSTRACT

Cellular microbiology requires a tool that can efficiently transport biological micro-objects, including single cells, cell clusters, microbeads and microscale hydrogels (microgels) laden with cells or chemicals. The transportation of these micro-objects is useful in many areas such as single-cell research and the construction of *in vitro* artificial tissue. In this dissertation, opto-thermocapillary flow-addressed bubbles (OFB) are evaluated for transporting biological micro-objects. Control over the OFB was accomplished by developing an engineered free-space optical addressing system. The OFB provides a new micro-transportation tool for cellular microbiology. It complements other cell-manipulation technologies such as optical tweezers and dielectrophoresis (DEP), as it is less dependent upon the optical and electrical properties of the working environment, enabling functionality in cell culture media. OFB also distinguishes itself by the capability for on-demand creation of micro-transporters, eliminating the need for microfabricated micro-transporters that need to be introduced into the working space. Further, the straightforward actuation mechanism of OFB enables parallel and cooperative micro-transportation using commercial beam-forming devices.

OFBs with varying dimensions were used to transport biological micro-objects such as microbeads, single cells, and cell-laden microgels. The micro-objects were patterned into different geometries to show the potential applications for engineering artificial tissue. The results of each transportation was subjected to viability tests or subsequent cell culturing to check the effects on the biological micro-objects. High cell viability rates were observed, showing OFB is a dexterous and reliable biological micro-transportation tool.

CONTENTS

LIST OF FIGURES

LIST OF TABLES

CHAPTER. 1 BIO-MICRO-TRANSPORTATION AND OPTO-THERMOCAPILLARY FLOW-ADDRESSED BUBBLE

1.1 PROGRAMMABLE BIO-MICRO-TRANSPORTATION

Cellular scale bio-micro-transportation focuses on the spatial transfer of bio-micro-objects with dimensions ranging from 1 μm to 1 mm in liquid media. The bio-objects within this range cover single cells [1], microparticles with various dimensions and functional surfaces [2], cell spheroids [3], microorganisms [4] and micro-capsules containing drugs [1]. Bio-micro-transportation has many applications in cellular-scale research [5] and tissue engineering research [6].

Bio-micro-transportation can finish two major operations in the cellular-scale research. In the first one, particular bio-micro-object of interest can be transported. This is useful for isolating rare or valuable cells for further analysis or culturing [5]. Besides this, micro-transportation of other bio-objects are also of interest. For example, the delivery of chemical-laden microcapsules by a micro-transportation tool to specific neural cells can be used to study the response of the neural cell network [7]. In the second operation, micro-transportation can also rearrange bio-micro-objects into desired locations. Such operation is helpful in decoding the relations between objects. For, example, patterning two cells next to each other makes it possible to examine intercellular signaling [5][8].

In addition to cellular-scale research, micro-transportation can also be used to create *in vitro* (outside living organism) tissue models for drug development. Currently, the drug development process is long, expensive, and has ethical issues such as animal testing. These problems are partly due to the imprecise cell assay models and animal models used for evaluating drugs designed for humans [9][10]. This motivates the research of *in vitro* tissue models, which can accurately represent their *in vivo* (inside living organism) counterparts [11], as this will help to streamline the drug discovery process by providing more accurate, inexpensive models that can potentially replace cell assays and animal testing. One way to create such *in vitro* functional tissue is to pattern cell-laden gels with dimensions from 100 μm to 1 mm [12]. In this method, cells of the same type are first grouped in cured microscale hydrogels (microgels) [3]. The hydrogel serves as the extracellular matrix (ECM), and is made from natural materials such as

collagen, agarose, and alginate, or synthetic polymers, such as gelatin methacrylate (GelMA) and polyethylene glycol diacrylate (PEGDA) [13]. After being enclosed in microgels, cells can grow in three dimensions, just as growth occurs *in vivo*. The cell-laden microgels can then be patterned into predefined geometries and cultured, eventually achieving functional tissues [6]. Although other methods are available to pattern cells [14][15][16][17], micro-transportation has its own advantages, such as accuracy and programmability, making it suitable for laboratory applications and rapid prototyping.

1.2 CURRENT BIO-MICRO-TRANSPORTATION TOOLS

1.2.1 INTRODUCTION

In micro-transportation, high throughput and accuracy are desired. The micro-transportation of bio-micro-objects imposes even more demands. Firstly, the actuation mechanism should be bio-friendly. The material in physical contact with the bio-objects should be bio-compatible, and the optical, magnetic, or electrical fields penetrating through the bio-objects should be within safe levels. Secondly, the micro-transportation has to function in liquids, as this is the native environment for bio-objects, especially cells. This is of increased concern for electrically based actuation mechanisms, as the conductive nature of many media such as phosphate buffer saline (PBS) and Dulbecco's Modified Eagle Medium (DMEM) can be problematic.

The most basic bio-micro-transportation tool is the manual micromanipulator [18]. Other micro-transportation tools relying on various physics have since been developed, with the goals of increasing efficiency, resolution, and the level of automation. Some of these micro-transportation tools, such as optical tweezers [19] and magnetic tweezers [20], rely on one physical field, while others, such optoelectronic tweezers (OET) [21], may hybridize the features of multiple fields. These tools can be categorized into the following six types, according to the force that immediately affects the bio-object during micro-transportation: magnetic, optical radiation pressure, dielectrophoresis, physical contact, acoustic, and hydrodynamic.

1.2.2 MAGNETIC FORCE

Strong magnetic fields can penetrate most bio-samples and their surrounding media without being disturbed, and with little safety issues [22]. To be transported by a

magnetic field, the bio-object has to be intrinsically magnetic [23]. Only a handful of bacteria types are magnetotatic, meaning that they contain magnetic material, and have been transported [24].

A variety of magnetic particles are available commercially [2] and can be transported directly by magnetic field. This method is referred as magnetic tweezers [20]. Usually, a magnetized microscale probe is attached to macroscale controller to wirelessly address the magnetic beads in the working space (the volume in which the micro-transportation occurs). These beads can be attached directly to cells and doped into microgels to make micro-transportation, or physically stretch cells to test their mechanical properties [20][25]. These topics are classified as physical contact micro-transportation and discussed more in Section 1.2.5.

1.2.3 OPTICAL RADIATION PRESSURE

Optical radiation pressure can be used to transport micro-objects [26]. The force direction resulting from radiation pressure depends on the refractive index contrast of the objects and surrounding medium as well as the intensity of the laser beam. A large contrast in refractive index and an intense laser yields stronger force, at the expense of increased photo-damage to cells under manipulation [27]. Forces of approximately 400 pN have been generated by optical macro-tweezers [28], which uses counter-propagating beams with the help of spatial light modulator (SLM) and a mirror on the other side of the working space [29]. This tool is able to trap objects outside the focal point of the beam with relatively lower laser intensity. Micro-objects from 50 to 100 μm, such as highly motile micro-organisms, potato-starch granules, and cell clusters have been successfully trapped in 3D [28].

Optical tweezers, which creates a 3D radiation-pressure trap from a single laser beam, has been widely used to transport single cells [19][30][31] and microstructures [32][33][34]. Such a trap is usually realized with an objective lens with high magnification and numerical aperture (N.A.). For example, a lens with 100X magnification and an N.A. of 1.3 was used in ref. [19]. As a way to circumvent the harmful direct laser radiation (discussed further in Section 1.2.5), microstructures, also referred as optical microtools in literature [32][33], can also be addressed by the optical tweezers and used to transport micro-objects. Multiple optical traps can also increase the transportation throughput. To achieve this, a scanning mirror can periodically

redirect the laser beam to different positions [35]. Alternatively, a spatial light modulator (SLM) can split light beams into multiple focal points using a hologram, allowing optical tweezers to independently address tens of cells at once to form various geometries [19].

1.2.4 DIELECTROPHORESIS FORCE

Dielectrophoresis (DEP) relies Coulombic force on a dipole in the presence of an electrical field gradient [36]. The force direction and strength depends on the electrical field frequency and the dielectric properties of both the micro-objects and surrounding medium. Thus, constant electric field gradients have been created by various microfabricated electrodes, realizing cellular micro-transportation [37][38]. To achieve programmable 2D transportation, electrical signals can be sent to these electrodes to dynamically modulate the electrical field gradient [36]. Using this method, various modulation schemes have been reported to transport single cells in parallel, such as independently addressed electrodes [39], and moving pulsed DEP [40].

To simplify the device fabrication process by eliminating the microfabricated electrodes, light can be used to modulate the electrical field, as in optoelectronic tweezers (OET) [21]. OET combines the advantages of light actuation and DEP. In OET, the substrate is optoelectronic semiconductor material such as amorphous silicon (α-Si) or titanium oxide phthalocyanine (TiOPc) [41]. Light illumination tunes the local electrical conductivity of the substrate, creating an electric field gradient in the medium that generates DEP force on nearby micro-objects. Since the light only acts as a control signal, non-coherent light is enough to function the mechanism. Using the micromirrors inside an off-the-shelf projector, it is possible to use OET to transport a massive number of cells independently and in parallel [42].

AC electric fields are generally used for DEP to prevent electrolysis, yet the potential hazards of Joule heating of the liquid medium and the electrical field penetration into the bio-micro-objects are intrinsic and cannot be circumvented [43]. Furthermore, the dependence on the dielectric properties mean that control parameters or the working space must be optimized for different micro-objects and different media. This is of increased importance to OET, as the media conductivity should be kept much lower than that of the standard cell culture media [44]. Modification of the substrate with

phototransistor arrays can resolve this issue, but at the expense of using a more complicated micro-fabrication process [45].

1.2.5 PHYSICAL CONTACT

Direct physical contact micro-transportation was first realized by a micromanipulator with microscale probe attached to macroscale mechanical controller [18]. The macroscale mechanical controller is manually operated tool such as Vernier meter; even when used by a skilled technician, the throughput is limited [18]. However, the control and actuation of micromanipulator can be automated, reducing the time and labor required to perform micro-transportation tasks [46]. Micromanipulators have been used to place tissue engineering scaffolds [46] and single cells into specific locations [47]. As long as there is sufficient working space, several micromanipulators can also work together to increase the throughput and degrees of freedom (DOF) in the system [48].

To deploy more micro-transportation tools in the working space, the bulky physical connections between the macroscale and microscale can be replaced. As mentioned in Section 1.2.2, magnetic fields are a suitable wireless control mechanism. Permanent magnets [49] or electromagnets [50] can create large magnetic forces or magnetic field gradients, and have been used to address magnetized microstructure [50]. These microstructures are referred as magnetic microrobots in the literature [50]. Their actuation mechanisms include stick-slip walking (crawling) [51] [52], gradient pulling [53] [54], and swimming [55]. Since the magnetic actuation is inherently unstable [56], accurate motion requires careful design of the microrobot and control system. Feedback control usually helps the microrobot move at well-controlled velocities of tens of millimeters per second [50] [52]. However, it is challenging to modulate the field of macroscale magnets for control of parallel and independent microscale magnetic traps [50]. Thus, parallel and independent addressing of multiple magnetic microrobots usually requires distinct fabricated features on each end-effector, enabling unique responses to complex control signals [57][52]. The complexity of the control system increases when more microrobots are deployed, limiting the overall system throughput. Although microscale coils array can generate localized magnetic fields and possibly can address multiple microrobots, the micro-fabrication is non-trivial [58].

As mentioned in Section 1.2.3, light can be easily split into multiple independent yet parallel focal points. Thus, optical radiation traps can replace the magnetic field to

address the issue of parallel transportation, Microstructures, which are also referred as optical microtools, made of patterned SU-8 [32], self-assembled beads [33][34], or thermally gelled polymer [59], have been actuated by multi-beam optical tweezers to transport bio-micro-objects. However, the parallel manipulation of optical microtools is limited by the tight laser focusing of optical tweezers, which is typically achieved by 100X objective lens with a numerical aperture of 1.4 [34]. This restricts the working space to an area smaller than 0.01 mm^2, which is smaller than the footprint of a single cell-laden microgel[17].

Another physical-contact micro-transportation tool under development is bacteria such as *Serratia marcescens*. Microbeads have been transported through the chemotactic response of the bacteria [60]. These bacterial micro-transporters have the potential to draw power from the nutrients in the surrounding medium. To transport larger objects, a microstructure was covered with many bacteria to form microbiorobots (MBR) [61]. The motion control of the MBRs relies on the galvanotaxis of the bacteria as it responds to the DC electric field in the medium.

Most physical contact transportation tools require some micro-fabrication. Further, microstructures or chemicals added to enable these micro-transportation methods may be contaminants during subsequent processes, especially since many microstructures are required for parallel transportation. Moreover, surface forces means that stiction of microscale objects is a serious problem in physical contact transportation, and can prevent the release of the micro-objects from the manipulator [62]. Vibration or electrostatic forces are sometimes necessary to shake the micro-objects off from the end-effectors. At last, it also has to be mentioned that the physical contact has the possibility of mechanical damage to the micro-object [63].

1.2.6 ACOUSTIC FORCE

Micro-transportation with resolution down to a single cell is possible with acoustic interference patterns from surface acoustic waves (SAW) [4]. Acoustic waves are generated by a transducer micro-fabricated on surface of the substrate. Although tunable patterning of multiple cells is possible [64], independent parallel micro-transportation of multiple micro-objects has not been demonstrated.

A bubble actuated by electrowetting was used to transport micro-objects directly [65]. To improve the transportation efficiency, acoustic radiation force, also known as the Bjerknes force, was introduced around gas bubbles by vibrating piezoelectric elements [66][67] or AC electrowetting [68]. By carefully tuning the frequency, the acoustic radiation force can trap micro-objects around the bubble. Besides electrowetting, micro-transportation using this mechanism can also be achieved by moving the bubble using a traversing rod tip [67]. This vibrating bubble mechanism is better at trapping larger particles, with diameters greater than 50 μm [69]. Currently, only beads [67][68][66], fish eggs [66][67][70], microorganisms [67][66] and groups of cells [71] have been trapped and transported. The resolution of this transportation mechanism must be increased further to accurately transport single cells, which are on the order of 10 μm in diameter. The fluidic flow around an acoustically excited bubble can also transport micro-objects like a conveyor, yet without showing to pattern micro-objects into arbitrary geometry [69].

1.2.7 HYDRODYNAMIC FORCE

Since the bio-micro-objects are in liquid media, another way to accomplish micro-transportation is to generate fluid flow to drag these micro-objects. Like physical contact micro-transportation, this method also has minimal reliance on the electrical and optical properties of the micro-objects.

The simplest way to generate hydrodynamic flow is through the movement of microstructures [62][72]. For example, the fluidic flow can be localized around a magnetic microrobot [62] or flows can intersect with each other to form a transport path [72][73]. Since the fluidic flow generated by different microstructures can be independent from each other, this mechanism may be used to transport micro-objects in parallel.

1.2.8 SUMMARY AND PROBLEM STATEMENT

In order to better transport biological micro-objects, especially for single-cell research and *in vitro* tissue engineering, a micro-transportation tool is preferred to have the least adverse biological effects. Magnetic, optical, and electrical mechanisms rely on the corresponding properties of the micro-objects, placing restrictions on the objects that can be transported and the maximum transportation force, due to the threat of

overexposure to hazardous fields. Thus, when transporting biological micro-objects, it is desirable to have tools that rely only on the mechanical properties of the objects.

Table 1 Major transportation tools relying on only the mechanical properties of the micro-objects. OFB related properties are marked in red.

Tool	Force	Parallel & independent transportation		Micro-fabrication	
		Number of parallel transporters demonstrated	Adding transporters increases control system complexity?	Number of micro-structures deployed	Micro-fabrication of the working space
Micro-manipulator [18][48]	Physical contact	Up to 4	Yes	Varies	None
Magnetic microrobots[50]		Up to 4	Yes	Multiple	None
Optical microtools [32][34]		Up to 2	No	Multiple	None
OFB		Up to 8	No	None	Single step
Bacteria microrobot [60][61]		1	Yes	Multiple	None
Acoustically excited bubble[66] [67][75] [69][71] [68]	Acoustic force	1	Yes	None	Multiple steps
SAW [4] [64]		N/A*	N/A	None	Multiple steps
Fluid flow around magnetic microrobots [62][72]	Hydrodynamic force	1	Yes	Multiple	None
Fluid flow around OFB		Up to 8	No	None	Single step
* Parallel transportation by SAW has been demonstrated, but the relative position of each micro-object is not independent of one another; it depends on the acoustic interference pattern.					

Table 1 summarizes the features of the mechanism relying only on the mechanical properties of the micro-objects. By using microstructure for direct physical contact, a wider selection of micro-objects can be transported, although this necessitates microfabrication and the potential contamination of the working space with microstructures. Of the physical contact transportation methods, acoustically excited bubbles and SAW demonstrate flexibility, but currently do not have single-cell resolution. Thus, the hydrodynamic flow generated by magnetic microrobot is currently an attractive method for transporting single cells. However, massive parallel

transportation is currently limited, as control of multiple magnetic microrobots is a complex problem, as mentioned in Section 1.2.5.

To address the problems and unify the advantages of these physical contact mechanisms, an opto-thermocapillary flow-addressed bubble, abbreviated as OFB hereafter, was developed as a micro-transportation tool. It accomplishes micro-transportation using either physical contact or hydrodynamic force. Hereafter, these two mechanisms are referred to as contact (physical contact) and non-contact (hydrodynamic force) micro-transportation. By using these two mechanisms, the OFB micro-transportation is agnostic to the electrical, optical, or magnetic properties of micro-objects. This makes OFB transportation applicable to a variety of bio-micro-objects, including microbeads, single cells, and microgels. At the same time, OFB actuation avoids excessive fabrication and wiring of the working space, permitting better interfacing with the current cellular microbiology protocols, such as cell culturing in enclosed plates, petri dishes, and flasks. At last, the optical control means that it is straightforward to realize parallel and independent transportation, potentially increasing the system throughput and enabling cooperative operations. In summary, with minimum microfabrication, the OFB can be used to transport bio-micro-objects with a wide size distribution in physiological medium. It is especially suitable for patterning small-scale micro-objects in ECM pre-polymers for single-cell and tissue engineering research.

1.3 OPTO-THERMOCAPILLARY FLOW-ADDRESSED BUBBLES (OFB)

1.3.1 INTRODUCTION

The gas bubble that is the heart of the OFB manipulator is well-suited to liquid media, since micro-scale cavitation bubbles can be generated on-demand through electrolysis [66] and laser absorption [74]. Bubbles have been previously transported by electrowetting [75] and DEP [76], but compared to these two mechanisms, the OFB can realize independent parallel and cooperative transportation by commercial light-beam-shaping devices, without complicated micro-fabrication. Thus, OFB can be integrated with current cell culture containers.

Gas bubbles can also be addressed by optical radiation pressure [77]. Compared to this, the OFB distinguishes itself by two features. First, the bubble has a lower refractive index than the surrounding medium, so optical radiation pressure repels bubbles from the regions of high laser intensity [78]. Thus, special techniques have to be designed to trap bubbles using optical radiation pressure [77]. As discussed later, the temperature derivative of surface tension of many liquid/gas interfaces, especially water/air, is negative [79]. Thus, OFB provides a mechanism for trapping bubbles at regions of high laser intensity, simplifying both the transportation mechanism and the optical setup. Secondly, unlike optical tweezers, opto-thermocapillary transportation has controllable thermocapillary flow around bubbles. As shown later, this fluidic flow can be utilized for non-contact micro-transportation.

1.3.2 THERMOCAPILLARY FLOW

As thermocapillary flow is the underlying actuation mechanism of the OFB, this section reviews this phenomenon.

The boundary condition on the gas/liquid interface for the Navier-Stokes equation can be described as [80][81]:

$$\eta(\partial u/\partial \boldsymbol{n}) = \gamma_T(\partial T/\partial \boldsymbol{t}) \qquad \text{Equation 1-1}$$

In Equation 1-1, $\boldsymbol{n}$ and $\boldsymbol{t}$ are the unit vector normal and tangent to the interface, respectively; η is the dynamic viscosity; u is the tangential component of the fluid velocity vector at the liquid/air interface; T is the temperature; γ_T is the derivative of the surface tension with respect to temperature, and γ is the surface tension.

The presence of a temperature gradient at the gas/liquid interface generates shear stress. This shear stress causes a fluid flow for the fluid near the interface. For an air/silicone oil interface and an air/water interface, the temperature derivative of surface tension γ_T is negative [79], which means liquid flows from hotter to cooler regions. Thus, if a bubble is present inside fluidic chamber with a linear temperature gradient, the bubble moves to the hotter region [82]. If the temperature gradient consists of a hot spot on the floor of a fluidic chamber, the bubble will try to center itself above the hot spot to

balance the temperature gradient on its surface. This results in a stable trapping of the bubble. If the hot spot moves, the bubble follows its movement.

1.3.3 CURRENT DEVELOPMENT OF OFB

This dissertation describes the development and implementation of OFB as a micro-transporter system for bio-objects. However, there is some prior fundamental work in opto-thermocapillary bubble actuation that should be mentioned.

Ivanova et al. used a diode laser (power: 20 mW, wavelength: 659 nm) to address bubbles with diameters from 200 µm to 1.2 mm through thermocapillary flow [83]. In their setup, the bubble was confined in a fluidic chamber (height: 50 µm) filled with a mixture of ethanol and brilliant green dye. The green dye was used to absorb the light energy.

OFB was first realized in a fluidic chamber (height: 100 µm) filled with silicone oil (Dow Corning 200® fluid) [84]. The fluidic chamber used an optically absorbent substrate to covert light energy into heat. By using a laser (power: 10 mW, wavelength: 635 nm), bubbles with diameters of approximately 100 µm were actuated at over 1 mm/s.

Oshemkov *et al*. later showed a femtosecond laser (average power: 20 mW, pulse duration: 200 fs) operating at a high repetition rate could address OFB in 3D [74]. The OFB is generated by laser-induced breakdown and thermocapillary flow is caused by heating the gas inside the bubble by nonlinear absorption.

Zheng et al. generated OFB in water on a SiO_2 substrate coated with a silver film. The OFB was kept static, and accumulated 1-µm polystyrene micro-particles [85] from surrounding area by using thermocapillary flow. These particles served as "ink" and were left behind when the OFB moved. Using this method, microparticles were patterned on the substrate.

Prior to this work, the OFB had not been thoroughly explored for the transportation of biological micro-objects.

1.3.4 OFB ON AN ABSORBING SUBSTRATE

In this dissertation, the hot spot that drives the motion of the OFB is created by the optical heating of an absorbing substrate. The top and side views of this system are illustrated in Fig. 1-1. The optically induced temperature gradient results a net movement of the gas bubble towards the warmest location, which corresponds to the position of the projected light beam (Fig. 1-1a). The OFB eventually centers above the light spot, where the fluid forces causing horizontal movement cancel out. To transport a micro-object, the thermocapillary flow brings the interface in physical contact with the object surface. The surface tension, which maintains the bubble surface shape, can push the objects to move.

The temperature difference between top and bottom of the bubble also causes a vertical component of thermocapillary flow (Fig. 1-1b). This vertical component counteracts the buoyance force, and pulls the bubble downwards. If the vertical component of the thermocapillary flow is not strong enough, the buoyance force may overcome it, and a cover is added to restrict the vertical movement of the OFB. If vertical component of thermocapillary flow is stronger than the buoyance force, the substrate prevents the bubble to center on the light spot in the vertical direction. Thus, this vertical component is present even when the bubble centers over the light spot.

The vertical component of thermocapillary flow also plays a role in micro-transportation. This convection also adds hydrodynamic force to the micro-objects within its range. The motion of these micro-objects depends on the hydrodynamic flow, as well as the geometry and density of the micro-objects. As described in the later section 3.5.4, careful modulation of the vertical component of thermocapillary flow provides an efficient way to non-contact transport single cells.

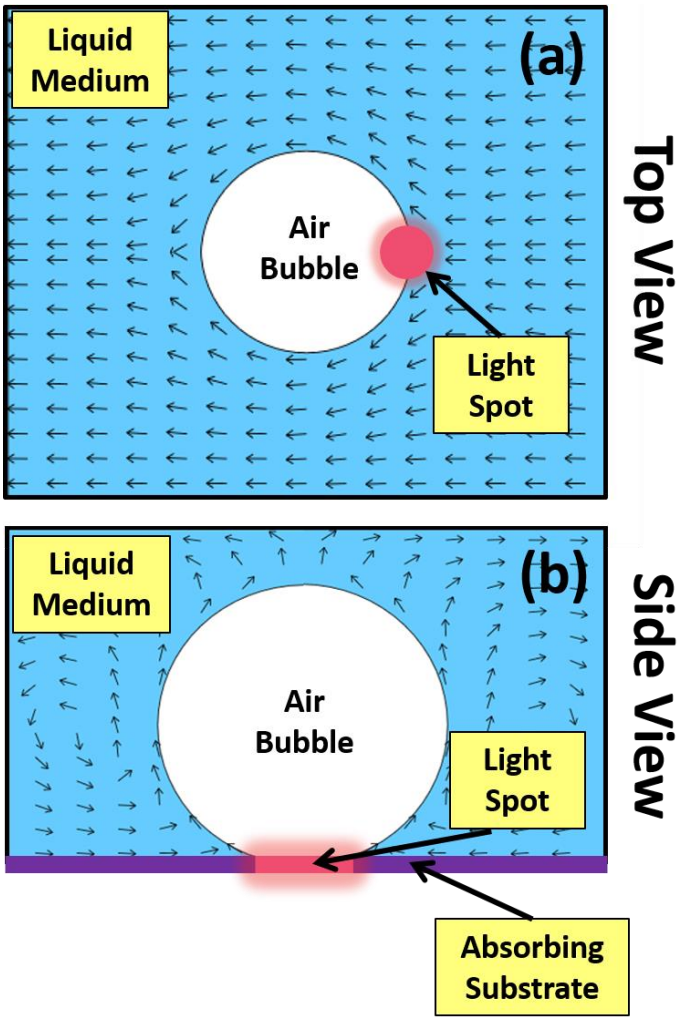

Fig. 1-1 Illustration of the thermocapillary flow around the OFB on the absorbing substrate. The reference frame is fixed on the bubble. The fluid mechanics inside the bubble are not shown. The spot heated by light beam is marked in red. (a) Top view. (b) Side view.

1.4 OUTLINE OF THE DISSERTATION

In this dissertation, OFBs with varying dimensions were used to transport biological micro-objects such as microbeads, single cells, and cell-laden microgels. The micro-objects were patterned into different geometries to show the potential applications for engineering artificial tissue. The results of each transportation was subjected to viability tests or subsequent cell culturing to check the effects on the biological micro-objects. High cell viability rates were observed, showing OFB is a dexterous and reliable

biological micro-transportation tool. The following chapters of this dissertation are organized as follows:

Chapter 2: OFB in Oil. In silicone oil, basic bubble actuation, contact/non-contact object transportation, and parallel operation were studied, serving as models for later research. The thermocapillary effect is very strong in silicone oil due to its low thermal conductivity and capacity. An off-the-shelf projector was customized to generate light pattern animation to address the bubble motion. Multiple light patterns were also used to independently control up to eight OFBs through an iPad touchscreen interface. Electrical engineering concepts related to the work in this chapter include the free-space optics utilized in the experimental setup, and the programming required to create a user interface for parallel micro-transporter actuation.

Chapter 3: OFB in Water. Various bio-micro-objects, from ~ 8 μm single cells to ~ 200 μm microgels, were transported in phosphate-buffered saline (PBS) or other physiological media, demonstrating the transportation capability of OFB. In order to create enough temperature gradient in water, 980 nm laser is used as the laser source. Glass beads were transported to characterize the OFB transportation capability, with a force larger than 1.8 nN demonstrated. Then, to demonstrate bio-micro-transportation, cell-laden microgels were patterned in PBS. Both yeast and NIH-3T3 fibroblast cells were seeded into microgel beads to mimic the building blocks of functional tissue. The patterning results were cultured and the cell viabilities were evaluated to prove the biocompatibility of OFB. At last, single cells were patterned by non-contact transportation, using thermocapillary flow. Using this technique, a single-cell array was patterned in ECM. High viability rates were observed. These features further prove the concept of applying OFB in cellular microbiology research. Electrical engineering concepts related in this chapter include the laser optics utilized in the experimental setup and the motion control system required to characterize the OFB mobility.

Chapter 4: Hydrogel Micro-transporter Driven by OFB (HMDO). OFB is preferred not to directly contact with cells, as the generated shear stress may harm the cell membrane. To realize the contact transport of bio-micro-objects, bio-compatible hydrogel micro-structures driven by OFB were developed. The hydrogel micro-structure were fabricated by a polymerization process with UV light provided by a customized projector. By using this hydrogel end-effector, cells and micro-beads can

be densely packed, increasing the OFB micro-transportation resolution. This transportation mechanism inherits the parallel transportation feature of optical transportation, and is independent of the electrical and optical properties of biological micro-objects. Yeast cells and cell-laden microgels were patterned and cultured, and the cells successfully multiplied.

As an effort to make the HMDO work with general substrates such as glass slides and plastic petri dishes, the hydrogel end-effector was rendered absorbing by doping with carbon black. After this modification, the OFB can drive the absorbing hydrogel micro-structure without the presence of an absorbing substrate. Preliminary results of cell and micro-object transportation are shown.

The additional electrical engineering concept here to Chapter 3 is the customized photo-polymerization system for fabricating the hydrogel micro-transporter.

Chapter 5: Conclusion and Future Work. The content of Chapter 2 to 4 is summarized, and ways to extend and improve OFB micro-transportation are discussed, along with the future applications of OFB.

CHAPTER. 2 OFB IN OIL

2.1 INTRODUCTION

Non-coherent light illumination from a computer projector is sufficient to actuate OFB motion in silicone oil with the help of an optically absorbent substrate. This OFB-in-oil system made it possible to characterize the bubble actuation, demonstrate contact and non-contact micro-transportation, and develop parallel OFB actuation.

2.2 EXPERIMENT SETUP

The thermal conductivity (λ) and specific heat capacity (Cp) is low for silicone oil (λ= 0.11 $W \cdot m^{-1} \cdot K^{-1}$, Cp= 1717 $J \cdot kg^{-1} \cdot K^{-1}$) [86] compared with water (λ= 0.607 $W \cdot m^{-1} \cdot K^{-1}$, Cp= 4181 $J \cdot kg^{-1} \cdot K^{-1}$) [79][87] . This means that it is easier to create a temperature gradient inside silicone oil, making the thermocapillary flow very strong. Fig. 2-1 shows a typical OFB system in silicone oil. The inset gives a side view of the fluidic chamber structure and the opto-thermal control mechanism. The light source is a computer projector (Dell 2400MP) with the projection optics removed. Arbitrary light patterns can be formed by the projector, although its optical power is relatively low, so the vertical component of thermocapillary (Fig. 1-1) is not strong enough to anchor the bubble on the substrate. Thus, a 1.1-mm-thick glass cover was added over the optically absorbent substrate to ensure the bubble remained in the oil. The top glass cover and the substrate were separated by 300-μm-thick spacers consisting of three layers of glass microscope coverslips, glued together using epoxy (Devcon, Illinois Tool Works Inc.). To enhance the heating by optical illumination, an optically absorbent substrate is used. It consists of a 1.1 mm-thick glass slide coated with a 200-nm-thick layer of indium tin oxide (ITO), topped by a 1-μm-thick layer of amorphous silicon (α-Si). The light from the projector is focused by a 5X objective lens onto the optically absorbent substrate.

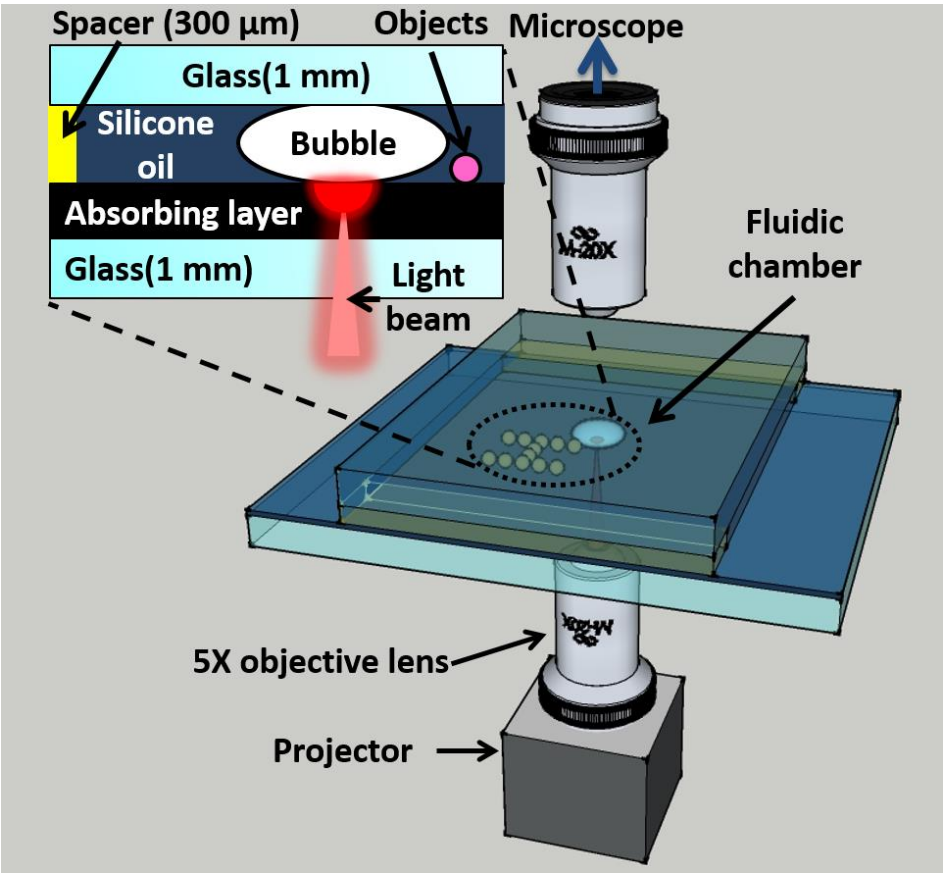

Fig. 2-1 Experimental setup of the OFB system in silicone oil. The inset gives a side view of the fluidic chamber structure and the control mechanism. The bubble is stably trapped by the light beam in the inset.

2.3 SIMULATION OF THE THERMOCAPILLARY FLOW AROUND OFB

This thermocapillary flow around OFB in the fluidic chamber filled with silicone oil was simulated using finite-element modeling software (COMSOL Multiphysics) in Fig. 2-2. In the simulation, the fluidic chamber has a height of 300 µm and the bubble radius is 125 µm. To model the heat source, a saturated Gaussian heat source distribution with a peak temperature of 300.8 K and a full-width at half-maximum of 424 µm is set at the front edge of the bubble surface (Fig. 2-2a). This peak temperature was determined empirically using a 50-µm-thick thermocouple (Omega Engineering) inserted into the fluidic chamber. The simulation shows the thermocapillary flow from both top and side views. The reference frame in this simulation is the bubble, which remains fixed in place.

When the maximum temperature of the heat source is located at x = 250 µm, the simulation shows that the temperature and surface tension gradients drive a horizontal fluid motion from the hot side of the bubble to the cold side (Fig. 2-2a). A vertical convection is present around the bubbles, as well (Fig. 2-2b). This flow component is due to temperature gradient between top and bottom of the fluidic chamber, as mentioned in Section 1.3.4.

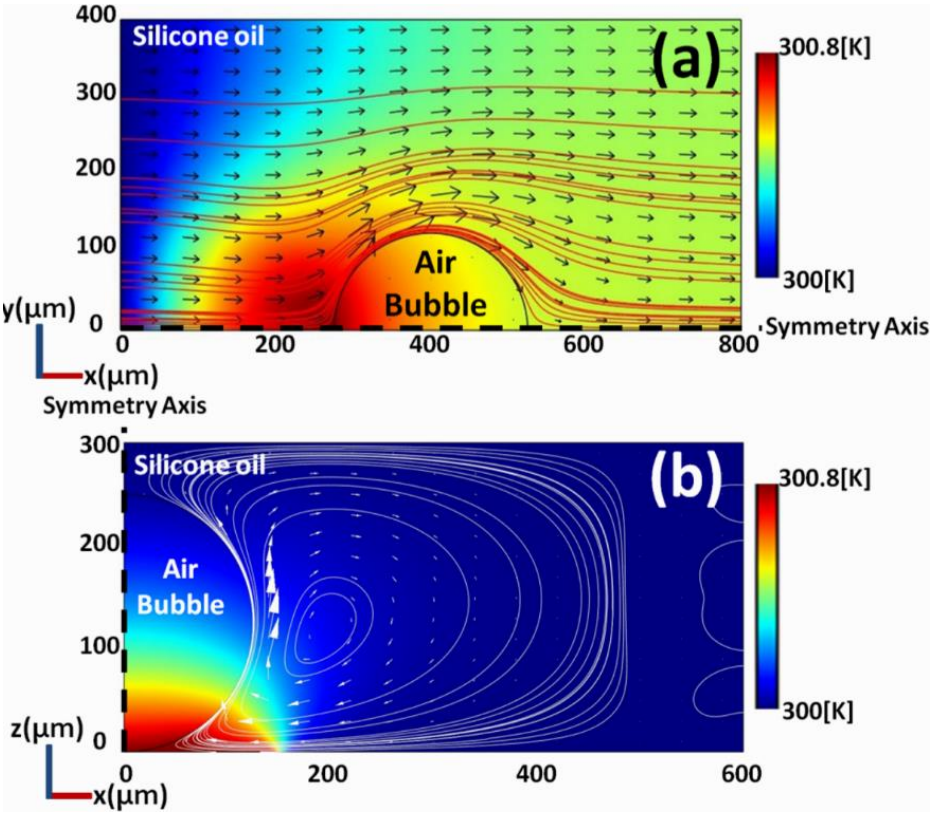

Fig. 2-2 Simulation of the thermocapillary flow around the OFB in silicone oil. The convective heat transfer inside the bubble and flow-induced deformation of the bubble are not considered in these simulations. (a)Top view of the system. (b) Side view of the system. Simulation of the vertical convective flow generated by the same heat source in (a). Based on empirical observations, the bubble is in contact with substrate, with a contact angle of 180◦.

2.4 PATTERNING OF GLASS BEADS

The micro-transportation capabilities of the OFB were demonstrated by pushing a 120-µm-diameter glass bead (Polysciences, Inc) around a feature on the surface of the substrate using a 488-µm-diameter air bubble (Fig. 2-3). The light spot used to control

the bubble was addressed by user input in a program written in the Processing development environment [88]. Running a program in the Processing development environment opens a window that displays the graphics specified within the code. Graphics defined within the Processing code can range from simple to complex; they can also be animated or be responsive to input from peripherals such as a mouse or keyboard. The graphics in the Processing display window is sent to the projector, converting the graphics into the optical patterns used to drive the OFB system. The control programs used in the experiments create white circles of various diameters against a black background, maximizing contrast. Projecting one or more spots onto the substrate generates radial temperature gradients at the locations where the light is absorbed. The programs contain both predefined animations of circles traversing the display window as well as circles that can be moved by user input. The current control system does not support feedback from the microscope, thus some manual control by the user is necessary. Currently, the control software relies on mouse and keyboard input to handle different events including spot generation, deletion, and movement.

The bead can be physically pushed by the bubble (Fig. 2-3a). In this case, the bead was always in contact with the bubble, and was pushed by the liquid/gas interface. This contrasts with bead being pulled by thermocapillary convection surrounding the bubble (Fig. 2-3b). The small spacing between the glass bead and the bubble meniscus verifies this, since the meniscus was not directly interacting with the bead. When the OFB stops moving, it was found that glass bead was stably trapped on the OFB surface and would not circulate with the convection, as shown in the frame at t = 0 s in Fig. 2-3b. This suggests the vertical component of thermocapillary flow is not fast enough to lift up the glass bead (density: 2.48 g/cm^3).

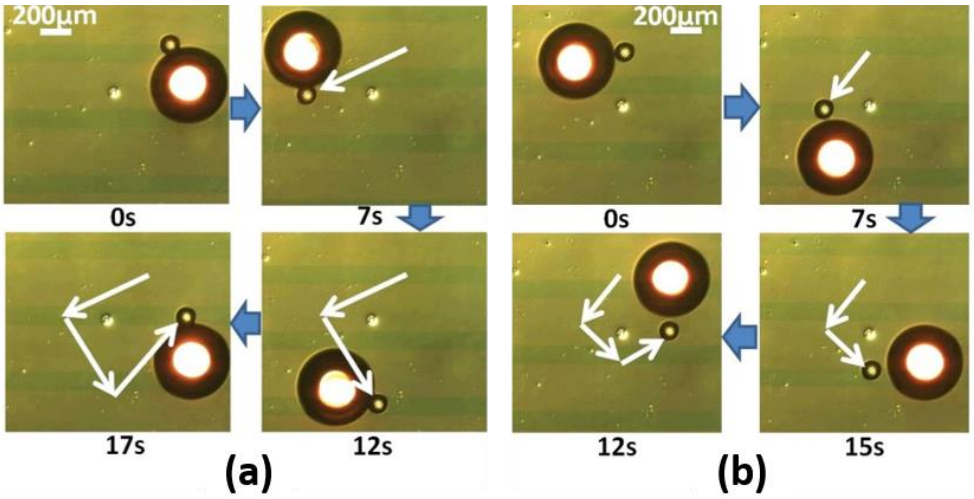

Fig. 2-3 An OFB (diameter = 488 μm) is used to move a glass bead (diameter = 120 μm) around a feature on the substrate surface. The feature is the dot in the center of the images. The light intensity is 5.3 W/cm^2. The light pattern diameter is 280 μm. (a) The OFB transports the bead by physical contact of the liquid/air interface. (b) The OFB transports the bead by the hydrodynamic force of the convection surrounding the bubble.

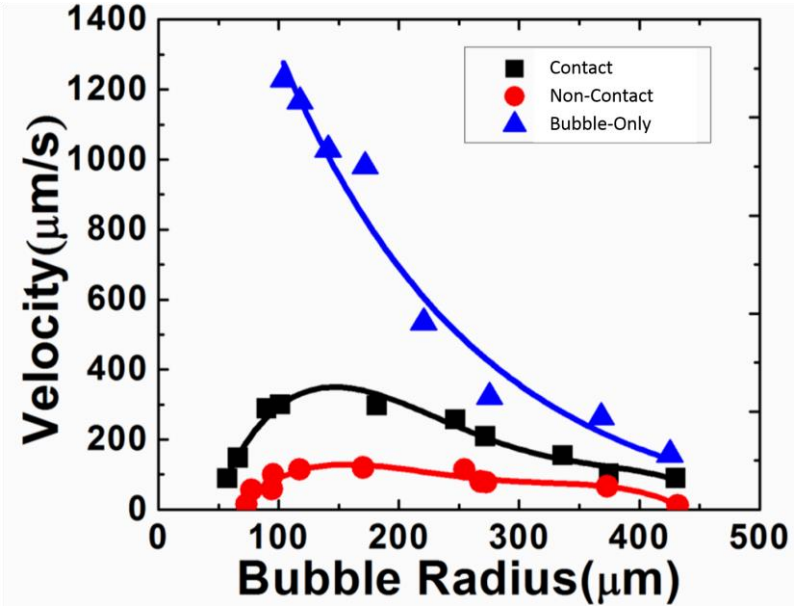

Fig. 2-4 Transportation velocity of a glass bead (diameter = 120 μm) in term of the OFB size. The light intensity is 5.3 W/cm^2, and the light pattern radius is 280 μm. For bubble only case (triangles), the velocity of the OFB itself is recorded. The other data correspond to the transportation of the glass bead using contact transportation (squares) and non-contact transportation (circles).

The OFB actuation velocity and bead transportation velocity were characterized for increasing bubble radii (Fig. 2-4). The contact transportation velocities continue increasing with increasing bubble size until the bubble radius becomes larger than approximately 150 µm. When pushing an object, a larger bubble has smaller curvature than small one, leading to larger contact area with the glass bead, and more force. The saturation in contact transportation velocity as the bubble radius increases beyond 100 µm is partially caused by the monotonic decrease in OFB actuation velocity.

The non-contact bead transportation velocity increases with increasing bubble radius due to an increase of the peak flow velocity of the vertical convection, up to a bubble radius of 150 µm. This is also supported by preliminary simulations based on the empirical conditions. For bubble radii larger than 150 µm, the decrease in OFB actuation velocity affects the non-contact transportation velocity. In addition, the peak flow velocity of the vertical convection saturates for these larger bubbles, contributing to the drop of the bead transportation velocity.

Randomly distributed glass beads with radii varying from 49 to 74 µm were patterned by an OFB, to form the initials "UH," for "University of Hawaii" (Fig. 2-5). The OFB utilized both contact and non-contact transportation to position the glass beads, with an average transportation velocity of approximately 200 µm/s.

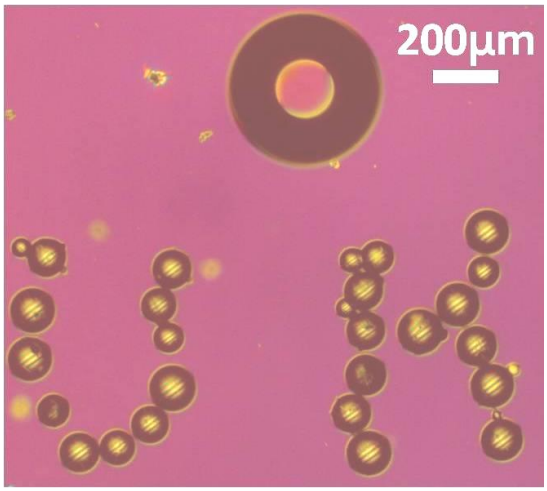

Fig. 2-5 Patterning of glass beads by an OFB (diameter= 572 µm). The OFB in the top center of the photo was used to position glass microbeads (diameter = 98 to 148 µm) into the initials "UH."

2.5 PATTERNING OF SU-8 MICROSTRUCTURES

The OFB is capable of the assembly of micro-objects, as demonstrated by the tight packing of three micro-triangles (Fig. 2-6). These right triangles are made of SU-8 (MicroChem Corp.), a polymeric photoresist. The triangles have an average thickness of 100 μm, and dimensions of 360 μm and 185 μm for the two legs. The micro-transporter utilized both contact and non-contract transportation to position the triangles at an average transportation velocity of approximately 50 μm/s. The transportation velocity of the triangles is less than that of the glass beads due to increased friction between the triangles and the substrate. The convection around the OFB did not show causing any motion on the triangles. This might be due to the large surface force since the contact area between the substrate and the triangle is substantially larger than that for glass bead.

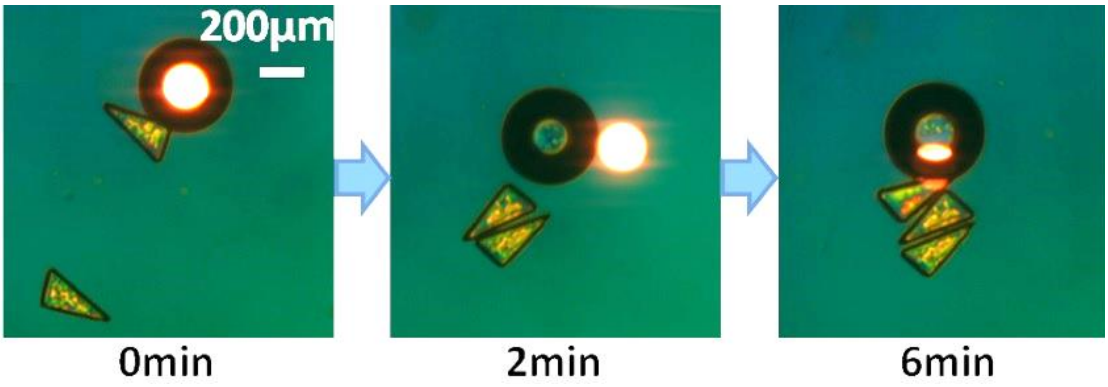

Fig. 2-6 Patterning of triangular SU-8 pieces by an OFB (diameter = 500 μm) into a tightly packed structure.

2.6 PATTERNING OF MICROGELS

The ability to assemble micro-objects into desired patterns is useful for creating artificial *in vitro* tissue [89]. A useful micro-object for this application is cell-laden microgels, which can be used to seed the formation of the tissue [90]. Micro-transportation of cell-laden microgels using OFB was demonstrated by arranging hydrogel beads containing yeasts into a line (Fig. 2-7). The yeast-laden hydrogel beads were created through an emulsion process [91]. The yeast (bakers' yeast) was rehydrated in YPD and allowed to sediment. A 10-μL aliquot of the yeast sediment was added to 1 mL of 1.5% (w/w) agarose solution (low-melting-point analytical grade

agarose; Promega) at 37 °C. The final cell concentration is about 5×10^6 cells/ml. This cell/agarose solution (0.5 ml) was then mixed with 4 mL of fluorinated oil (FC-40, 3M Corp.) with 1% EA surfactant (RainDance Technologies; Lexington, MA). The solution was put into a 15-mL centrifuge tube and mixed on the vortex mixer for 30 seconds. After this step, agarose droplets laden with cells were generated within the oil. This emulsion was then cooled in the refrigerator at 0 °C for five minutes, which gelled the agarose droplets, forming beads. Phosphate-buffered saline (PBS) was then added until the emulsion volume was 7 mL, and the emulsion was centrifuged at 4000 rpm/s for 30 seconds. Since the density of the FC-40 (1.855 g/cm^3) is higher than that of the agarose hydrogel beads, most hydrogel beads entered the PBS solution. This PBS solution with hydrogel beads was used for the experiment. The yeasts encapsulated in the beads can be seen in the inset of Fig. 2-7, and are circled for clarity.

The transportation of the hydrogel beads was done in FC-40 fluorinated oil, chosen for its permeability to gases, allowing cells to aspirate inside the microgels. FC-40 also has even lower thermal conductivity (λ = 0.0065 W•m^{-1}•K^{-1}) and heat capacity (Cp =1100 J•kg^{-1}•K^{-1} [92] than silicone oil. Since its density is larger than water, the microgels beads floated in the oil, reducing friction with the chamber surfaces, and resulting in an average transportation velocity of 200 µm/s. Contact micro-transportation was utilized to position a random distribution of the beads into a vertical arrangement, then a horizontal arrangement (Fig. 2-7).

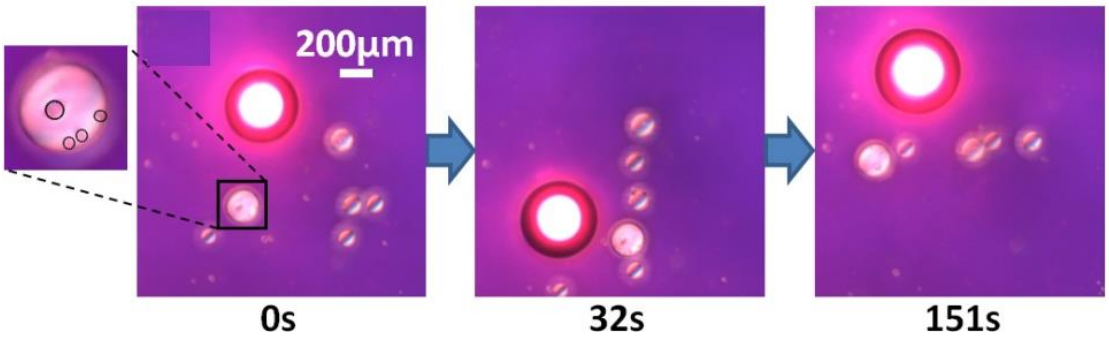

Fig. 2-7 Patterning of yeast laden microgels by an OFB (diameter = 450 µm). Microgels were first arranged into a vertical line, followed by rearrangement into a horizontal line.

2.7 PARALLEL AND COOPERATIVE MICRO-TRANSPORTATION

2.7.1 INTRODUCTION

End-effectors actuated both independently and in parallel are critical for parallel and cooperative micro-transportation, as this can potentially increase the system transportation throughput. This has been achieved in systems actuated by magnetic fields [57] [52] and optical radiation pressure [33][93]. Parallel and independent addressing of multiple end-effectors by magnetic fields usually requires distinct features on each end-effector, enabling unique responses to complex control signals. To date, no more than five magnetic microrobots have been independently controlled at the same time [57][52]. In contrast, optically addressed end-effectors can take the advantage of commercial light-beam-shaping devices to make the control of individual end-effectors intrinsically independent from each other [33][93]. The control of OFB also inherits this capability for independent control, making it possible to implement parallel and independent actuation.

2.7.2 PARALLEL OFB

In the bubble transportation system with a computer projector light source, parallel OFB actuation was realized by projecting multiple light patterns onto the substrate. This was demonstrated by actuating three OFBs at once with light patterns moving from the bottom to the top of the field of view (Fig. 2-8). In this case, the light patterns were created in Microsoft PowerPoint™ and played as an animation by the projector.

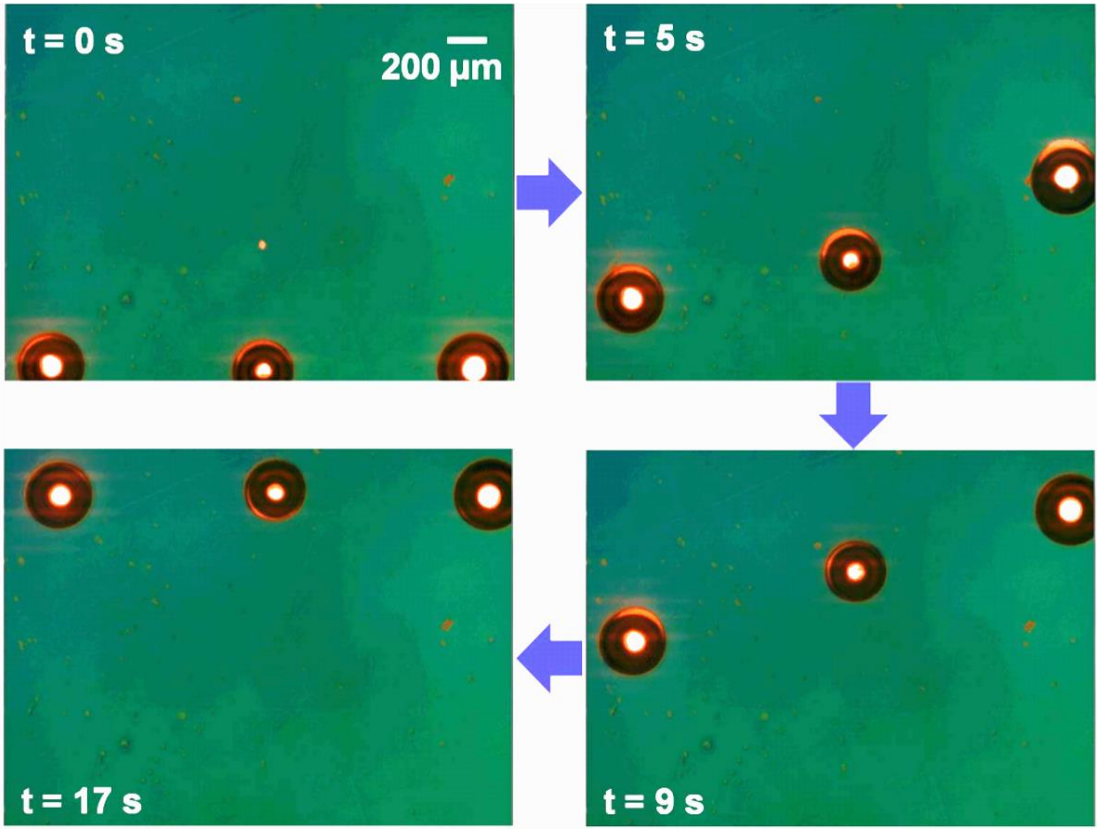

Fig. 2-8 Parallel and independent actuation of three OFBs in silicone oil. The OFB (average diameter: 342 µm) were moved independently at different velocities from the bottom to the top of the field of view.

2.7.3 COOPERATIVE TRANSPORTATION THROUGH MULTI-TOUCH SCREEN

In order to independently address larger numbers of OFBs, an application was created that utilizes the capacitive multi-touch technology of the Apple iPad, like similar controllers for optical tweezers systems [93]. A custom application was created for the iPad that combines the ability to create, reposition, re-size, and remove light patterns within a set workspace. These light patterns control the movement of the OFB, and appear on the iPad screen as white circles, hereafter called micro-transporter controllers (MC). The iPad was connected to a computer projector, which projects the light patterns onto the substrate of the OFB system. The iPad display was aligned with a live-view camera allowing for simultaneous control of the light sources and instant visual feedback (Fig. 2-9).

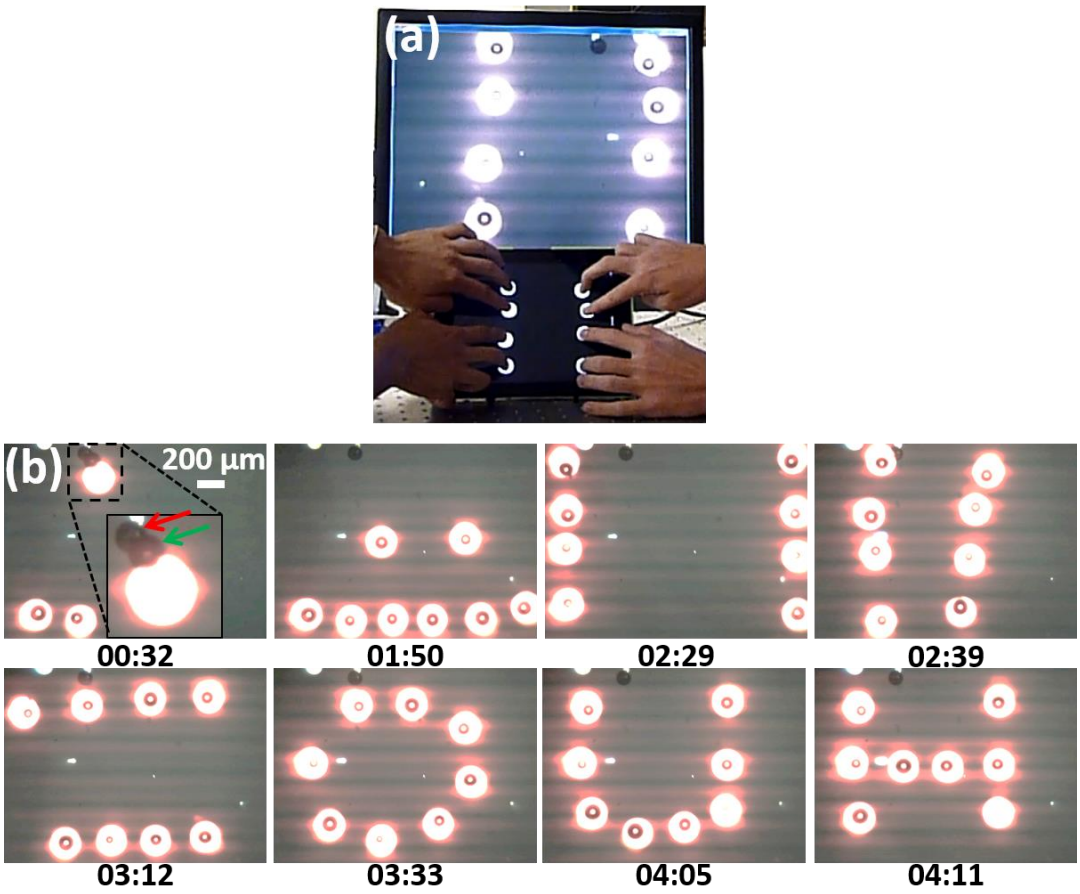

Fig. 2-9 Parallel and independent actuation of eight OFBs by the light beams from the projector controlled by a custom iPad application. The time stamp format is m:s. (a) The iPad display was aligned with the live-view of the microscope camera. The iPad is visible in the lower part of the photo, and the computer monitor with the live feedback from the microscope is in the upper part of the photo. The white circles on the iPad display correspond to the light patterns controlling the OFB. (b) Sequential frames from actuation. The inset in the first frame shows the generation of the bubble at one defect on the substrate. The red arrow marks the defect and the green arrow marks the bubble being generated. A light pattern was positioned nearby to capture the bubble after the generation process was completed.

The iPad app functions through a single visual interface. Using the default touch libraries of the Apple iPad operating system, various gestures were assigned to specific tasks. This includes a double-tap to create an MC, multi-touch support for the simultaneous movement of MCs, and a triple tap to delete an MC. The size of the MCs can also be controlled by pinch gestures.

In order to prevent the merging of the OFB, the application constantly checks for potential collisions between MCs. When an MC is changed in size or moved, its location is compared to the other MCs to ensure an appropriate boundary is maintained around each bubble. The minimum distance allowed between adjacent MCs is derived algorithmically using the respective sizes of the selected MC and the MC with which it is being compared. Similarly, any time a new gesture is recognized, the location of the selected MC is compared to the stored locations within a data array to identify the selected MC.

Parallel transportation of multiple OFB was demonstrated using this iPad app. In this experiment, the spacer was made of three layers of double-sided polyimide tape that totaled 300 μm in height. The OFB were generated by illuminating a defect on the substrate with a laser 800-mW, 980-nm, continuous-wave laser for approximately two seconds (Fig. 2-9b, shown in inset of the first frame). The defect was originally created by continuous illumination from the laser, focused by a long working distance 0.28-N.A.10X objective lens (Mitutoyo, Japan) on a single point. Under illumination by this laser, a piece of α-Si peeled off after approximately five seconds, exposing the ITO layer below, and creating the defect. Preliminary experiments showed that bubbles could be easily generated on these defects. It is suspected that these defects serve as nucleation sites that facilitate bubble formation. However, further research into this hypothesis is still needed.

Bubble generation at the defect site was repeated, serially creating eight OFBs. At the same time, eight MCs were created sequentially to capture the newly generated OFB. The light intensity of each MC is 5.2 W/cm^2. The average radius of the OFB was 50 μm. The bubbles were then sequentially re-arranged into different patterns, including two vertical lines, two horizontal lines, a circle, the letter U and the letter H (Fig. 2-9b). The average velocity for each bubble micro-transporter was about 200 μm/s.

Cooperative micro-transportation was also performed using the iPad app (Fig. 2-10). Four OFBs were used to perform a cooperative bead "handoff" routine, where glass beads were passed among the OFBs. The glass beads were transported using a combination of the contact and non-contact transporters. Two glass beads were exchanged between the OFB A and C and B and D (Fig. 2-10a-c). The two beads were then brought to the center of the screen (Fig. 2-10d) and exchanged between bubble

OFB A and D (Fig. 2-10e). At last, in Fig. 8f, the glass beads were brought by the bubble OFB to the position diagonally opposite to their location from Fig. 2-10c.

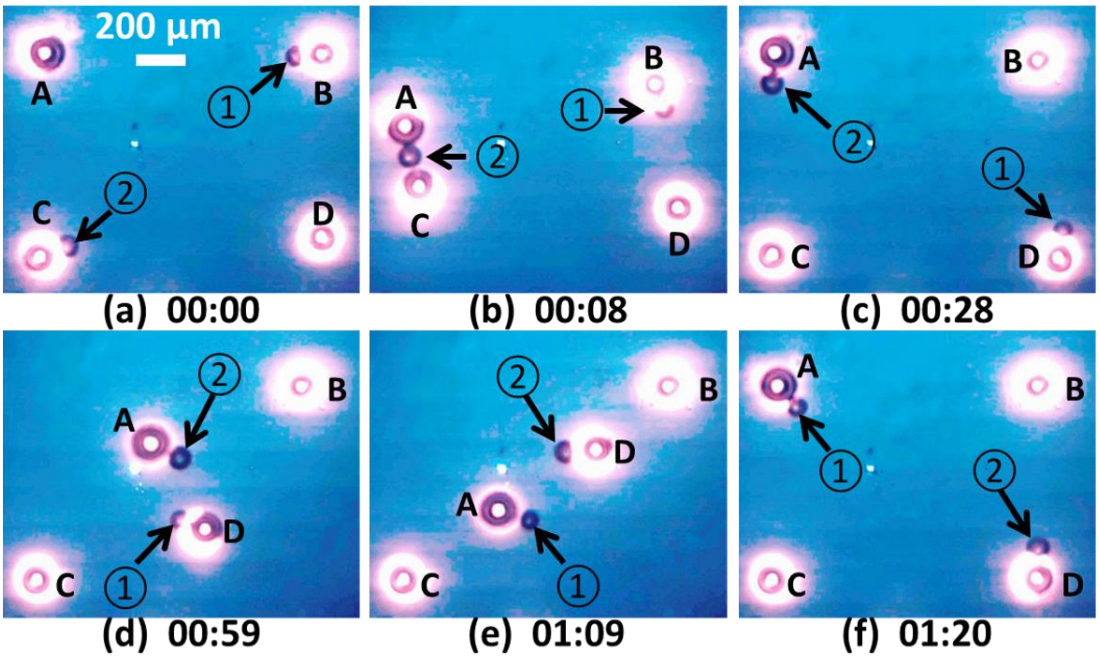

Fig. 2-10 Cooperative transportation of two glass beads between OFB controlled by iPad. Four OFBs are marked by A, B, C, D. Two glass beads are marked by 1 2. The time stamp format is minutes: seconds. (a-c), B handed No. 1 bead to D when C handed the No. 2 bead to A. (d-f) Two glass beads were exchanged by two OFBs in the center and brought to the opposite side by another OFB.

CHAPTER. 3 OFB IN WATER

3.1 INTRODUCTION

If the OFB are to be used for the transportation of bio-micro-objects, such as cells or cell-laden hydrogels, it can be advantageous to work in aqueous solutions, for example, in phosphate-buffered saline (PBS) solution. Compared to actuation of the bubble in silicone oil, a stronger light source is required when aqueous solution is used. This is due to the higher thermal conductivity of water compared to the oils used in the previous results, making it more challenging to create large temperature gradients. Thus, instead of a computer projector, a laser is used as the light source. The higher intensity of the laser enables the creation of higher temperatures at the optically absorbing substrate, resulting in a thermal gradient that is sufficient to move the OFB in aqueous solutions.

The 1064-nm laser is approved by FDA for many biomedical applications [94][95]. To approach this wavelength, a laser wavelength of 980-nm is used for the experiments described here. Compared to shorter wavelengths, this wavelength causes less DNA damage when the laser directly illuminates the cells [27].

3.2 EXPERIMENT SETUP

The main change to the experimental setup of the system discussed in Chapter 2 is the light source, which is now a 980-nm diode laser (Laserlands, 980MD) (Fig. 3-1). The laser has a peak power of 800 mW, and it can operate at lower powers as well. The fluidic chamber was put on the specimen stage under an Olympus BXFM upright microscope. The laser was mounted on a XYZ stage below the microscope stage (Fig. 3-1), and focused onto the absorbing substrate to a spot with a diameter of 4.4 μm by a 20X, 0.4-N.A objective lens (Meiji, Japan 13560). An ITO-coated slide (sheet resistance of 4 to 10 ohms, Delta Technologies), consisting of 1-mm-thick glass topped by a 200-nm-thick ITO layer was chosen as the absorbing substrate since it has verified biocompatibility with cells [96]. Empirical measurements by an optical power meter (Newport 1830-C, Detector: 818-SL) showed that 70% light was absorbed by the substrate, without accounting for reflections at each interface.

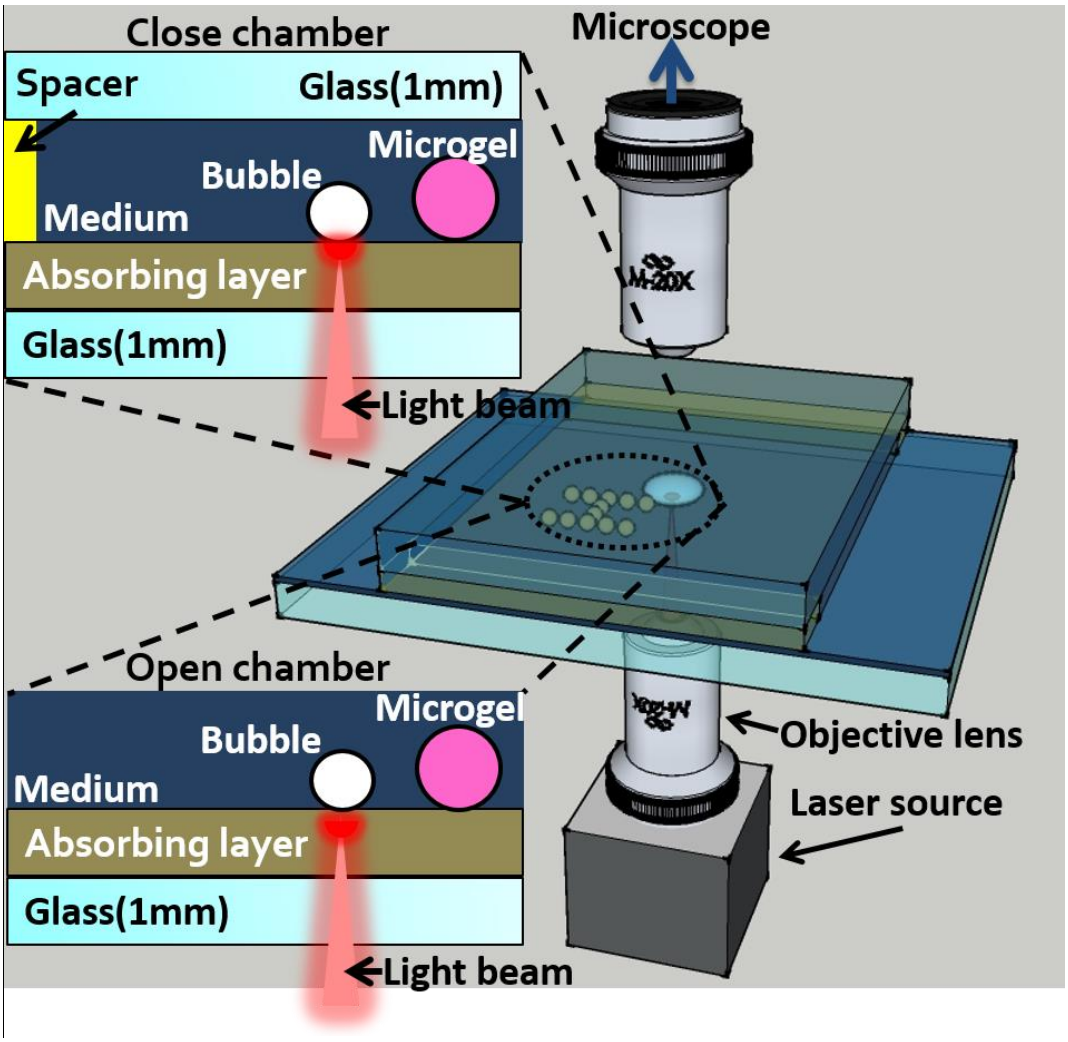

Fig. 3-1 Experimental setup of the OFB in water system. A 980-nm diode laser is focused onto the absorbing substrate. The OFB can function in either enclosed fluidic chamber or open substrate, depending on the task.

Unlike OFB addressed by the computer projector, in this laser-based system, the vertical component of thermocapillary flow can be strong enough to pull the bubble to the substrate during actuation. Thus the actuation can take in place either inside a fluidic chamber or in an uncovered reservoir, depending on the balance between the vertical component of the thermocapillary flow and buoyance force on the OFB, as discussed in Section 1.3.4. The performance of OFB in an enclosed fluidic chamber shows that the OFB can be integrated with other microfluidic devices, like magnetic-field-driven microrobots [97]. This topic is discussed further in Section 3.3.

Transportation by OFB in an uncovered reservoir simplifies the culturing and harvesting of bio-micro-objects, as there is no cover to restrict the nutrient and gas

exchange between the environment and the bio-micro-objects. This is of importance to *in vitro* tissue engineering, since the assembled result can be immediately transferred onto tissue-culture plates for subsequent procedures, without changing the current established biological protocols. This topic is discussed further in Section 3.4.

3.3 MICRO-TRANSPORTATION IN AN ENCLOSED FLUIDIC CHAMBER

3.3.1 TRANSPORTATION PERFORMANCE

If the transportation is in fluidic chamber, the buoyancy force of the OFB is not a problem since the fluidic chamber cover can confine the bubble to the substrate. A fluidic chamber was formed by bonding a 1.1-mm-thick glass slide over the optically absorbent substrate using three layers of double-sided polyimide tape (Kapton tape, DuPont) as spacers (300 µm inthickness). To help the larger OFB (diameter > 100 µm) move freely in the fluidic chamber, the glass that forms the top of the chamber and the substrate on the bottom of the chamber were coated with polyethylene glycol (PEG) to increase their wettability. The method used to coat PEG is described elsewhere [98]. Briefly, a layer of native oxide was created on the fluidic chamber surfaces by Piranha treatment (H_2O_2:H_2SO_4 in a 2:5 volume ratio) at 55 ºC for 10 to 20 minutes. After rinsing the chamber pieces with deionized water and blow-drying with air, the pieces were soaked in a PEG-silane solution (2-[methoxy (polyethyleneoxy) propyl]-trimethoxysilane, Gelest) for two hours. The coated pieces were rinsed with ethanol before use. The actuation of smaller OFB (diameter < 100 µm) does not need the PEG coating. This might be due to the smaller contact area and less surface force with the substrate for smaller OFB.

The basic actuation of the OFB was demonstrated by moving around a feature on the surface (Fig. 3-2a). The bubble was introduced into the chamber by micropipette or by optically heating a defect on the substrate, as described in Section 2.7.3. Larger bubbles can be realized by fusing smaller bubbles. To measure the velocity, a linear actuator (850F-HS, Newport) was attached to the XYZ stage on which the laser was mounted, and was used to move the laser at a constant velocity. The velocity of a 510-µm-diameter bubble was characterized (Fig. 3-2b) At each laser intensity, the linear actuator velocity was adjusted until the bubble could no longer follow the laser. At an average intensity of 387 kW/cm^2, the OFB can move the 510-µm-diameter bubble at a

velocity of up to 4 mm/s. Smaller bubbles can move even faster. For example, a bubble with diameter smaller than 100 µm can easily move at over 10 mm/s. This is comparable to the 12.5 mm/s velocity achieved by the resonant magnetic actuator microrobots [99][52].

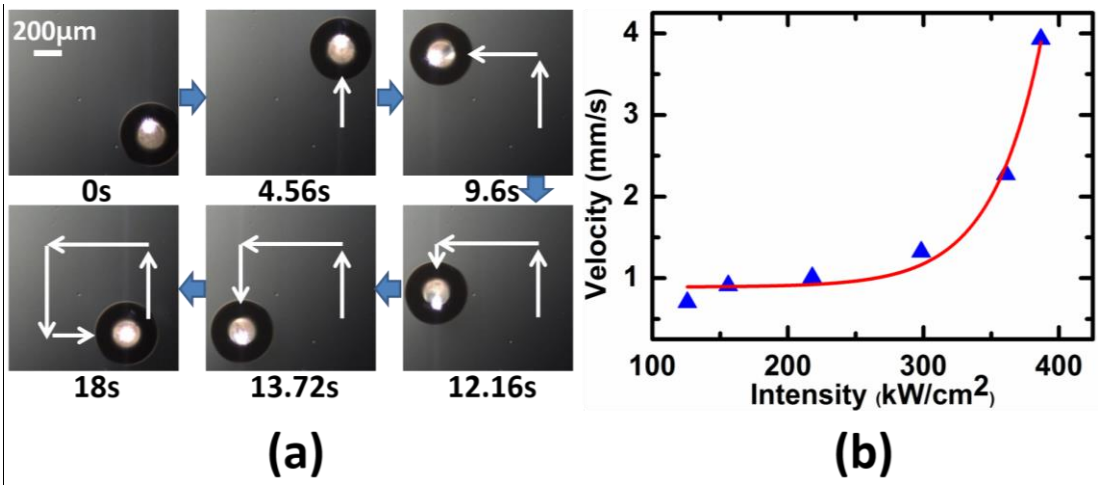

Fig. 3-2 OFB actuation in PBS. (a) Actuation of an OFB (diameter = 446 µm). The light intensity is 361 kW/cm^2. (b) The velocity of an OFB (diameter = 510 µm) as a function of laser intensity. A trend line is added to the graph.

Although the transportation velocity of micro-objects was not characterized, it can be inferred from the observation of a 338-µm-diameter OFB with eight glass beads attached to its meniscus. The OFB demonstrated a mobility up to 2.1 mm/s when the light intensity is 361 kW/cm^2. This stiction of the glass beads to the OFB is possibly due to the hydrophobicity of the bead surface [75]. As an estimation for the OFB actuation force, the total drag force for moving one glass beads at a constant velocity in water is calculated using Stokes' Law:

$$F_d = 6\pi\mu R v \qquad \text{Equation 3-1}$$

Equation 3-1 describes the drag force on a solid spherical particle with smooth surface moving at constant velocity in laminar flow. In this equation, μ is the dynamic viscosity (N▪s/m^2), R (m) is the radius of the spherical object, and v (m/s) is the particle's velocity. By taking the viscosity value in Table 2 and assuming the R = 50 µm, the calculated transportation force is about 1.8 nN. Thus, the force actuation force of eight glass beads

by the OFB is estimated to be larger than this value. More direct force measurement is currently under research.

The same focused laser spot used for OFB, at the maximum intensity 387 kW/cm^2 used in the results shown in Fig. 3-2b, was tested on a 100-µm-diameter glass bead to see if optical radiation pressure trapping could be observed. The fluidic chamber is similar, except the optically absorbing substrate was replaced by a glass slide. In this setup, no optical trapping was observed.

3.3.2 TEMPERATURE DISTRIBUTION AROUND OFB

For bio-micro-transportation, the maximum temperature during operation is a concern. The temperature at the bubble surface was measured using the configuration shown in the inset of Fig. 3-3. A 440-µm-diameter bubble was positioned in contact with the tip of 50-µm-thick thermocouple (Omega Engineering, Type T; resolution = 0.1 °C) while the laser (position marked by a white arrow) was focused on the contact line between the bubble and the substrate. The measured data when the light intensity is 361 kW/cm^2 and 387 kW/cm^2 is shown in Fig. 3-3. The distance between the contact line and the tip of the thermocouple is about 60 µm. The highest temperature measured at an intensity of 387 kW/cm^2 is 28 °C. This is well below the physiological temperature (normal human body temperature) of 37 °C.

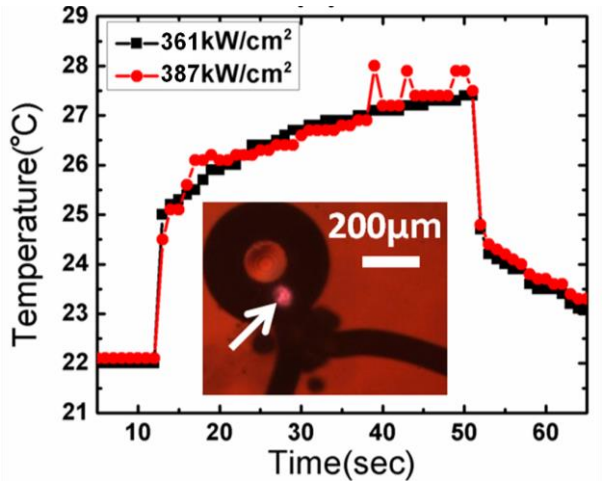

Fig. 3-3 Temperature measurement on the OFB (diameter = 440 µm) surface during laser illumination. The inset shows the measurement setup. The structure in the lower portion of the inset is the thermocouple. The laser spot is indicated by the white arrow.

3.3.3 PATTERNING OF CELL-LADEN MICROGELS

To verify the capability of patterning cell-laden microgels to form *in vitro* tissue, the OFB was used to pack four triangular agarose microgels laden with yeast cells into a holding structure in an enclosed fluidic chamber with a height of 60 µm (Fig. 3-4). The holding structure for the assembled micro-gels was fabricated using a process described by Chung et al. [100]. To fabricate the holding structure, trimethylolpropane triacrylate (TMPTA, Sigma Aldrich) with 1% Irgacure 819 (Ciba Specialty Chemicals Inc.) was flushed into a fluidic chamber formed by two glass microscope slides separated by a layer of polyimide tape (60 µm thick). The top glass slide was spin-coated with 50-µm-thick PDMS layer to render it non-adhesive to cured TMPTA. The pre-polymer was then selectively cured using a UV light pattern from a modified computer projector (Dell 2400MP). The UV filter of the projector was removed to provide an increased output of the light wavelengths absorbed by the photoinitiator. The desired holding structure shape was drawn in Microsoft PowerPoint software and displayed on the projector, creating the TMPTA structure. After the polymerization, the top glass slide was then removed, and uncured pre-polymer was rinsed using isopropyl alcohol. The cured holding structure was manually transferred onto the absorbing substrate using a 30-gauge syringe needle. The working fluidic chamber for the hydrogel assembly was then formed by placing a 1-mm-thick glass microscope slide over the absorbing substrate, using 60-µm-thick polyimide tape as spacers.

The microgels have the same dimension as the SU-8 microstructure discussed in Section 2.5. The height of the micro-gel was 50 µm. They were made using a PDMS molding process [101]. A mold was created to form the agarose micro-gels by spin-coating polydimethysiloxane (PDMS) onto a silicon wafer with 50-µm-high triangular SU-8 features. The PDMS was cured on a hotplate at 120°C for half an hour, then separated from the wafer, transferred onto a clean glass microscope slide, and exposed to a corona discharge for two minutes to render the surface hydrophilic [102], creating a thin-film mold. A drop of PBS was added onto the surface of the PDMS mold to cover it, and the mold was degassed under vacuum for 5 minutes. This step is to ensure all the triangular holes on the PDMS mold were wetted and accessible to molten agarose. After this step, molten agarose was dissolved in phosphate buffered saline (PBS) in a 3% weight-to-volume ratio.

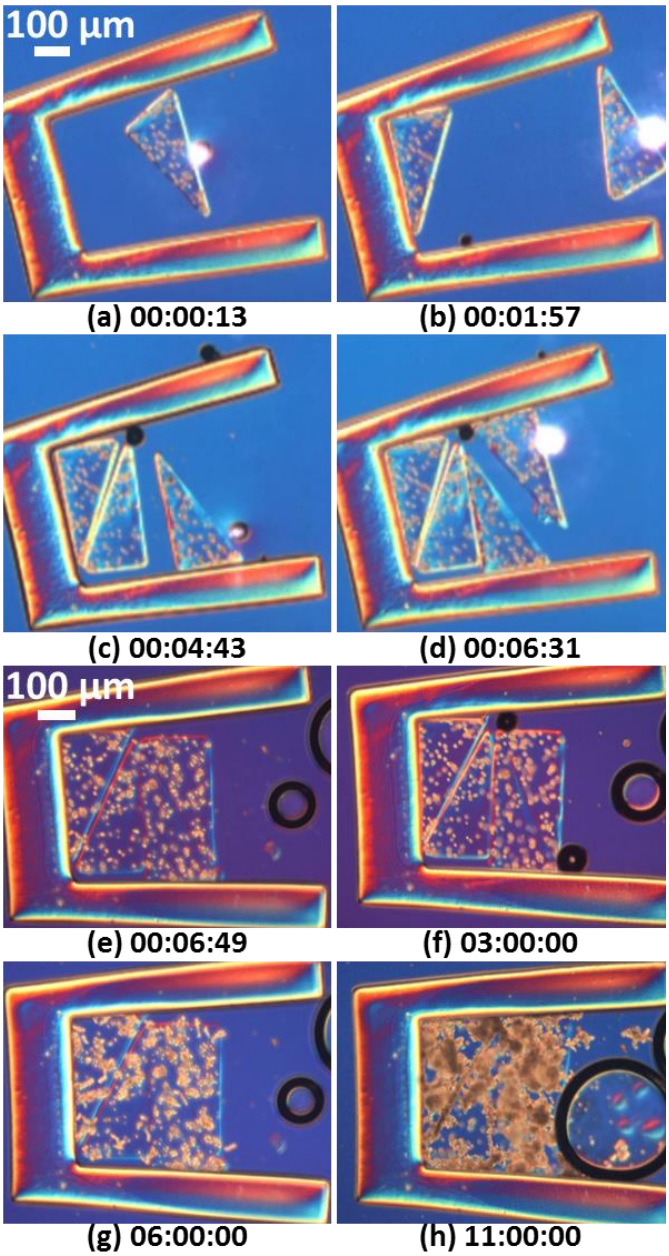

Fig. 3-4 Patterning and culturing of yeast-laden agarose microgels by OFB. The time stamp format is h: m: s. (a-d) Transportation of the microgels using the OFB. The laser sometimes obscures the bubble, but the bubble is clearly visible in (c) as it pushes the hypotenuse of the rightmost triangular microgel. (e-h) Yeast culturing. (e) The fluidic chamber was filled with YPD media. (f) Yeasts began to multiply after 3 hours. (g, h) The cells after undergoing multiple divisions.

Baker's yeast in PBS were mixed with 3% w/v agarose (Sigma-Aldrich, Type IX-A, gelling temperature: less than 20 °C) in PBS with 1:1 volume ratio to achieve a final concentration of 8.9×10^7 cells/ml. A PDMS mold was placed on the glass slide and

plasma-treated to render it hydrophilic. The molten yeast-laden agarose was poured onto the PDMS mold, and excess solution was removed by scraping over the top of the mold using a microscope glass coverslip. The mold was cooled to 4 ºC for 10 minutes to gel the agarose. The gel blocks were released by gently tapping the mold to one opening of the fluidic chamber, which was filled with PBS. A piece of filter paper was positioned at another of the fluidic chamber, wicking the fluid, and sucking the microgels into the fluidic chamber. The agarose concentrations used here were the lowest that yielded gel blocks with acceptable structural integrity.

In the experiment, micro-transportation outside the microscope field of view, defined here as moving an object more than 2 mm, was achieved by moving the microscope stage to change the relative position of the laser spot in the fluidic chamber. Short-distance precision transportation was performed by adjusting the laser position with the XYZ stage while the fluidic chamber remains fixed in place. The average distance that the microgels were transported by the bubble was 2 mm. To retrieve microgels outside the field of view of the microscope, the microscope stage was moved while keeping the laser position fixed.

Non-contact transportation was not used in this experiment due to the requirement of densely packing microgels. However, the flow that enables non-contact transportation does affect the contact transportation. Since the density of microgels is close to that of water [38], the vertical component of the thermocapillary flow around the OFB tends to lift the microgels off the substrate, away from the OFB. This can suspend the contact transportation. Thus, vertical motion of the microgels (height = 50 μm) was restricted by the low fluidic chamber height (height = 60 μm) in the experiment.

An OFB with diameter larger than 10 μm is able to transport the microgels by physical contact. By manually controlling the position of the laser with the XYZ stage, four microgels were densely packed into a holding structure in about six minutes. Ignoring the time spent on orienting the microgels, the average transport velocity was 100 μm/s. In some images, the camera was saturated by the laser (Fig. 3-4b, d) and the bubble was not visible. However, the bubble can be seen in Fig. 3-4a, c.

After the patterning, the chamber was flushed with yeast peptone dextrose (YPD, Gifco), and the yeast were cultured in an incubator (37 ºC, CO_2 concentration of 5%).

Photos of the culture were captured every few hours (Fig. 3-4e-h). The yeast multiplied several times after eleven hours of culturing (Fig. 3-4h). During the YPD flushing procedure, two bubbles were introduced near the opening of the holding structure (Fig. 3-4e). Two additional bubbles were seen in Fig. 3-4f; these additional bubbles are due to the outgassing from the metabolizing yeast. Eventually, these two bubbles merged with the original two bubbles. This process repeated with further outgassing, resulting in bubbles that grew continuously throughout the experiment (Fig. 3-4h).

3.3.4 COOPERATIVELY PATTERNING OF CELL-LADEN MICROGELS

To address multiple OFB, the laser beam has to be split, involving integration of scanning mirror or SLM into the optical path. As a simple proof-of-concept, an additional laser was added to the setup in Fig. 3-1 to demonstrate cooperative transportation of two OFBs in parallel (Fig. 3-5). Two lasers were projected obliquely onto the substrate, enabling parallel control of two OFBs without the use of a scanning mirror or SLM. Each laser was controlled by a separate operator, and the corresponding OFBs were moved independently and in parallel. In 78 seconds, two triangular agarose microgels were assembled into a densely-packed rectangular structure. A setup utilizing a scanning mirror or SLM that can address more OFBs in parallel is currently under development.

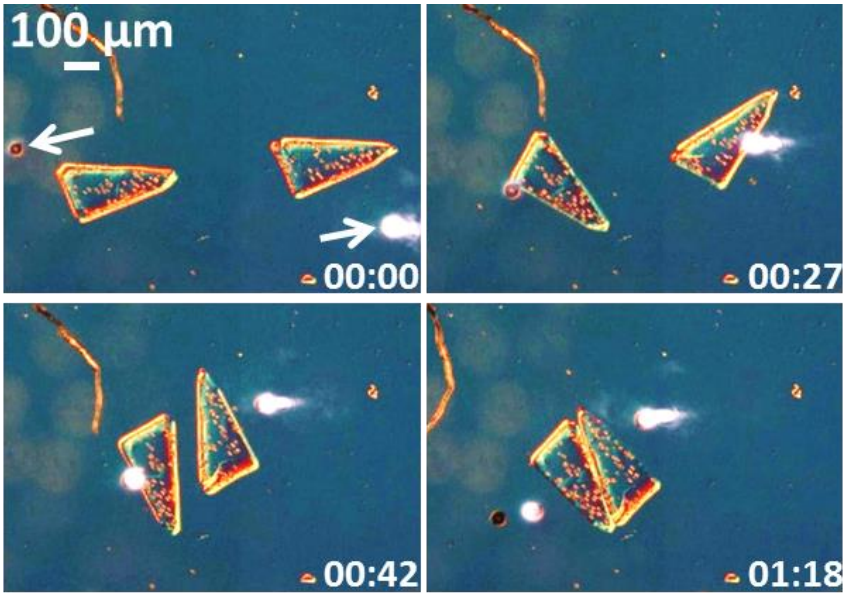

Fig. 3-5 Cooperative patterning of yeast-laden agarose microgels by two OFBs. Two OFBs are marked by white arrows. The time stamp format is m:s.

3.4 MICRO-TRANSPORTATION IN AN UNCOVERED RESERVOIR

3.4.1 INTRODUCTION

If the laser heating is able to provide a sufficient vertical component of the thermocapillary flow to counteract the buoyancy force, the OFB can stay in an uncovered reservoir. However, the absence of a cover also means the microgels could be lifted away from the OFB by the vertical component of thermocapillary flow, as described in Section 3.3.4. Thus, a mechanism is required to restrict the microgels to the surface of the substrate. Here, surface tension force resulting from controlling the liquid media thickness (Section 3.4.2) and magnetic force resulting from doping the microgels with magnetic particles were used to confine micro-objects on the substrate (Section 3.4.3).

3.4.2 PATTERNING OF MICROGEL RESTRICTED BY SURFACE TENSION FORCE

The first way to restrict the microgels on the uncovered reservoir is by the meniscus of the liquid. In Fig. 3-6, agarose hydrogel beads (diameters of approximately 100 μm) laden with NIH-3T3 mouse fibroblasts were assembled by the OFB. The fibroblast cell was selected to represent cells used in patterning *in vivo* tissues [103]. Prior to the experiment, the cells were cultured in Dulbecco's Modified Eagle Medium (DMEM) supplemented with 10% bovine serum (ATCC), 100 U/ml penicillin, and 100 μg/ml streptomycin (Sigma-Aldrich) at 37 °C in 5% CO_2. At the time of the experiment, cells were detached from the surface of the tissue culture flask by trypsin-EDTA (ATCC). Agarose microgel beads were made by the same method described in Section 2.6with a cell concentration of 1×10^7 cells/ml.

The medium is a PBS solution containing 5% PEGDA with 0.2% 2-Hydroxy-4-(2-hydroxyethoxy)-2-methylpropiophenone (Sigma-Aldrich) as the photoinitiator. Before experiment, it was adjusted to a thickness of approximately 200 μm. This thickness was found to be able to confine the microgels (with diameters around 100 μm) on the substrate, and allow the microgels to be transported by OFBs with diameters of approximately 20 μm. Under these conditions, the OFB was used to pattern thirteen microgel beads into an “H” shape in less than three minutes (Fig. 3-6a-d). After the transportation, the PEGDA was gelled by UV polymerization to fix the beads in place

(Fig. 3-6). Cell viability was then evaluated using the LIVE/DEAD cell viability/cytotoxicity kit (L-3224, Invitrogen). A 50-µl aliquot of the working solution, containing 1 µM calcein AM and 2 µM EthD-1, was dispensed onto the PEGDA gel. The gel was kept at room temperature for 40 minutes before being examined under a fluorescent microscope. Fifteen of sixteen cells fluoresced green, indicating that they are viable. The remaining cell fluoresced red, indicating that it is not viable. Subsequent cell viability tests showed a viability of 86% among the assembled cells (Fig. 3-6f), which is consistent with other cells in the sample.

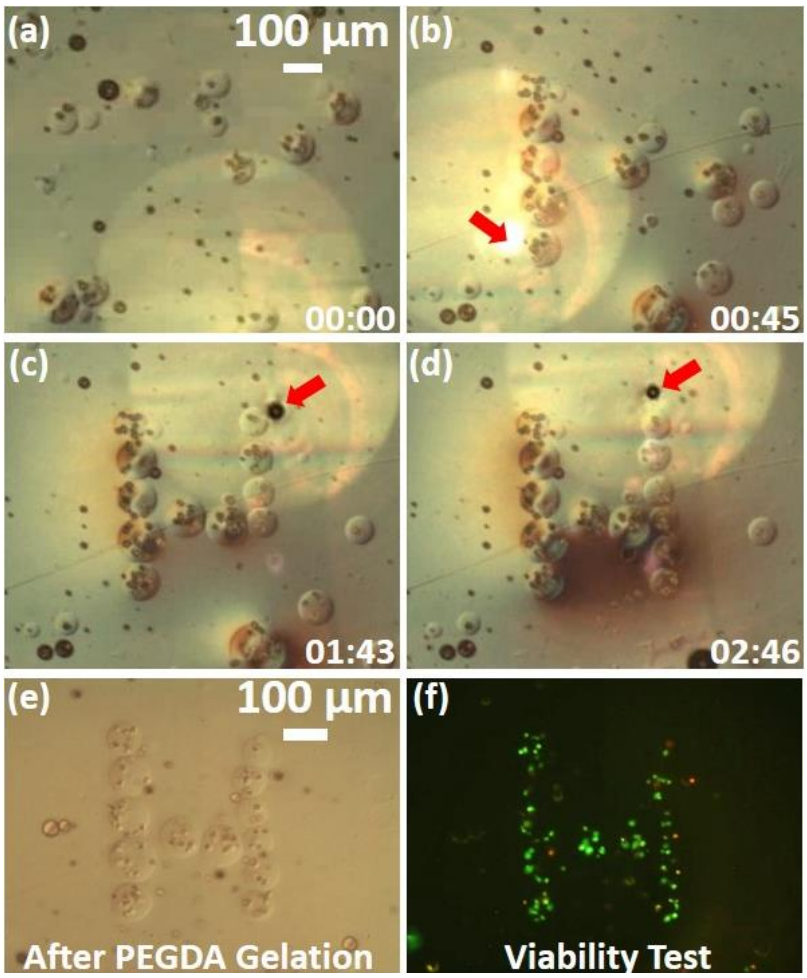

Fig. 3-6 Patterning of agarose microgels laden with NIH-3T3 cells restricted by liquid meniscus. Red arrows indicate the position of the OFB. The laser was turned off in (c-d) to show the position of the bubble. The time stamp format is m:s. (a-d) The patterning process. (e) The assembled microgels after polymerizing the PEGDA solution. (f) Cell viability test. Live cells fluoresce green, while dead cells fluoresce red.

3.4.3 PATTERNING OF MICROGELS RESTRICTED BY MAGNETIC FORCE

Microgels can also be anchored to the surface of the substrate after being doped with magnetic particles. To make these microgels, the emulsion method described in Section 2.6was modified. In this experiment, the microgel bead is made by mixing collagen reconstitution solution and 4% agarose at 1:1 ratio. The collagen is used to promote cell spreading and proliferation [91]. Before the process, the collagen reconstitution solution (Collagen Gel Culturing Kit, Type I-A, Nitta Gelatin Inc., Osaka, Japan) was made as described in ref. [104]. Medium with cells (volume = 7 ml) was harvested by the same method described in Section 3.4.2and put into a 15-ml test tube. A 2.5-µl aliquot of solution with magnetic particles (particle mass concentration: 40 ~ 55 mg/ml, amino functionalized, Fluka) was added to the cell solution. The magnetic particles contribute to anchoring microgels by increasing its mass and responding to magnetic fields. The mixture was centrifuged at 1500 rpm/s for 5 minutes to get 50-µl aliquot, with cell present in the solution. A 100-µl volume of 4% agarose solution (Sigma Aldrich, Type IX) and 100 µl of collagen reconstitution solution were added to the cell/magnetic particle solution, sequentially. The final cell concentration was approximately 1×10^8 cells/ml. Droplets were then made by emulsifying the cell solution in FC-40 oil, as described before. The emulsified mixture was then put into the freezer and kept at 0 ℃ for 15 minutes to gel the agarose, and then the mixture was transferred into the incubator for another 15 minutes to gel the collagen at 37 ℃. The microgel beads were then separated into the cell culture medium by centrifuging, and the beads in the medium were put into the incubator for further culturing.

Before the experiment, a 1-ml aliquot of the cell culture medium carrying the microgels was pipetted into a 2-ml test tube, and 1 ml of PBS was added. The test tube was centrifuged at 4000 rpm/s for 30 seconds and the upper solution was aspirated away, leaving only the microgels. PBS was then added to fill the tube. This process was performed to clean the microgels, enabling more reliable OFB actuation. Direct actuation in cell culture medium is currently under evaluation.

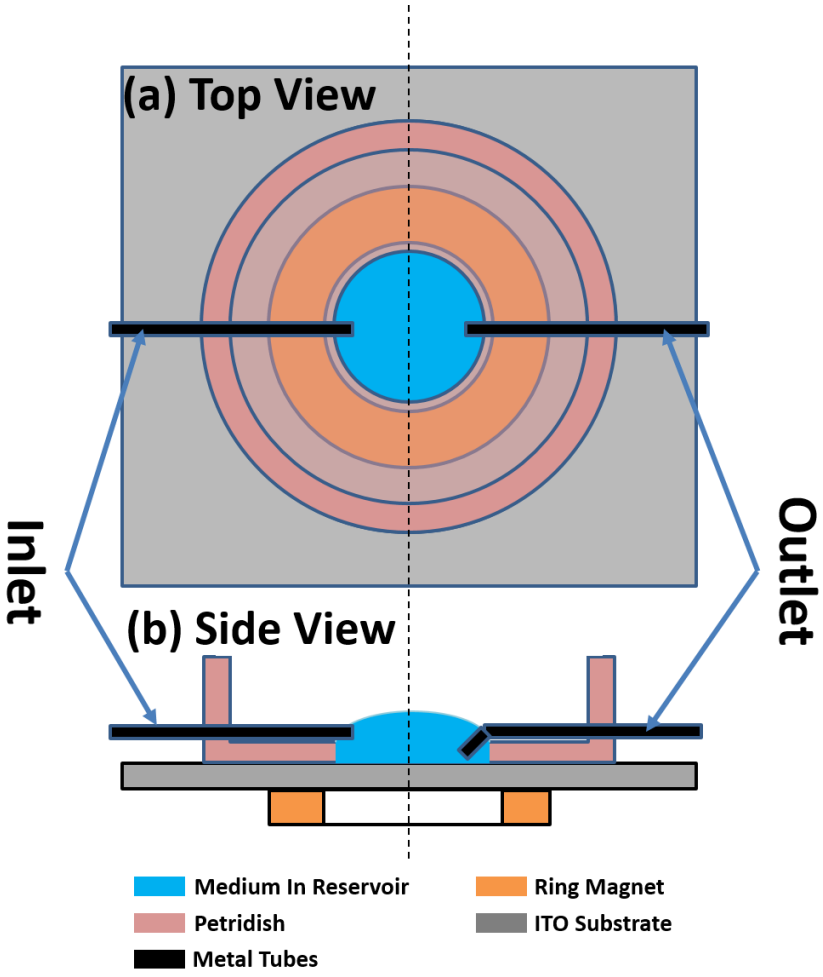

Fig. 3-7 Device for patterning and culturing of the microgels doped with magnetic beads. The reservoir has a diameter of 20 mm. (a) Top view. (b) Side view.

The device for this experiment is shown in Fig. 3-7. A hole with 20 mm diameter was drilled on the bottom of a petri dish (35 mm × 10 mm, tissue culture dish, Falcon). A fluid reservoir was formed by bonding the petri dish onto an ITO substrate using epoxy. A neodymium ring magnet (N40, CMS Magnetics®) with 3" × 1.65" × 0.5" (outer diameter ×inner diameter × thickness) dimension was attached to the backside of the ITO substrate by double-sided polymide tape (Kapton tape, DuPont), with the center of the magnet aligned with the center of the reservoir to minimize the effects of any lateral magnetic fields on the microgels. The reservoir was first filled with 500 µl PBS, and then a 50-µl aliquot of the PBS with microgels was pipetted in the center of the reservoir.

Fig. 3-8a-c shows the transportation process. To visualize the bubble better, an 800-nm dichroic shortpass filter (#69-208, Edmund Optics) was added to the front of the camera to filter out the laser illumination. Thus, no light beam is observed in the photos. The OFB under control is magnified in Fig. 3-8a and marked by black arrows in Fig. 3-8b,c. During the transportation, the OFB may get stuck by hydrogel debris lodged on the substrate. Thus, many OFBs exist in the working space as shown in Fig. 3-8b,c. If an OFB becomes unresponsive, a new OFB can be generated immediately, and used continue the transportation.

The patterning process took approximately 10 minutes. After the assembly, the PBS inside the reservoir was replaced by the collagen reconstitution solution, by flowing in the new solution at a rate of 2 ml/h. Due to the magnetic field, the microgels remained in place during the flush process, keeping the patterned shape intact (Fig. 3-8d). After about 15 minutes, the PBS was totally replaced by the collagen reconstitution solution. Two sides of the ITO substrate were then connected to DC power supply. Current from the power supply was used to increase the temperature of the reservoir by resistive heating of the ITO. The temperature inside the reservoir was kept at 32 °C (measured by a thermocouple) for 15 minutes to gel the collagen on-chip. After this, a 1-mm-thick 4% agarose was poured onto the collagen, and gelled by storing in a freezer for 5 minutes. This agarose layer helped to keep the collagen from mechanical damage when the reservoir was moved. After this step, the microgel pattern fixed inside the hydrogel is shown in Fig. 3-8e. At last, cell culture medium was poured on top of the agarose hydrogel, and the device was put into the incubator for culturing. The patterned cells were already fixed in the gel. After culturing for one day, the cells inside the microgel beads began to multiply and migrate away from the microgels (Fig. 3-8f). The cell growth in 3D is also shown in (Fig. 3-9).

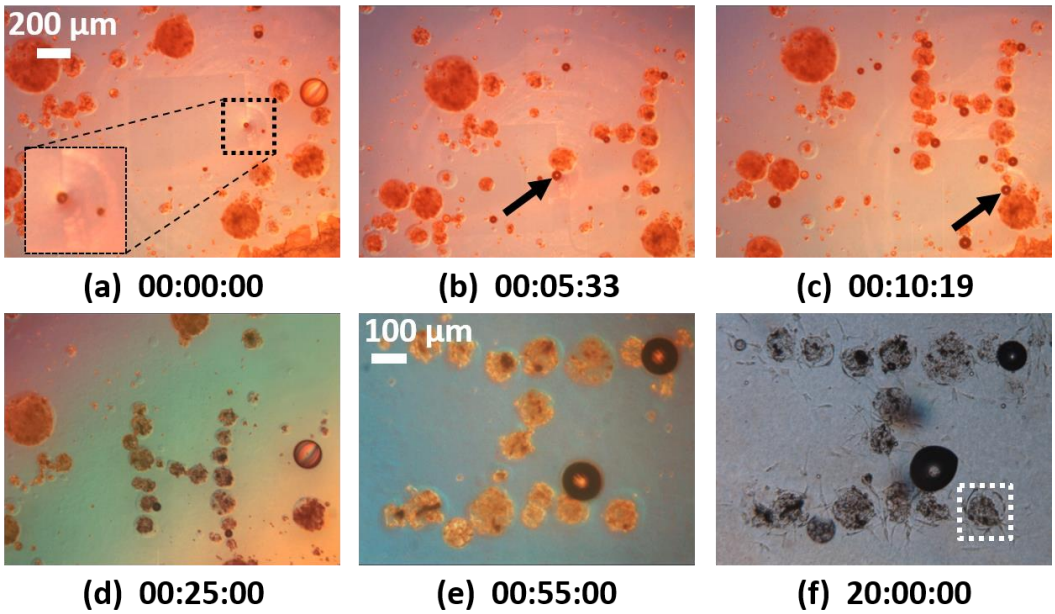

Fig. 3-8 Patterning and culturing of NIH-3T3-cell-laden laden microgels doped with magnetic beads. The OFB being addressed is magnified by the inset in (a). Their positions are indicated by black arrows in (b), (c). Other bubbles in the environment are old OFBs stuck by hydrogel debris. A low pass filter is fitted to the front of the camera to block the laser beam. The time stamp format is h:m:s. The length scale at (a) applies for (a-d) while the one in (e) applies for (e-f). (a-c) The patterning process. (d) The pattern after being covered by collagen reconstitution solution. (e) The pattern after the collagen and agarose gelation. (f) After one day, cells started to multiply and migrate inside the collagen matrix. The microgel bead marked by white dots is magnified and shown in Fig. 3-9.

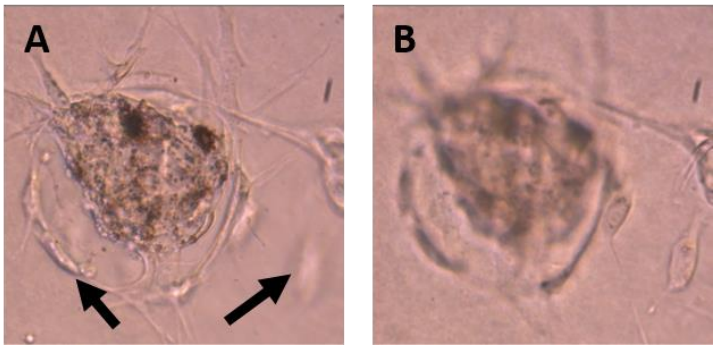

Fig. 3-9 Cells growth in 3D in gelled collagen. The microgel bead is the one marked by white dots in Fig. 3-8f. Cells at different heights are marked by black arrows.

3.5 MICRO-TRANSPORTATION OF SINGLE CELL IN AN UNCOVERED FLUID RESERVOIR

3.5.1 INTRODUCTION

Cells in microgels are usually protected by the hydrogel and not in direct contact with the OFB during transportation. In contrast, when transporting cells in solution, physical contact transportation may be a concern, as shear stress may exist when the cell membrane touches the air-liquid interface [105][106]. Thus, non-contact cell transportation using thermocapillary flow is an attractive method of micro-transportation.

In this section, we show that the OFB is capable of non-contact transportation of single cells on a substrate. Yeast (diameter of approximately 7 μm) and mouse fibroblasts (diameter of approximately 20 μm) were transported and patterned by the thermocapillary flow around OFB, hereafter referred as the OFB single-cell transporter. To transport these bio-micro-objects, localized thermocapillary flow must be generated around OFB to prevent disturbing neighboring objects. To achieve this, OFB with diameters of less than 1.5 μm were generated by laser pulses, and used for micro-transportation.

3.5.2 EXPERIMENT SETUP

The OFB single-cell transporter is shown in Fig. 3-10. An ITO-coated slide (sheet resistance of 4 to 10 ohms, Delta Technologies), consisting of 1-mm-thick glass topped by a 200-nm-thick ITO layer, was placed under the microscope as the substrate. The continuous-wave 980-nm laser (Laserlands) was focused by a plano-convex lens (Newport KPX088) and a 20X objective (Meiji S. Plan M20X, NA: 0.4) onto the substrate, forming a spot with a diameter of 3.87 μm at full-width, half-maximum. The laser was switched on and off by a TTL signal from a function generator (Agilent 33220A). When the laser was on, the intensity was measured to be 414 kW/cm^2. In comparison, the operational intensity of the optical tweezers is usually on the order of megawatts per square centimeters [31].

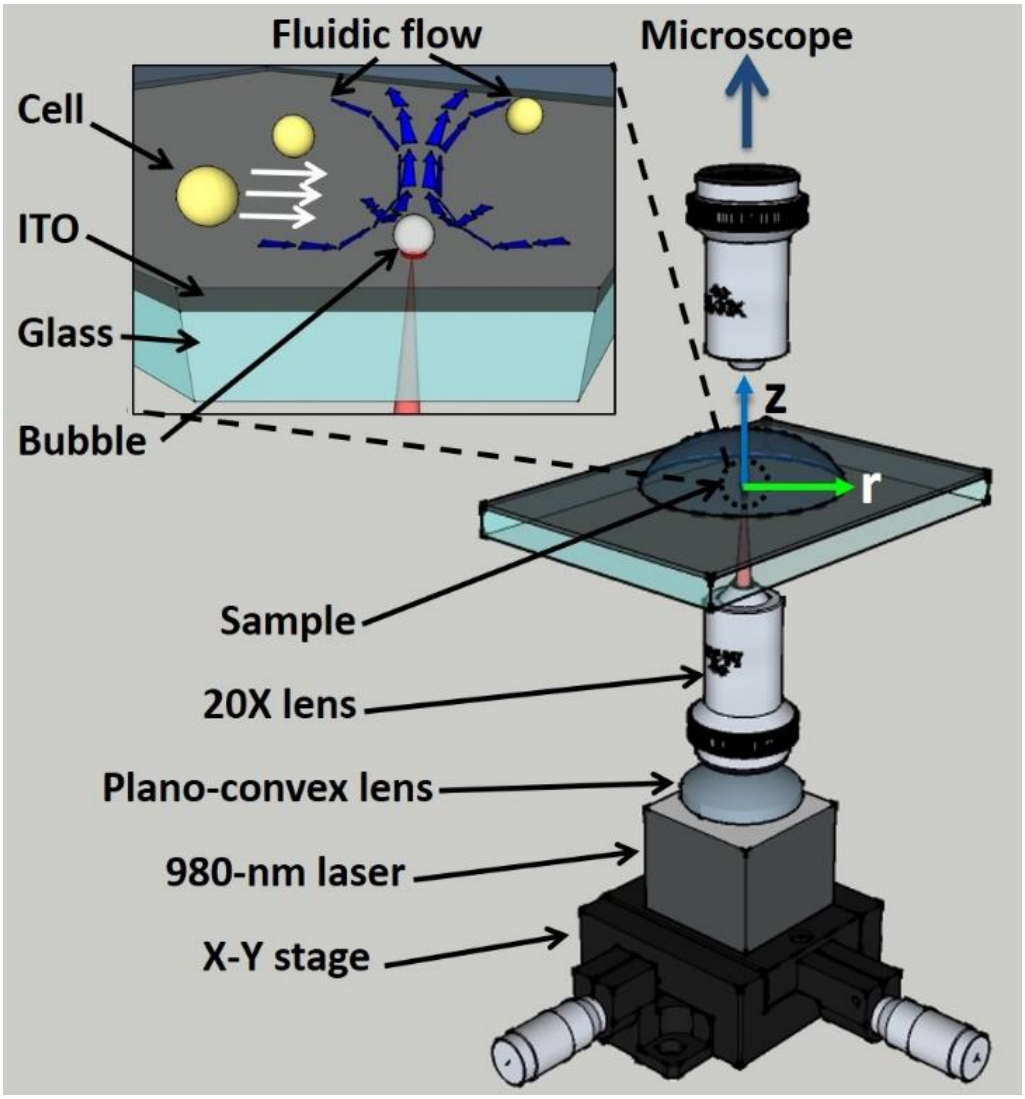

Fig. 3-10 Experimental setup of the OFB single-cell transporter in water. The inset shows a magnified view of the ITO substrate and the toroidal thermocapillary convection around the OFB. Note that the OFB is in an uncovered fluidic reservoir.

3.5.3 OFB AND ASSOCIATED THERMOCAPILLARY FLOW

3.5.3.1 SIMULATION

As described before, when an air bubble on the substrate of a liquid reservoir is subjected to a temperature gradient normal to the substrate, thermocapillary convection can form around the bubble. In Fig. 3-11, the relationship between the bubble size and the lateral scale of the thermocapillary flow was simulated by finite-element modeling in COMSOL Multiphysics. The model geometry is shown in Fig. 3-11a. In Fig. 3-11b, the horizontal steady-state fluid velocities are plotted as a function of distance from the

OFB center, measured along the white dashed line in Fig. 3-11a for three different bubble radii (5.0 µm, 2.5 µm, and 0.5 µm). The graph shows that the strength of the thermocapillary flow increases with bubble size, so a larger bubble has a wider horizontal influence. In Fig. 3-11c, similar horizontal fluid velocities for a hemispherical bubble with a 0.5-µm radius in water and 1% agarose solution are plotted. The increased viscosity of the agarose solution affects the thermocapillary flow velocity, making the range of horizontal flow smaller. The Marangoni numbers were calculated by the equation given in [107].

$$\mathrm{Ma} = -\left(\frac{\partial \sigma}{\partial T}\right) \times \frac{T_{diff}}{\mu \alpha} \times \frac{R_b^2}{H} \qquad \text{Equation 3-2}$$

In equation Equation 3-2, $\left(\frac{\partial \sigma}{\partial T}\right)$ is the temperature derivative of surface tension, T_{diff} (K) is the temperature difference in the system, μ is the dynamic viscosity (N▪s/m^2), α (m^2▪s^{-1}) is the thermal diffusivity, H (m) is the liquid layer height, R_b (m) is the bubble radius. The Marangoni numbers are 23.26, 5.81, and 0.23 for a bubble radius of 5.0 µm, 2.5 µm, and 0.5 µm, respectively in water (Fig. 3-11b), and it is 0.03 for a 0.5 µm-radius bubble in 1% agarose (Fig. 3-11c) [107]. These results agree with that that reported by B. K. Larkin [81], in which smaller Marangoni numbers lead to a more localized thermocapillary convection.

In order to make a fair comparison of the flow velocities for different bubble sizes, each case must experience the same temperature gradient. Thus, for this simulation, the entire lower boundary is held at a constant temperature. (In the real experiment setup, the temperature gradient is more realistically modeled as a Gaussian curve centered at the origin, but this would mean that bubbles of different sizes would have different temperature gradients at their surfaces.) Both conductive and convective heat transfer are considered outside the bubble. The fluid mechanics and convective heat transfer inside the bubble are ignored. The boundary condition on the bubble surface is set to Equation 1-1. The rest of the boundary conditions are indicated in Fig. 3-11. The properties of the media are listed in Table 2.

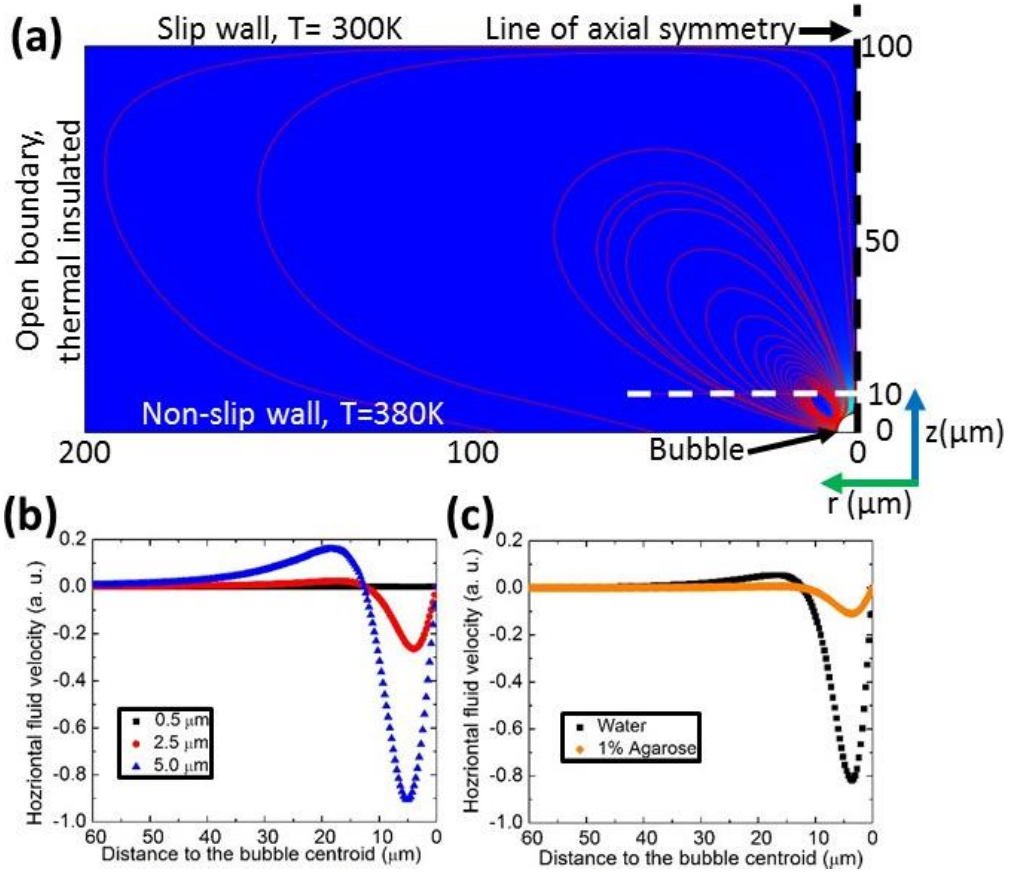

Fig. 3-11 Simulation of the thermocapillary flow around the OFB single-cell transporter in water.(a) Simulation of the thermocapillary flow around a 5-μm-radius hemispherical bubble centered at the origin. (b) The horizontal fluid velocity as a function of distance from the OFB center, measured along the white dashed line in (a) for different bubble sizes. The media simulated here is water. Positive velocities indicate fluid moving towards the origin. (c) The horizontal fluid velocity for a hemispherical OFB (diameter = 1 μm), in media with two different viscosities: water and a 1% agarose solution.

Table 2 Properties of gas (air) and water at 25 ºC [87] *used for the simulation shown in Fig. 3-11. Other parameters used include* $\gamma_T = 0.148\ mN{\cdot}m^{-1}{\cdot}K^{-1}$ [79] *and* $\eta_{agarose} = 7\ mPa{\cdot}s$ [38].

Property	Air	Water
ρ (Density)	1.161 $kg{\cdot}m^{-3}$	0.997 $kg{\cdot}m^{-3}$
η (Dynamic viscosity)	Not used	0.89 mPa·s
λ (Thermal conductivity)	0.026 $W{\cdot}m^{-1}{\cdot}K^{-1}$	0.607 $W{\cdot}m^{-1}{\cdot}K^{-1}$
Cp (Specific heat)	1007 $J{\cdot}kg^{-1}{\cdot}K^{-1}$	4181 $J{\cdot}kg^{-1}{\cdot}K^{-1}$

3.5.3.2 EXPERIMENT RESULTS OF BUBBLE GENERATION

The thermocapillary flow is used by the OTMm to transport cells in non-contact style (Fig. 3-12, inset). According to the measurement of the optical power meter, approximately 16% of the optical energy is absorbed by the 100-nm-thick ITO layer and converted into heat. This laser-induced heating is used to generate a bubble in the liquid medium above the ITO layer.

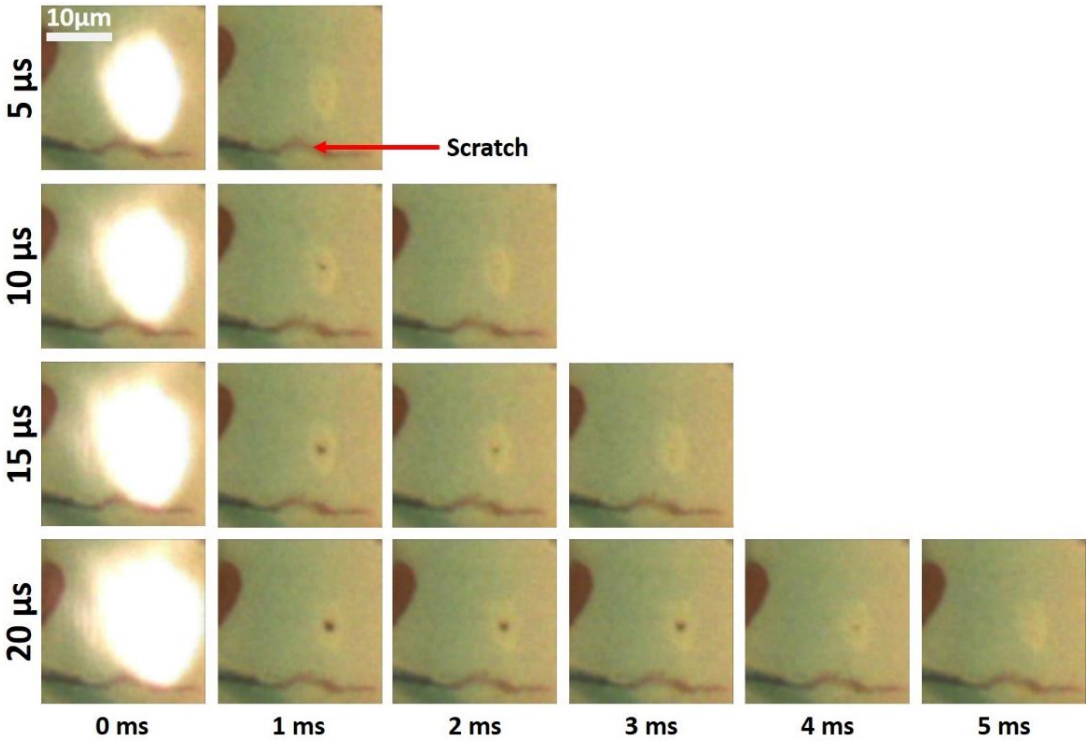

Fig. 3-12 OFB generation by four different laser pulse widths. The bubbles were generated near a scratch on the surface of the ITO-coated glass. The video was recorded at 1000 frames per second.

The size of the generated bubble reduces with the decreasing pulse width in Fig. 3-12. The bubble diameters were about 1.5 μm, 1 μm, and 0.6 μm for pulse widths of 20 μs, 15 μs, and 10 μs, respectively. Smaller bubbles dissolved into the liquid more rapidly; bubbles disappeared within 5 ms, 3 ms, and 2 ms for pulse widths of 20 μs, 15 μs, and 10 μs, respectively. When the pulse width was 5 μs, the bubble dissolved too rapidly to be observed with the camera used to record these images. Since it only took less than 3 ms for a bubble generated by a 15-μs laser pulse to dissolve, and the shortest period

between bubble generation events in later experiments was 10 ms (100 Hz), all the generated bubbles had enough time to dissolve before the next pulse.

Once the bubble is created, the temperature gradient on the bubble surface, which is hotter close to the substrate and cooler on the bubble apex far away the substrate, generates a toroidal opto-thermocapillary flow around the bubble (Fig. 3-10, inset). When the laser is turned off, the opto-thermocapillary flow immediately ceases due to the absence of the temperature gradient, and the bubble quickly dissolves into the medium due to the large Laplace pressure across its surface. In all the experiments discussed here, sufficient time elapses between laser pulses for the bubbles generated by each laser pulse to completely dissolve into the liquid (Fig. 3-12)

3.5.4 OFB SINGLE-CELL MICRO-TRANSPORTER MECHANISM

3.5.4.1 CELL MOTION IN THE THERMOCAPILLARY CONVECTION

In order to track the motion of the cell in the thermocapillary convection, a 20-μm-diameter bead used as a model. Before tracking the bead trajectory, a method to determine the z-direction displacement of micro-object was needed (Fig. 3-13). To achieve this, the centroid brightness of the bead was recorded for different z-direction displacements, achieved by adjusting the specimen stage of the microscope using a Vernier micrometer (SM-25, Newport). The brightness of the image at the center of the bead was extracted using ImageJ software, and correlated to the z-direction displacement.

Once the bead brightness was correlated to z-position, the bead was circulated around OFB. Fig. 3-13b shows a bead as it circulated back to the substrate surface. The circulating bead had an obvious z-displacement change corresponding to a centroid brightness change, and a lateral displacement during this process. In comparison, the other bead visible in this sequence has almost zero motion, due to stiction to the surface.

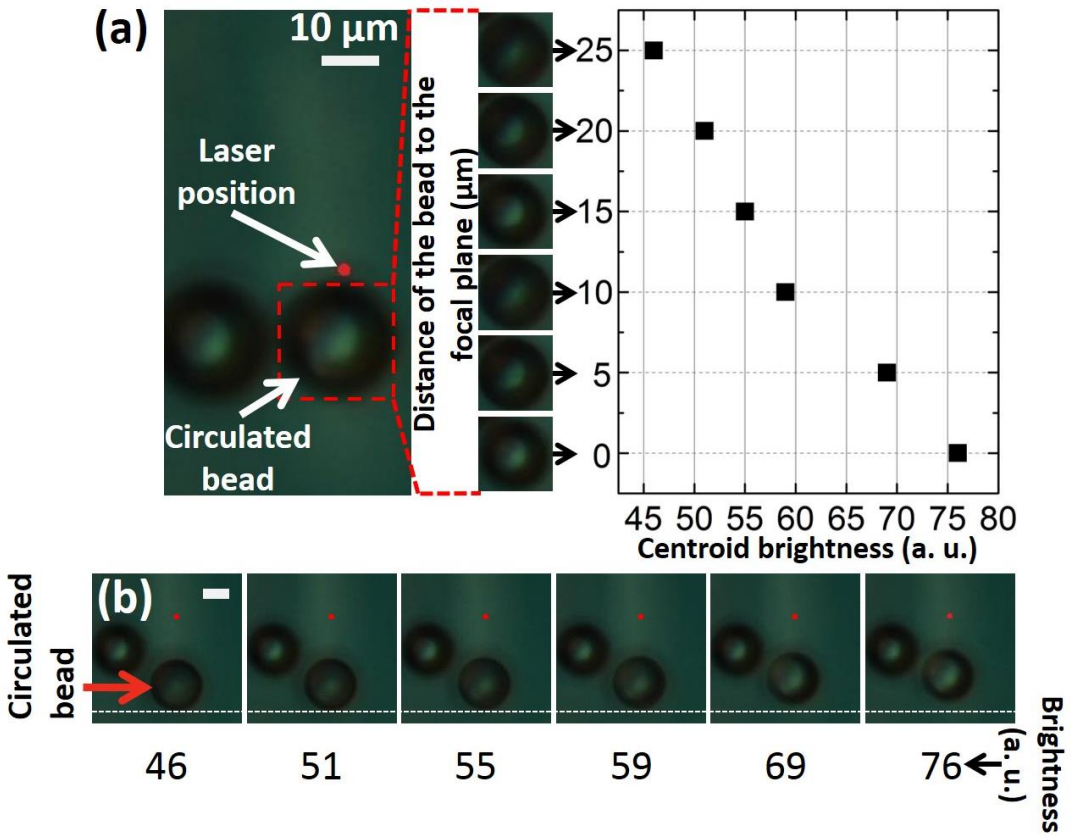

Fig. 3-13 Vertical displacement of a polystyrene bead (diameter =20 µm) in the z-direction correlated to bead centroid brightness. The laser pulse frequency is 20 Hz and the pulse width is 15 µs. The laser position is marked by a red dot. (a) Measurements of the reference bead centroid brightness when the laser is off. (b) Vertical displacement of the bead during circulation around OFB. The centroid brightness of the circulated bead is marked below each frame. The white dashed line is the reference line to detect the position of the beads. The scale bar is 10 µm.

To quantify the motion of a micro-object subjected to the opto-thermocapillary flow, the movement of a 20-µm-diameter polystyrene bead was tracked while it circulated in the flow generated by laser pulses with a width of 15 µs at a frequency of 20 Hz (Fig. 3-14a). The bead circulates clockwise in the thermocapillary flow, following the trajectories plotted in Fig. 3-14a. The dotted lines marked an artifact by using the brightness measurement method in Fig. 3-13. This artifact was due to the reflective emitting surface of the laser diode, which made the background of the region near the laser spot brighter, as shown later in Fig. 3-20b. Thus, a bead would appear to be brighter when closer to the laser spot, and darker when it was away from the laser,

causing the evaluation of the z-displacement of the bead far away from the laser spot (25~30 μm) to be measured as larger than the actual value. This artifact causes the spike in the z-displacement of the microbead as it circulates away from the laser, as shown in Fig. 3-14a. There is no similar artifact when the bead is close to the laser spot, as this corresponds to the position of the bead during the initial correlation between the bead brightness and the z-displacement.

Fig. 3-14b shows the instantaneous velocity of the bead at different locations along the 15 μs trajectory in Fig. 3-14a. The instantaneous velocity is decoupled into horizontal velocity (V_r) and vertical velocity (V_z) components. A positive V_r refers to bead moving towards the bubbles, while a positive V_z refers to the bead moving upwards and away from the substrate. V_r and V_z have positive and negative values since the bead was circulating around the bubbles. At the section marked by "Sub-flow region" in Fig. 3-14a, the bead had the highest V_r towards the cavitation bubble and a negligible V_z (Fig. 3-14b). This is the region of the thermocapillary flow used for the non-contact single cell transportation. If the bead was too close to the bubble ($r \leq 5$ μm in Fig. 3-14a), it entered a region with high V_z moving upwards and away from the substrate (Fig. 3-14a), so the bead was circulated away from the bubble.

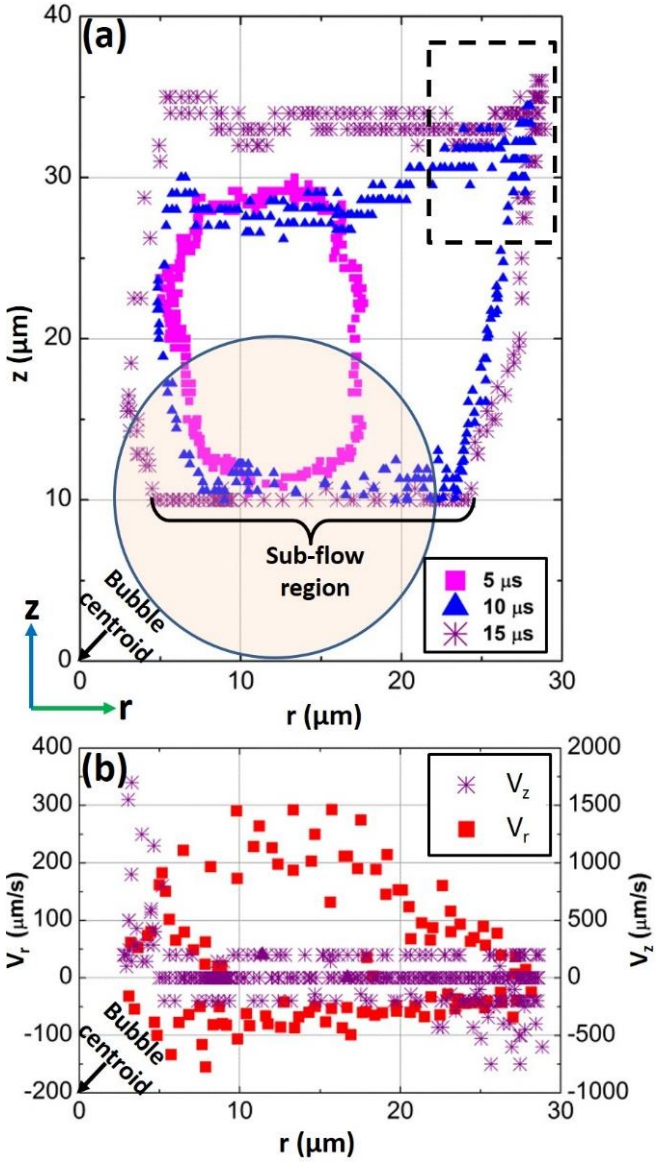

Fig. 3-14 Side view of a polystyrene bead (diameter =20 μm) motion in the toroidal opto-thermocapillary flow around the OFB single-cell transporter. The bubble was generated at the origin in these graphs. (a) The motion of the bead in an r-z plane, as it circulates around OFB, using various laser pulse widths. A circle with 20-μm diameter is drawn on the graph to show the size of the bead. The portion of the overall bead trajectory that is used for transportation is labeled as the "sub-flow region." An artifact in the measured bead motion is apparent in the portion of the trajectory bounded by the black dashed lines, and is explained early in this section. (b) The measured horizontal (V_r) and vertical (V_z) instantaneous velocity of the bead as a function of horizontal displacement along the r-direction. The laser pulse frequency was 20 Hz and the pulse width was 15 μs.

3.5.4.2 MICRO-TRANSPORTATION MECHANISM

Based on the motion of micro-objects in the convection around OFB, a non-contact transportation mechanism was developed, and is shown in Fig. 3-15. Initially, the laser is positioned so that the bead can experience the part of the opto-thermocapillary flow that is closest to the substrate (step i in Fig. 3-15a). The laser is then briefly turned on, generating a bubble and opto-thermocapillary flow, moving the bead a small distance, D_O (step ii in Fig. 3-15a). The laser then turns off and the bubble that was generated dissolves into the liquid. The opto-thermocapillary flow also ceases, along with the motion of the bead. While turned off, the laser moves a displacement distance, D_L (step iii in Fig. 3-15a). This completes a transportation period; repeating this process can continuously drag the bead in the direction of the laser. Fig. 3-15b shows the bead and laser displacements during two consecutive laser pulses. The first four images form a complete transportation period. The bead moved a distance D_O during the first period. The bead had no observable motion when laser was off (between the 10 ms and 50 ms frames in Fig. 3-15b). The bead moved another distance D_O in the first part of the second transportation period (50 to 60 ms). The laser pulse frequency was 20 Hz and the pulse width was 15 μs.

If $D_L = D_O$ is maintained during the transportation by the OTMm, the bead will follow the laser at a constant velocity. However, if $D_L > D_O$ due to rapid laser motion, the bead will not be properly positioned in the opto-thermocapillary flow, and will fall behind and stop moving after several transportation periods. On the other hand, if $D_L < D_O$, the bead will move closer to the laser-induced bubble in every period. When the bead is too close to the bubble, it circulates upwards and away from the bubble surface. In this scenario, the transportation needs to be temporarily suspended. The laser should stop moving until the bead is re-circulated back to the thermocapillary flow region that is closest to the substrate; after that, transportation can resume.

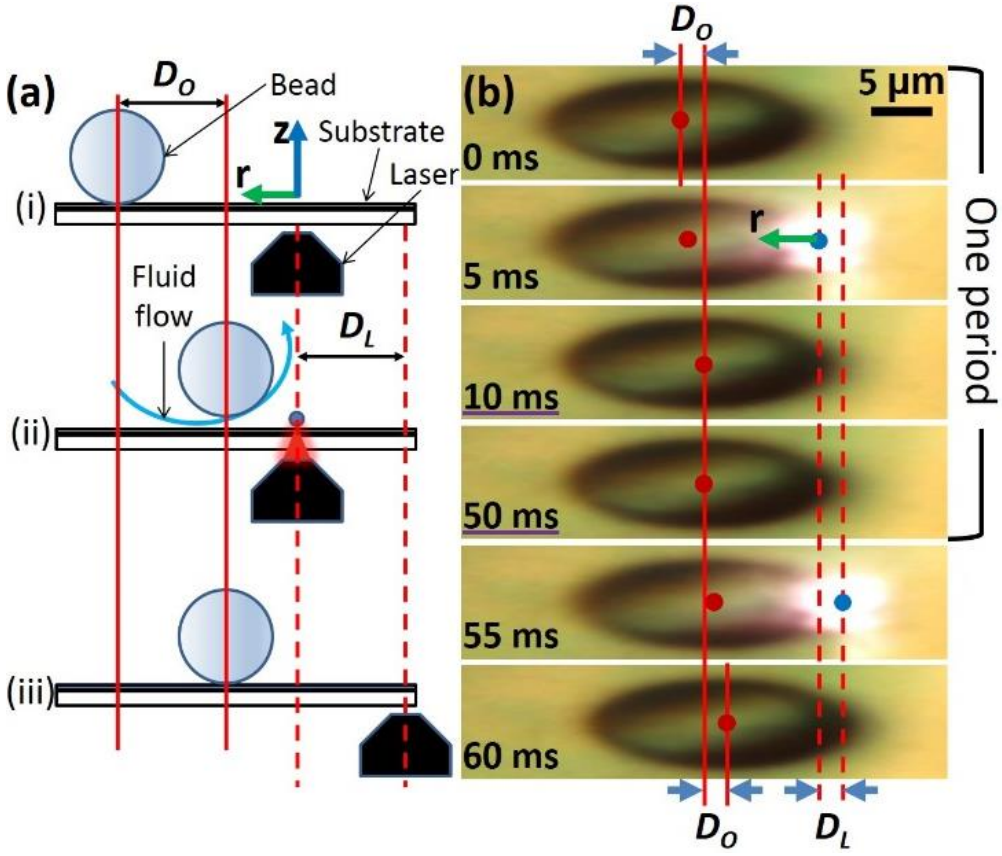

Fig. 3-15 OFB single-cell transportation mechanism. (a) A side-view illustration of one transportation period of a micro-bead. i) The micro-bead position immediately before the laser is turned on. The coordinate axes match the ones shown in Fig. 3-10. ii) The laser is on, creating a bubble and opto-thermocapillary flow, moving the bead a distance of D_O. iii) The laser is off, stopping the flow and the bead movement, while it translates to the next illumination point. (b) Top view of the observed motion of a 20-μm-diameter bead. The bead centroid and laser spot are marked by red dots (●) and blue dots (●), respectively. The photos have been stretched three times in the x-direction to magnify the displacements. The r-axis is marked in the second frame, and the z-axis is normal to the plane of the page.

Using this mechanism, a 10-μm-diameter polystyrene bead can be pulled around a feature on the substrate by moving a pulsed laser relative to the substrate (Fig. 2a). The laser pulse used has a width of 60 μs at a frequency of 60 Hz. The substrate is coated with a 1-μm-thick layer of α-silicon, giving it the same structure as the substrates used in Section 2.2. The average intensity at the laser focal point is 508 kW/cm^2 for this

experiment. Thus, the transportation velocity is higher than the experiment on bare ITO, due to the higher light absorption of the substrate with the α-silicon coating.

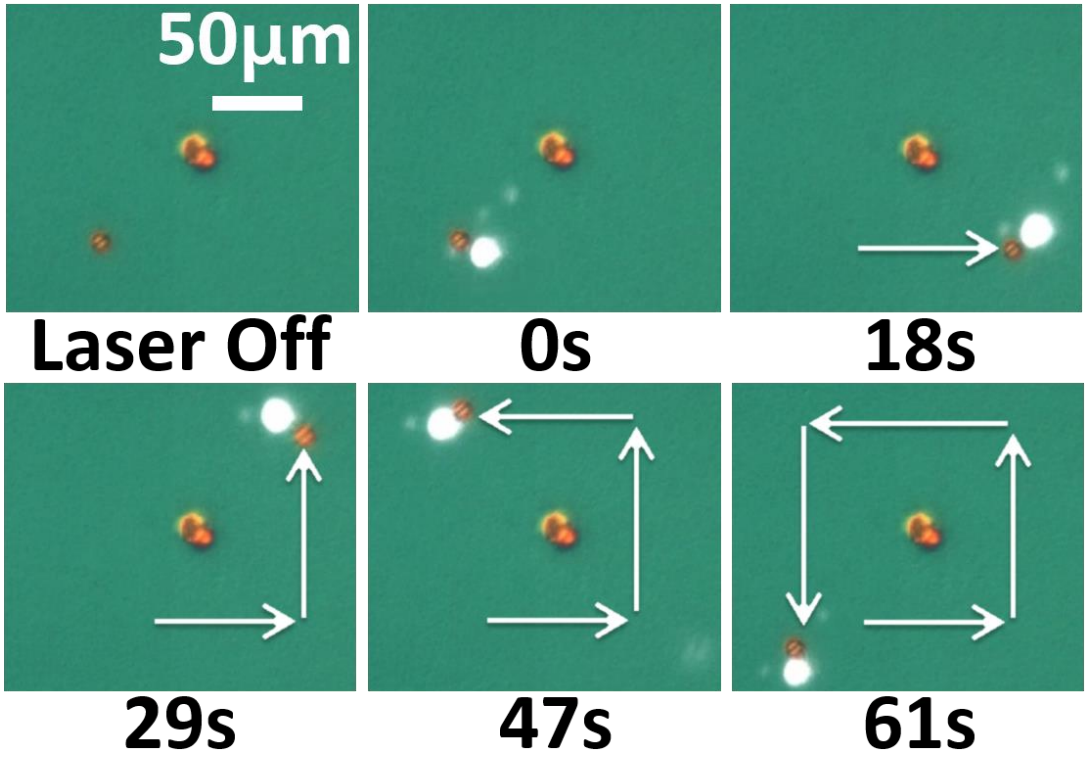

Fig. 3-16 Transportation of a 10-μm-diameter polystyrene bead in 1.5% agarose solution by OFB single-cell transporter. The bead (the smaller object in the image sequence) was pulled around a feature on the substrate (the larger object in the center of the images).

3.5.4.3 MICRO-TRANSPORTATION RESOLUTION

The resolution of the 20-μm bead transportation is revealed by the horizontal scale of the circulation in Fig. 3-14a. For example, when the pulse width is 15 μs, the maximum horizontal displacement of the bead is 30 μm, so the thermocapillary flow will not disturb another 20-μm-diameter bead located farther than 30 μm away from the laser spot. If the bead has settled down onto the surface of the substrate, the minimum distance to the laser spot without any disturbance can decrease to 20 μm due to the friction of the substrate (Fig. 3-13b). Thus, in order to initiate the circulation of the bead, the laser should move closer to the bead. For example, the laser should be within 10 to 20 μm of the bead for a laser pulse width of 15 μs. This will cause the bead to move and follow the trajectory shown in Fig. 3-13a. The resolution decreases when

using a smaller laser pulse width, which causes a smaller maximum horizontal displacement.

3.5.4.4 MICRO-TRANSPORTATION VELOCITY

To transport micro-objects at higher velocities, a longer laser pulse width or a higher pulse frequency can be used. This was experimentally verified by measuring the transport velocity of 20-µm-diameter polystyrene beads over a distance of 200 µm for different laser pulse widths (5 µs, 10 µs, 15 µs) and pulse frequencies (20 Hz, 40 Hz, 60 Hz, 100 Hz) (Fig. 3-17). Motorized linear actuators (850F-HS, Newport) were used to translate the laser at a constant velocity for this measurement.

The transportation velocity increases with increasing laser pulse width due to a longer D_O in each period, moving the object further per laser pulse. A higher laser pulse frequency means that the sequence shown in Fig. 3-15a repeats at a faster rate, so theoretically the transport velocity of an object and the frequency (y and x respectively in Fig. 3-17) should increase at the same rate (y/x = constant). To verify this, the linear function $y = ax+b$ was used to fit the data of each pulse group. The errors for each point are used as instrumental weights, so data points with larger errors are less important in the fitting process. Thus, the y-intercepts should be nearly zero for y/x=constant, as shown on all the three fit lines in Fig. 3-17.

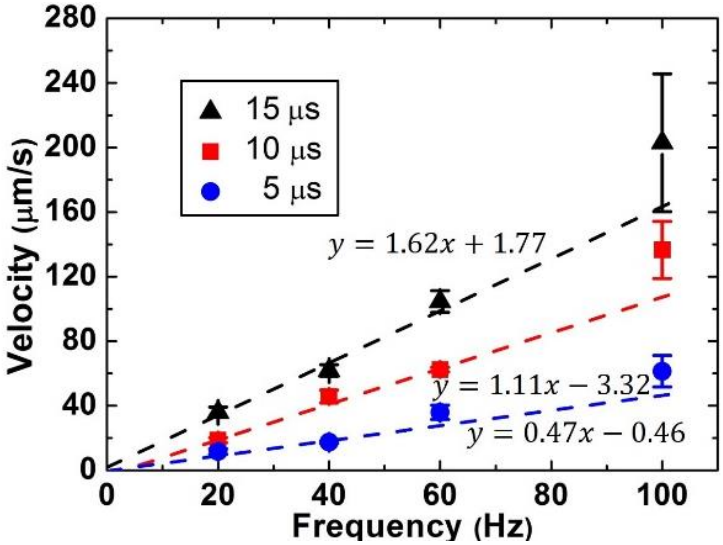

Fig. 3-17 Measured transportation velocities of a bead (diameter = 20 µm) for varying laser pulse frequencies and pulse widths. Each point represents an average of three measurements, and the error bars represent the standard deviations. The function y = ax+b is used to fit the data in each frequency group.

3.5.4.5 TEMPERATURE DISTRIBUTION DURING MICRO-TRANSPORTATION

The generation of thermocapillary flow requires a temperature gradient, which is a concern for a transportation system for living cells. Fortunately, the heat used to create the actuating bubble is rapidly dissipated, keeping the temperature below the maximum physiological temperature. It is challenging to precisely measure the temperature distribution of the fast-moving fluid under laser illumination in the microscale. To probe the temperature distribution around the OFB, two temperature-sensitive polymers were used (Fig. 3-18).

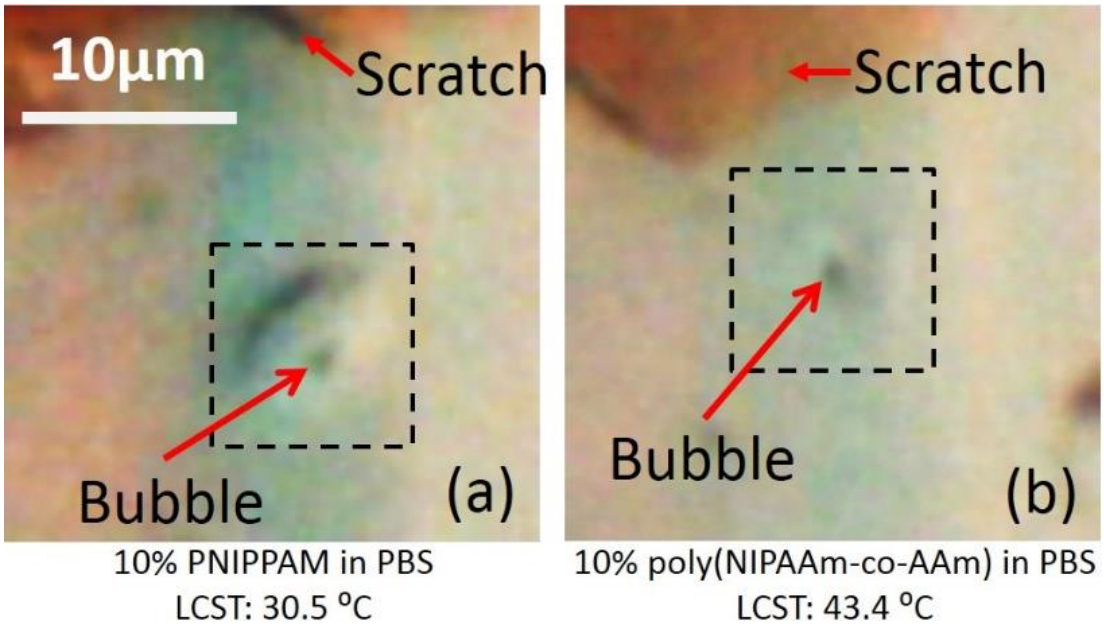

Fig. 3-18 Detection of the temperature profile around the OFB single cell transporter by (a) 10% w/v PNIPAAm in PBS, and (b) 10% w/v poly(NIPAAm-co-AAm) in PBS. The laser was set to a pulse width of 15 µs at 100 Hz, and positioned near a scratch on the substrate. The video was recorded at 1000 frames per second.

Solutions of 10% w/v PNIPAAm (Mw: 19,000-30,000, Sigma Aldrich) in PBS and 10% poly(NIPAAm-co-AAm) (Mw: 20,000-25,000, Sigma Aldrich) in PBS were used to probe the temperature distribution around the laser-induced bubble [108]. The laser pulse frequency was set to 100 Hz and the pulse width was 15 µs, representing the harshest conditions that the cells experience. The lower critical solution temperatures (LCST) of each solution were verified by a thermocouple (Type T probe, Omega

HH806AU). The PNIPAAm solution had an LCST of 30.5 ºC, and the poly(NIPAAm-co-AAm) solution had a higher LCST of 43.5 ºC. Gelation of each solution occurs if the temperature is greater than the LCST. Fig. 3-18 shows the gelation of PNIPAAm (Fig. 3-18a) and poly(NIPAAm-co-AAm) (Fig. 3-18b) immediately after a laser pulse. The radii of the gelled areas are about 3.5 µm and 2 µm, respectively. This indicates that the temperature was less than 43.4 ºC at a distance of 2 µm from the center of the laser spot, and less than 30.5 ºC at a distance of 3.5 µm from the center of the laser spot. For reference, 37 ºC is considered the physiological temperature for human cells.

However, there are limitations to the polymer-based temperature probing performed here that may lead to an overestimation of the temperature distribution around the bubble. First, the gelation of the temperature-sensitive polymers in Fig. 3-18 reduces the convective heat transfer around the bubble, contributing to a temperature increase around the bubble. Secondly, even if the effects of the gelation were ignored, both temperature-sensitive polymer solutions used here are more viscous than water, so the temperature distribution result should not be combined with the characterization results measured in water (Fig. 3-13) to evaluate the temperature impact on the 20-µm-diameter bead. Thus, during cell transportation in media with viscosity similar to water, such as PBS or DMEM, cells are circulated like in Fig. 3-13a, but the radius of the region with harmful temperatures greater than 37 ºC should be smaller than that in Fig. 3-13, due to the lower viscosity of the water. On the other hand, for cell experiments in more viscous media such as PEGDA or agarose pre-polymer, the radius of the region with harmful temperatures is closer to that in Fig. 3-18. However, at the same time, the increased media viscosity reduces the strength of the thermocapillary flow, as shown in Fig. 3-11, so the cells are not pulled as close to the laser-generated bubble as compared to the situation shown in Fig. 3-13a. Moreover, it should be noted that when the object is moving close to the bubble, its perpendicular velocity V_z increases sharply (Fig. 3-13b), reducing the negative impacts of the higher temperatures on the cell.

3.5.4.6 VIABILITY TESTS ON CELLS UNDER TRANSPORTATION

A more important and pragmatic evaluation of the impacts of temperature and thermocapillary flow on NIH-3T3 cells is to measure the cell viabilities after transportation. Fig. 3-19 shows a NIH-3T3 cell as it circulated around a bubble. The cells were in a 5% PEGDA pre-polymer mixture, prepared as described in Section 3.4.2.

The laser pulse frequency and pulse width were also set to be the same as that in the experiment shown in Fig. 3-18 (100 Hz, 15 μs). The cell was circulated around the bubble at least 20 times (a total duration of 10 to 15 seconds), compared to a circulation for a maximum of 10 times during the micro-transportation procedures described elsewhere in this paper. After this, the cell was fixed on the substrate by gelling the PEGDA. The viability test, described in Section 3.4.2, was performed immediately after the PEGDA gelation, and indicated that the cell was still alive. The same test was repeated on 108 cells in total. Of these, 106 cells were observed to be viable, corresponding to viability of over 98%. The two negative cases may due to the selection of cells that were already dead.

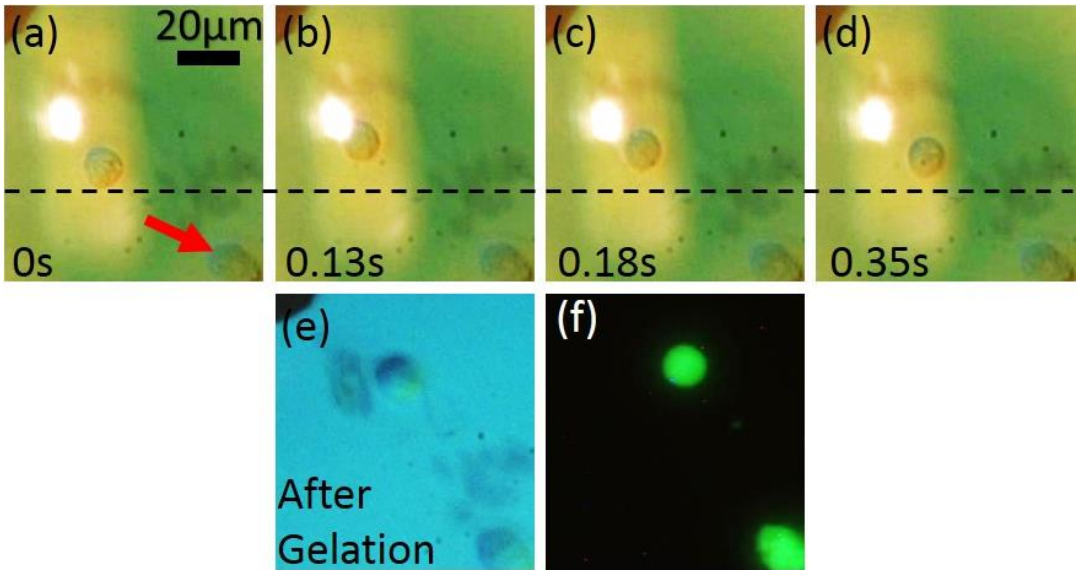

Fig. 3-19 Viability tests on cells after being circulated by OFB single-cell transporter. (a-d) An NIH-3T3 cell circulating. The red arrow marks a nearby cell as a point of reference. The black dashed line is the reference line to detect the position of the cell. (e) An image taken after the cell had been circulated for at least 20 times, followed by PEGDA gelation. (f) Viability test of the same cells in (a-e). Green fluorescence indicates that the cell is viable.

In the cell patterning experiments described in this paper, a distance of at least 10 μm was maintained between the cell edge and the laser spot. This means the cell is outside the high-temperature region near the laser spot, as verified by the temperature-sensitive polymer experiments (Fig. 3-18). The laser pulse frequency was fixed at 100 Hz and

the pulse width was tuned to a value that can finish the transportation in a reasonable time (within 10 minutes). However, the viability tests in Fig. 3-19 and the results in Fig. 3-17 suggest that the cells could be transported at a much faster velocity.

3.5.5 SINGLE-CELL PATTERNING

To test the OFB single-cell transporter, NIH-3T3 cells in cell culture medium were mixed with a hydrogel pre-polymer to form the working media for these experiments. PEGDA and agarose are two hydrogels used in cell patterning [3][37][38]. PEGDA is a photo-curable synthetic polymer, while agarose is naturally derived and is cured by lowering the temperature. Cell patterning using these two hydrogels has usually been done using DEP forces [37][38]. Here, we demonstrate programmable direct-cell patterning in these two hydrogels.

3.5.5.1 SINGLE-CELL PATTERNING IN PEGDA

A two-dimensionsal 4 x 4 cell matrix was constructed in PEGDA using the OFB single-cell transporter. First, a pre-polymer was made of 10% (w/v) PEGDA (MW: 6000, Sigma-Aldrich) and a photoinitiator of consisting of 0.2% 2-Hydroxy-4′-(2-hydroxyethoxy)-2-methylpropiophenone (Sigma-Aldrich). The pre-polymer was mixed in a 1:1 volume ratio with the harvested NIH-3T3 cells in media to yield a working medium containing 5% PEGDA, 0.1% photoinitiator, and 3×10^5 cells/ml. A 50-µl aliquot of this working medium was dispensed onto the substrate. The thickness of the dispensed aliquot on the substrate varied depending on the area of the media droplet. However, the media always had a thickness of greater than 100 µm, which is sufficient to cover the cells under transportation. A thicker media droplet does not have any effects on the micro-transportation.

The entire patterning process for creating the 4 x 4 cell array took 6.5 minutes (Fig. 3-20a-d). The laser pulse frequency was 100 Hz. A laser pulse width of 7 µs was used to transport cells at an average velocity of 30 µm/s to positions 50 µm away from its final position. At this point, the pulse width was reduced to 5 µs, corresponding to an average transport velocity of 5 µm/s, to perform the final positioning of the cells. This reduction in pulse width ensures the accurate positioning of the cells under transportation, while reducing the possibility of disturbing neighboring cells.

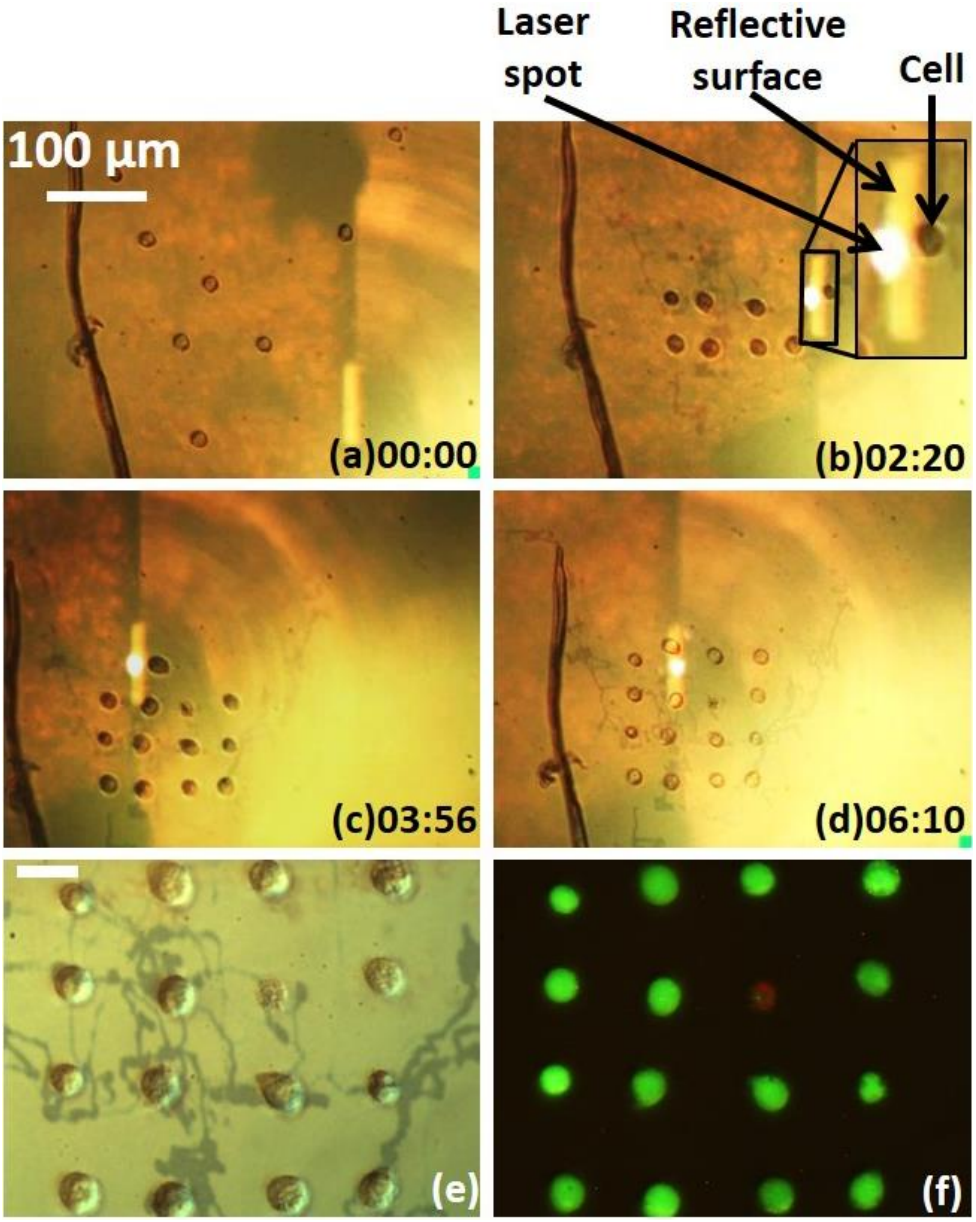

Fig. 3-20 Patterning of a single NIH-3T3 cell in PEGDA by the OFB single-cell transporter. The time stamp format is m : s. (a-d) Cells were assembled by the OFB single-cell transporter. The inset shows a close image of the cell being transported. The reflective surface is the emitting surface of the laser diode, due to the match of the focal plane of the microscope objective lens and laser projection objective lens. (e) Single-cell pattern after PEGDA gelation. The dark tracks may be due to the laser heating of the substrate, but they do not affect the OFB transportation. The scale bar is 20 µm, and also applies to (f). (f) Viability test on the assembled cells. Green fluorescence indicates that the cell is viable, while red fluorescence indicates a non-viable cell.

After the cells were assembled, the media within the field-of-view of the microscope was exposed to a broadband UV source (90 mW/cm^2 at 365 nm, X-Cite Series 120Q) for 15 seconds to photopolymerize the PEGDA. Uncured excess PEGDA pre-polymer was washed away by pipetting phosphate-buffered saline (PBS) solution directly onto the chip. The overall PEGDA gel area was about 30 mm^2. The final cell pattern in the polymerized PEGDA is shown in Fig. 3-20e.

The transport velocities of the cells were slower than those predicted from Fig. 3-17. This is due to the separation that was maintained between the cells and the generated bubble to avoid exposing the cells to a high temperature, as mentioned in Section 3.5.4.

3.5.5.2 CELL PATTERNING IN AGAROSE

Agarose is a natural material, and is degradable by cellular enzymes, making it attractive as a cell scaffold [37]. However, the transportation of cells directly in agarose is more challenging due to the higher viscosity of agarose solutions. Here, single cells were directly transported inside agarose in solution, and assembled into a pattern, followed by the gelation of the agarose. This experiment demonstrates the feasibility of using the OFB to seed 3D cultures in agarose.

Agarose gelation is triggered by lowering the solution temperature. Thus, a cooling system has to be added to the Fig. 3-10 to enable the gelation. Two schemes were used to realize this. Fig. 3-21 shows the first scheme, in which a Peltier chip (Tellurex C134-1604) was used to cool the substrate. The Peltier device was clamped on the substrate alongside the reservoir, and is used to manage the temperature of the liquid in the reservoir. It can heat the fluid in the reservoir to 32 °C, or to cool the fluid in the reservoir to 14 °C. There is a temperature difference of approximately 1 °C in the reservoir on the side closer to the Peltier device compared to the side farther away. This small temperature difference does not affect the experiments described here. Fig. 3-22 shows the second scheme of the substrate used for cell transportation inside agarose pre-polymer solutions. Laser absorption in the lower glass slide was found to be negligible. After the cell transportation was completed, an ice cube was placed on one side of the cooling chamber. The icy water melt from the ice cube filled the cooling chamber due to capillary force. Filter paper was placed at the other side of the cooling chamber to absorb the icy water. This method creates a continuous flow of icy water

through the cooling chamber, which drops the surface temperature of the substrate to 11 ºC, with an ambient room temperature of 22 ºC. The lower temperature causes the agarose to gel.

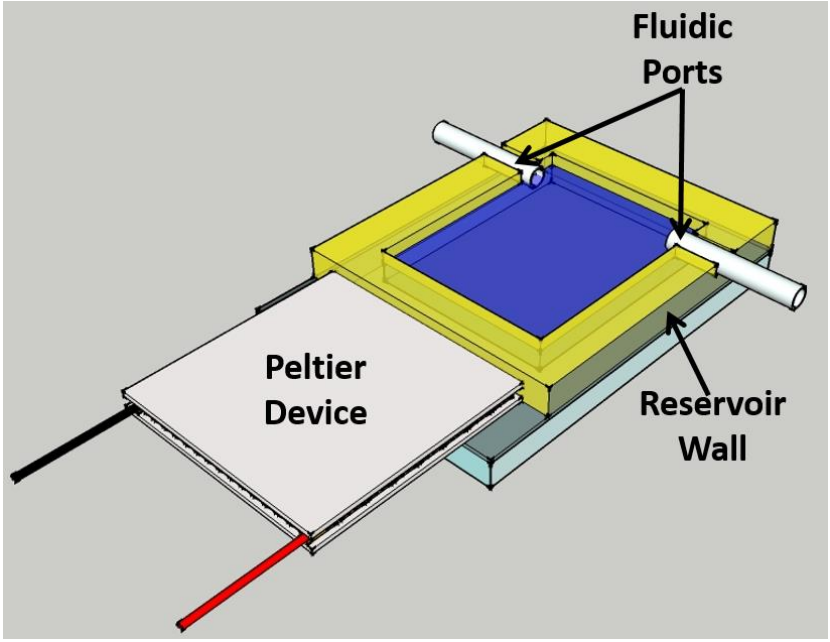

Fig. 3-21 The Peltier chip cooling scheme for the OFB single-cell transporter in agarose

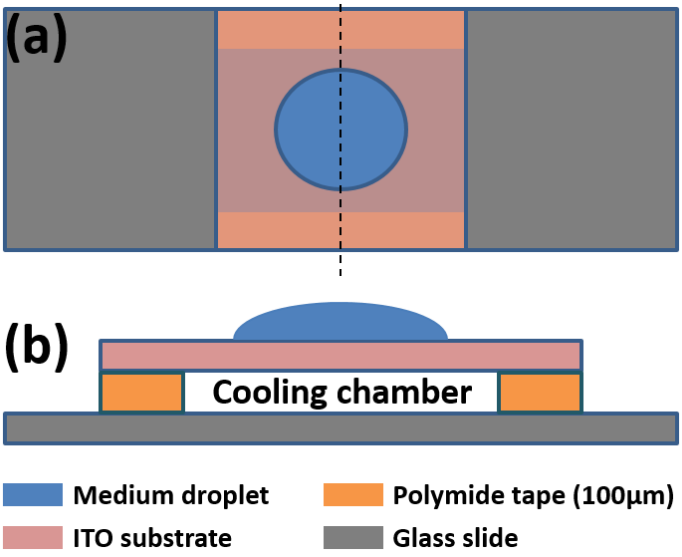

Fig. 3-22 The icy water cooling scheme for the OFB single-cell transporter in agarose. (a) Top view. (b) Cross section along the black dashed line in (a).

Cell patterning was first demonstrated by arranging yeasts into an "H" (for Hawaii) in 1.5% ultra-low-gelling-temperature agarose solution (Fig. 3-23). Yeast was chosen in order to have rapid cell division. The yeasts were collected within a 200-μm-radius circular area. A laser pulse frequency of 60 Hz was used throughout the manipulation (Fig. 3-23a-c). The laser pulse width was set to 60 μs for transporting cells to the assembly sites, and 20 μs for fine adjustments of cell positions. The final pattern contains 12 yeasts. The average yeast diameter is 8 μm and the average distance between each pair of yeast after assembly is 43 μm.

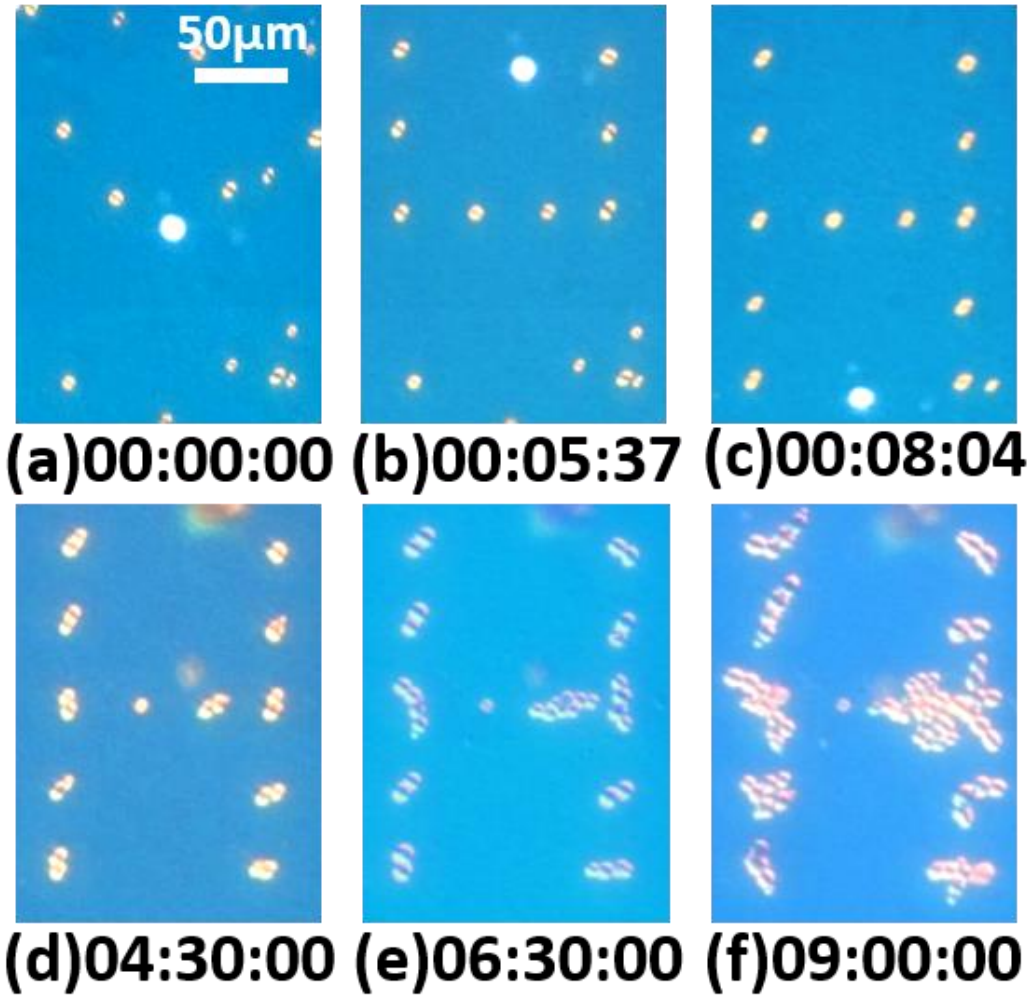

Fig. 3-23 Patterning and culturing of yeasts in 1.5% agarose solution by the OFB single-cell transporter. (a-c) Patterning of yeasts into an "H" in agarose solution, (d-f) Gelation of agarose and culturing for 9 hours. The solution was maintained at 15°C during gelation and at 32 °C at all other times.

After the cell patterning was completed (Fig. 3-23c), the agarose was gelled (Fig. 3-23d) by lowering the temperature of the fluidic chamber to 15 ºC for 10 minutes by the Peltier device (Fig. 3-21). This ensures that the assembled yeasts remain in place, and the agarose hydrogel acts as a scaffold for 3D cell growth. Following agarose gelation, yeast peptone dextrose solution was added to the chamber through fluidic ports, and the chamber temperature was raised to 32 ºC for yeast culturing. Of the 12 cells in the initial pattern, 11 underwent multiple cell divisions. The average single yeast manipulation velocities are 10 μm/s and 4 μm/s for the 60 μs and 20 μs laser pulse widths, respectively. This relatively low velocity can be improved in the future. Currently, the assembly process is controlled manually, and the current manipulation speed gives the operator enough time to ensure that the yeasts remain a distance from the laser spot. Future autonomous manipulation will be able to maintain this separation with a faster reaction time, so the manipulation velocity can be increased.

When patterning NIH-3T3 cells, a solution of 4% (w/v) agarose (Type IX, ultra-low gelling temperature, Sigma-Aldrich) in PBS was made prior to the experiment. This agarose solution was mixed with media containing NIH-3T3 cells at a ratio of 1:3, yielding a solution of 1% agarose (viscosity: 7 cp) [38] with a cell concentration of 4.5×10^5 cells/ml. A 50-μl aliquot of the mixture was dispensed onto the ITO substrate. It took less than 6.5 minutes to assemble nine cells into a 3 by 3 matrix (Fig. 3-24a-d). The laser pulse width was set 10 μs during cell transportation. Tuning the pulse width to a smaller value for the fine adjustment of the cell positions was not necessary in this experiment. The more viscous agarose medium reduces the scale of the thermocapillary flow (Fig. 3-11c), so higher precision was possible. The decreased flow velocity also reduced the average cell transportation velocity to approximately 8 μm/s.

After the cell pattern is formed, an ice cube was put on one side of the cooling chamber Fig. 3-22, and filter paper was placed at the other side of the chamber to collect the icy melt-water. This lowered the substrate surface temperature down to 11 ºC, in an ambient room temperature of 22 ºC. The substrate was kept cool for 10 minutes, resulting in an agarose gel approximately 75 mm^2 in diameter. The substrate was then separated from the cooling chamber and placed into a sterilized 35 mm × 10 mm tissue culture dish. A 2% agarose (low-melting point agarose, Promega) was poured into the dish to fix the whole chip. The total thickness of the agarose was about 5 mm deep.

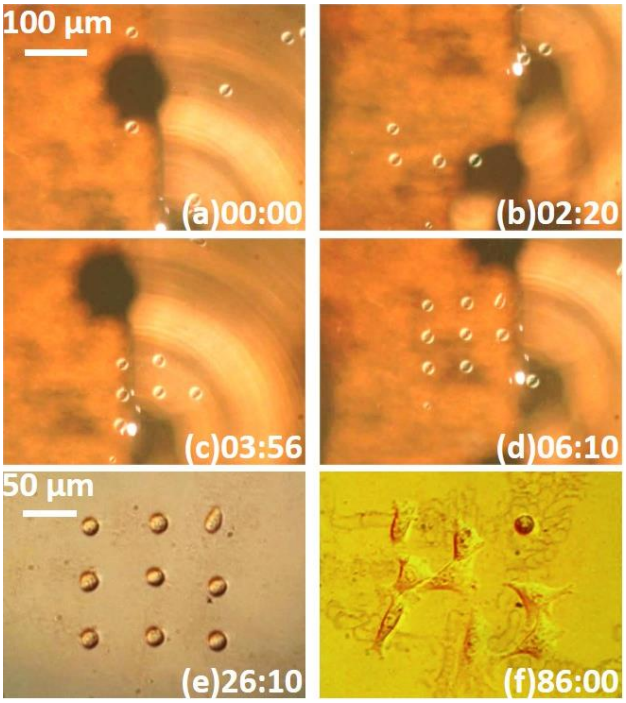

Fig. 3-24 Patterning 3T3 cells in 1% agarose by the OFB single-cell transporter. The time stamp format is minutes : seconds. (a-d) Patterning of cells. (e) Single-cell pattern after agarose gelation. (f) Cells after one hour of culturing. The patterns visible underneath the cells are due to the laser heating of the agarose. This does not affect the transportation. These patterns are also present in (e), but are more obvious in (f), due to imaging with differential-interference-contrast (DIC) microscopy.

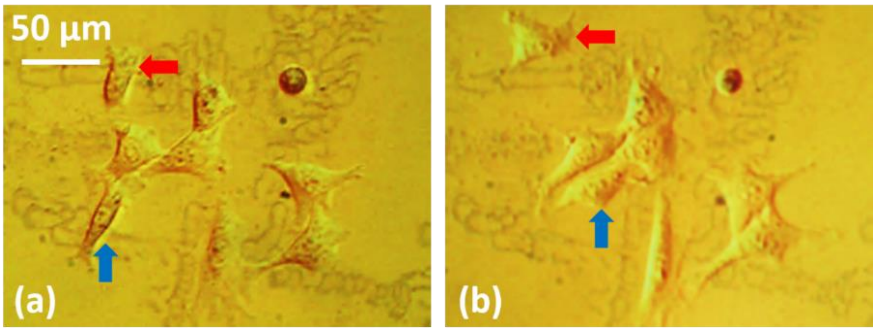

Fig. 3-25 Cell migration under agarose hydrogel after being patterned by the OFB single-cell transporter , after (a) one hour and (b) two hours of culturing. The cells marked by the red and blue arrows have moved significantly. Note that (a) is the same as the Fig. 3-24.

Fig. 3-24e shows the single cell pattern inside the agarose hydrogel. Cell culture medium was dispensed on top of the agarose gel, and the dish was incubated at 37 ºC

in a 5% CO_2 atmosphere. After one hour, eight of nine assembled cells spread and started migrating beneath the agarose [109][110], as shown in Fig. 3-25. Red and blue arrows mark the two cells with significant migration.

CHAPTER. 4 HYDROGEL MICRO-TRANSPORTER DRIVEN BY OFB (HMDO) IN WATER

4.1 MICRO-TRANSPORTATION BY HMDO

4.1.1 INTRODUCTION

In addition to the non-contact transportation of single cells by OFB, another way to handle cells directly (without a supporting microgel) is to introduce an intermediary structure between the OFB and the cells, like the microtools driven by optical tweezers [32][33][34][59]. In this section, the OFB is used to drive a hydrogel structure made of poly(ethylene glycol) diacrylate (PEGDA) to realize contact transportation. Although microfabricated structure has to be introduced to the working space, this Hydrogel Micro-transporter Driven by OFB (HMDO) inherits all the features of the optically actuated micro-transporter, and complements the non-contact single cell transportation of OFB in Section 3.5.4. The HMDO also benefits from OFB, as the laser focusing is more relaxed; a 20X objective lens with a N.A. of 0.4 is used in this system, , in contrast to the tightly focused laser in microtools driven by optical tweezers (projection lens: 100X, N.A. 1.4) [34]. This simplifies the optical path of the system, and makes the HMDO able to explore a wider region in the fluidic working space, enabling more parallel and cooperative transportation.

To demonstrate the capabilities of HMDO, various micro-objects were assembled, including 20-μm-diameter polystyrene beads and single yeast cells. Cooperative transportation of 20-μm-diameter polystyrene beads by two HMDO was also demonstrated. At last, cell-laden-microgels were gathered and assembled by the HMDO.

4.1.2 EXPERIMENT SETUP

The HMDO system is shown in Fig. 4-1. An infrared laser is focused on the bottom of a fluid reservoir containing the cells to be transported. The light is absorbed by the α-silicon layer, creating a thermocapillary flow that actuates the hydrogel microrobots. A Peltier device helps to manage the temperature of the fluid reservoir.

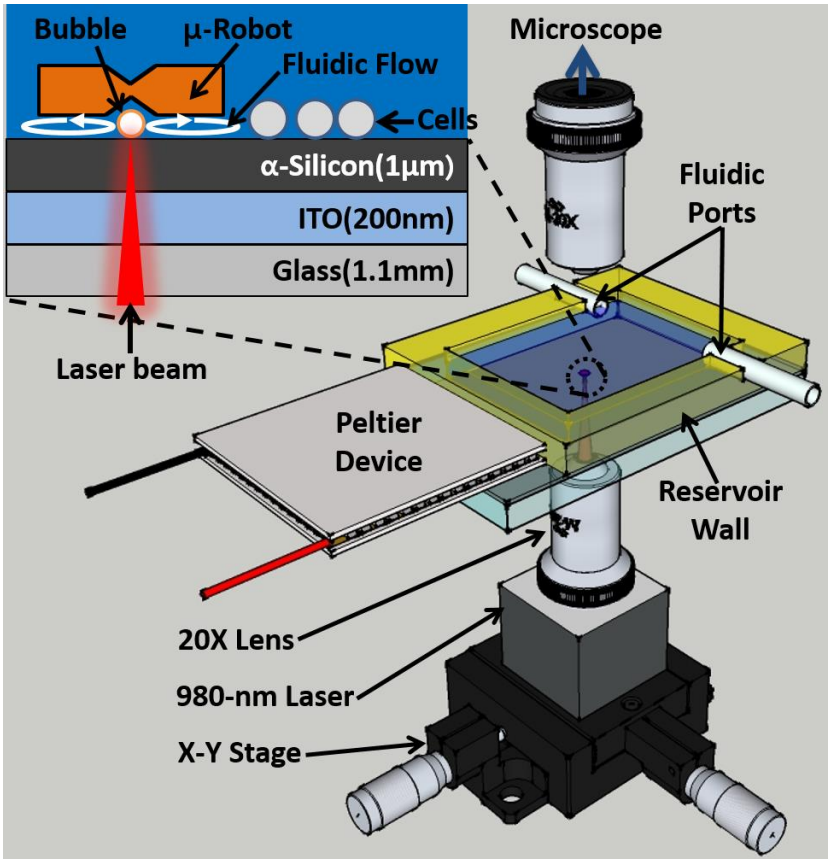

Fig. 4-1 Experimental setup of the Hydrogel Micro-transporter Driven by OFB (HMDO). The inset shows the side view of the HMDO actuation mechanism.

In Fig. 4-2, the hydrogel micro-transporter designs are shown. It is made of PEGDA (Sigma Aldrich, typical Mn: 258) using the same photopolymerization procedure described in detail in the Section 3.3.3. The hydrogel micro-transporter has a disk shape with cavities at the center on both the upper and lower surfaces (No. 1 in Fig. 4-2a). The micro-transporters used here have diameters D = 80 to 140 μm, and a thickness of t = 50 μm. The concavities in the center of the disk have diameters of d = 10 μm, and an average depth of 9 μm, as measured by an optical profilometer (Wyko NT1100). These cavities provide a place for laser-generated microbubbles to push the micro-transporter structure, and are created during the photopolymerization process. The PowerPoint pattern (Fig. 4-2b) used to create the hydrogel micro-transporter had a dark spot in the centre of the disk. Light refraction in the projection system led to the formation of the concave cavities in the centre of the disk

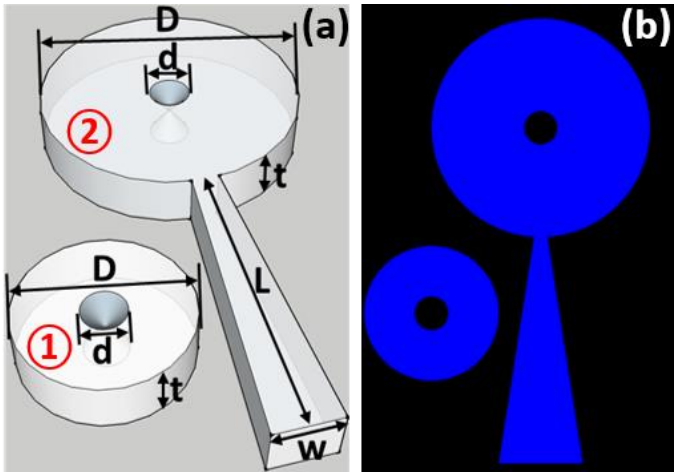

Fig. 4-2 The hydrogel micro-transporter design. (a) The different shapes of the HMDO used in the experiments presented here. Important dimensions are labeled. (b) Optical patterns used for the photopolymerization of the HMDO.

A slightly different micro-transporter structure (No. 2 in Fig. 4-2b) is needed when manipulating objects smaller than 10 μm. During normal HMDO actuation, the hydrogel structure levitates slightly above the substrate (inset of Fig. 4-2a), which allows smaller micro-objects to slip underneath the edge of the hydrogel micro-transporter. The second micro-transporter is designed to prevent this, and features a stub protruding from the main disk portion of the micro-transporter, with a length of L = 135 μm and a width of w = 50 μm. This stub flexes downward slightly, allowing the micro-transporter to maintain contact with the substrate for the transportation of objects less than 10 m in diameter. This contact point also serves as a pivot to orient the micro-transporter. This second type of micro-transporter is also able to transport larger objects as well as smaller objects. However, the extra stub somewhat reduces the HMDO transportation velocity, so the cylindrical micro-transporter (No. 1 in Fig. 4-2b) is preferred if only objects larger than 10 μm are to be transported.

4.1.3 HMDO ACTUATION

4.1.3.1 ACTUATION MECHANISM

The micro-transporter is actuated by OFB generated at its concave portion Fig. 4-1. After the OFB is generated, the vertical flow component near the bubble is directed upwards from the substrate. This upward flow, as well as the size of the bubble itself, results in the levitation of the micro-transporter above the substrate. At the same time,

there is a parallel flow component that is axially symmetric around the focused laser spot, as this is the heated region of the substrate. The parallel thermocapillary flow forces the bubble, and the micro-transporter above the bubble, to center itself over the laser spot. This is a stable state, as the parallel thermocapillary flow components cancel. If the laser spot is moved, the bubble will follow, and thus the laser can move a bubble against the concave portion of the hydrogel structure, actuating the levitated micro-transporter. The hydrogel structure does not contact the substrate, reducing stiction for more robust operation. Once the laser pulse is over, the gas bubble starts to collapse due to the decreasing temperature inside the bubble and the large Laplace pressure. New bubbles can be generated by the next laser pulse to continue the actuation of the micro-transporter.

4.1.3.2 ACTUATION VELOCITY

The size of the OFB and the scale of the surrounding thermocapillary flow are functions of the laser intensity, pulse width, and pulse frequency. These factors determine how fast the HMDO moves, and are characterized in Fig. 4-3. As expected, smaller hydrogel structures can move at higher velocities. In addition, micro-transporter velocity increases as pulse width and pulse frequency increase. These measured velocities represent the maximum rate at which a HMDO can be moved in a single direction for a distance of 750 μm.

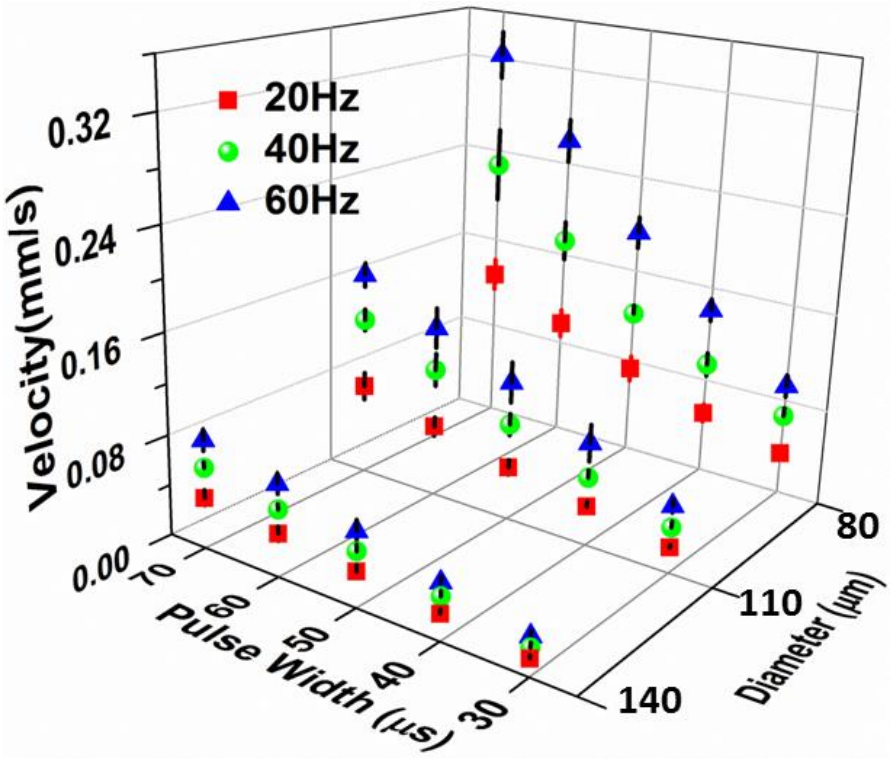

Fig. 4-3 HMDO actuation velocities in terms of the laser pulse frequency, the laser pulse width, and the hydrogel end-effector diameter. Each data point is the average measurement from ten different end-effectors of the same size. Error bars are the standard deviation of the ten measurements.

4.1.4 TEMPERATURE DISTRIBUTION AROUND THE HMDO

The temperature distribution around the micro-transporter was empirically verified by the same method in Section : by observing the laser-induced bubble formation in a solution of deionized water mixed with 10% (w/v) PNIPAAm(Fig. 4-4). For a laser pulse width of 160 μs and a pulse frequency of 20 Hz, PNIPAAm gelation was observed in an area with a diameter of 14.5 μm when ambient temperature was 20 °C. This corresponds to the highest amount of optical energy of all the laser pulses used here for cellular transportation. The diameter of the PNIPAAm gel is much smaller than the minimum diameter (80 μm) of the current micro-transporter. More heat may be retained when a hydrogel micro-transporter is actually present around a laser-induced bubble, due to more limited heat dissipation. However, when the experiment was repeated with a hydrogel micro-transporter present, no gelation was observed outside the region

covered by the hydrogel micro-transporter structure. These PNIPAAm experiments indicate that the micro-transporter keeps cells at a safe temperature by maintaining adequate distance from the heated area on the substrate. Furthermore, the micro-transporter diameter is also significantly larger than the diameter of the laser spot, ensuring that the cells are not irradiated with intense light.

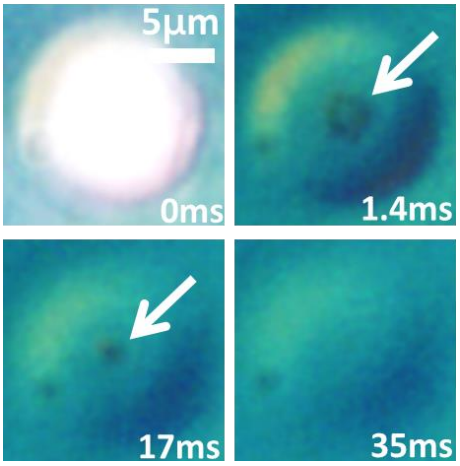

Fig. 4-4 Generation and collapse of the OFB in the 10% PNIPAAm solution in deionized water on ITO substrate coated with 1 µm α-silicon. The laser pulse width is 160 µs at a frequency of 20 Hz. The circular area visible in the last three frames is due to the gelation of PNIPAAm. The bubble marked by the white arrows has a diameter of 3.4 µm immediately after the laser pulse, and it dissolves into the solution within 35 ms. Due to refraction at the surface of the layer of water, the laser spot appears larger than its actual size.

4.1.5 PATTERNING OF POLYSTERENE BEADS

Patterning of 20-µm-diameter polystyrene beads (Polysciences, Inc.) into a densely packed UH shape was done first to study the micro-transportation resolution (Fig. 4-5a). Polystyrene beads in deionized water were added to the open fluid reservoir. To form the UH pattern, a 140-µm-diameter micro-transporter was used to gather randomly distributed beads from within a circular area with a radius of 1.3 mm.

The entire transportation process lasted approximately 17 minutes, and included the transportation of 23 beads. A laser pulse frequency of 20 Hz and a pulse width of 160 µs were used for long-distance bead transportation. The longer laser pulse width helped to increase the micro-transporter actuation velocity, which averaged 75 µm/s. When

the micro-transporter brought the beads close to their final position, the micro-transporter velocity was slowed to achieve higher positioning accuracy. A laser pulse of 80 µs at 20 Hz was used during the short-range, final micro-transportation of the beads into the UH pattern, corresponding to an average micro-transporter velocity of 10 µm/s. When placing a bead at a desired location, no movement of the neighboring beads was observed.

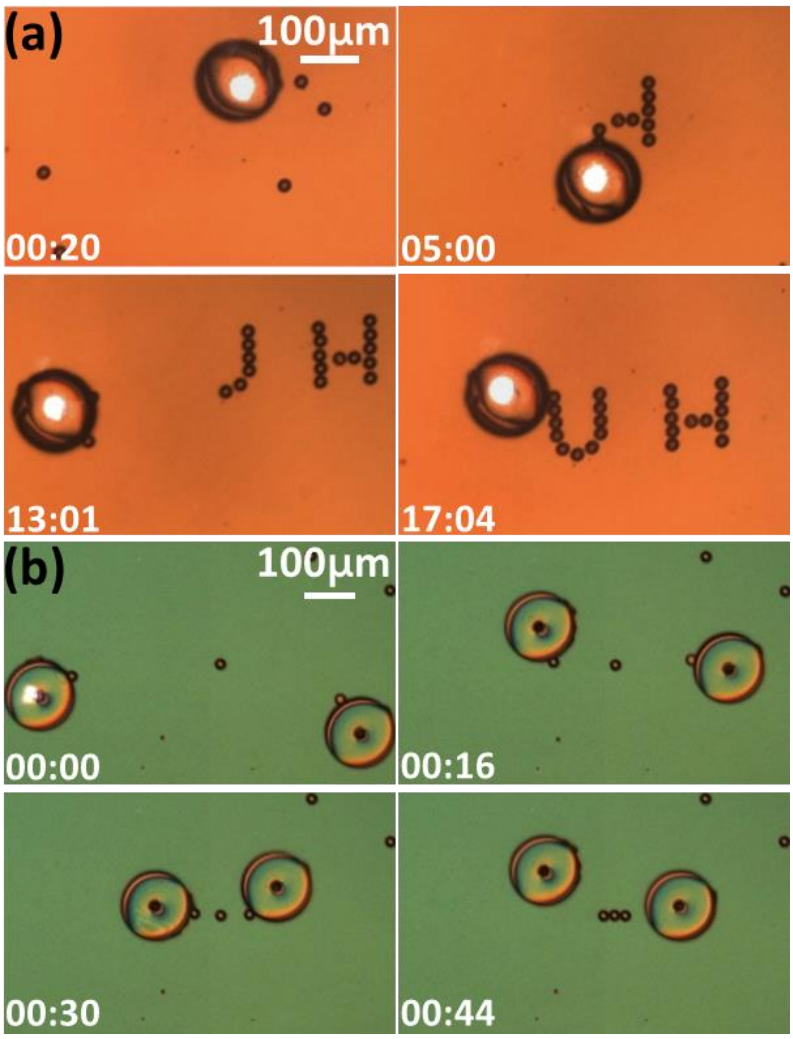

Fig. 4-5 Patterning of 20-µm-diameter polystyrene beads into "UH" using 140-µm-diameter HMDO. The time stamp format is m : s. (a) Transportation of a "UH" pattern using a single end-effector. (b) Cooperative transportation of beads by two HMDOs.

The concept of the cooperative transportation was also demonstrated (Fig. 4-5). Another laser was added to the setup in Fig. 4-1, so that there were two lasers projected

obliquely onto the substrate. Each laser was independently controlled by a separate X-Y stage. Two 20-µm-diameter polystyrene beads were moved in parallel to each side of a bead in the center of the field of view, forming a densely packed line of beads. Laser pulses of 50 s at 40 Hz were used.

4.1.6 PATTERNING OF SINGLE CELLS

The feasibility of using the HMDO system for cell patterning was demonstrated by the patterning of single yeasts (Fig. 4-6). Although it is unnecessary for yeast viability, the transportation was done in phosphate-buffered saline (PBS) to demonstrate that this system can also be used with mammalian cells. Bakers' yeast was chosen for this demonstration, due to its rapid growth rate. The size of yeast cells is also similar to that of many mammalian cells, making yeast a suitable model cell for future use of this system with animal or human cells.

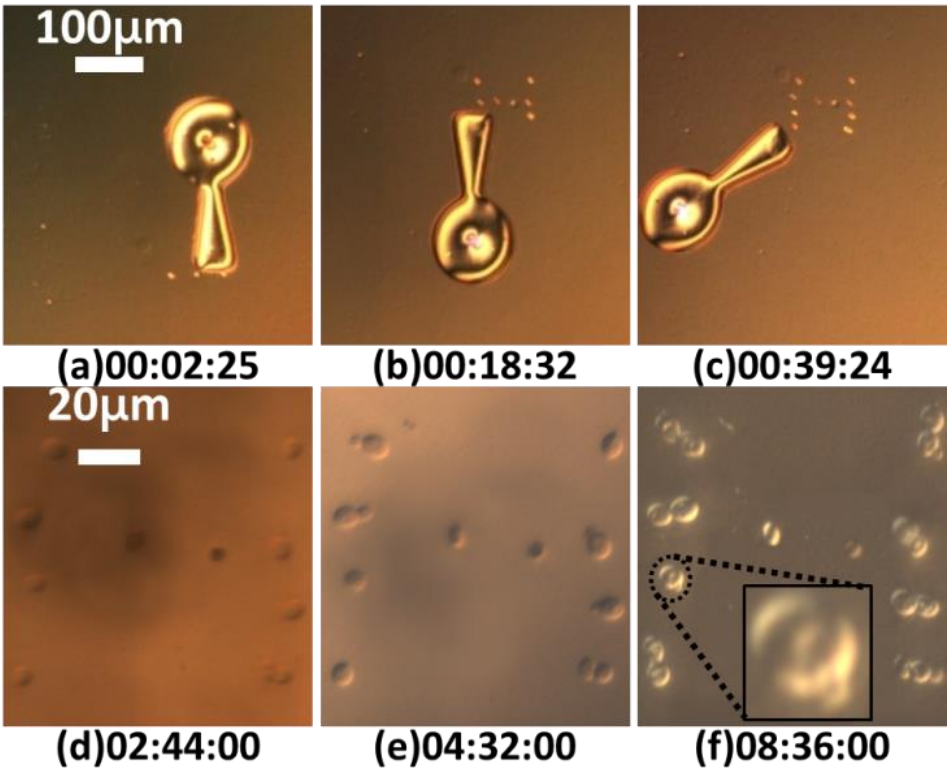

Fig. 4-6 Patterning of single yeast using a HMDO with an additional transportation stub. (a-c) The patterning process. (d-f) Cells during culturing. (e) The yeast began to multiply after four hours. (f) The yeast after culturing for eight hours. Cell division is obvious for seven of the yeast cells. An eighth cell, highlighted in the inset, has a small bud forming. The time stamp format is h : m : s.

The diameter of the micro-transporter used was 130 μm, while the average diameter of the yeasts was 7.3 μm. Due to the small size of the cells, a stub with dimensions of L = 135 μm and w = 50 μm was added to the circular micro-transporter structure to ensure contact between the micro-transporter and the substrate. When the frequency is 20 Hz, keeping the laser pulse width shorter than 200 μs ensures that the stub contacts the substrate and pushes the yeast; thus a pulse width of 160 μs was used for the transportation described here. Randomly positioned yeast cells were gathered within a circular area with a radius of 1 mm. Ten separate cells were assembled into an H shape using a hydrogel micro-transporter. The average transportation time for each cell was about 3 minutes. The average distance between neighboring assembled yeast cells was 27.5 μm. After the micro-transportation was completed, yeast peptone dextrose (YPD) was slowly injected into the fluid reservoir at 0.1ml/h by a syringe pump (KDS Scientific, KDS-210). The temperature of the yeast solution was maintained at 32 ℃ using the Peltier device clamped to the substrate, and the reservoir was covered to prevent evaporation. After approximately eight hours, eight out of the ten original yeast cells showed signs of cell division.

The yeast transportation required more delicacy than the polystyrene beads. Although yeast could be pushed at a maximum rate of 40 μm/s, the lower density of the yeast meant that this maximum velocity could not be maintained, since fluidic disturbances [62] generated at the tip of the stub can push yeast cellss upwards and to the sides of the robots. If the yeast lifted off the substrate, the micro-transporter motion was stopped for more than 30 seconds to let the yeast re-settle onto the substrate. The micro-transporter could then re-align itself to the cell and continue transportation. This adjustment was done multiple times during the transportation, which made the average velocity approximately 5 μm/s. When the yeast was close to its final location, the velocity of the micro-transporter was decreased to prevent disturbance of neighboring yeasts. After a yeast was placed in the desired position, the micro-transporter was left in place for approximately 30 seconds. Immediate retraction of the micro-transporter may cause the yeast to move backwards with the micro-transporter due to the disturbance generated by the robot.

4.1.7 PATTERNING OF CELL-LADEN MICROGELS

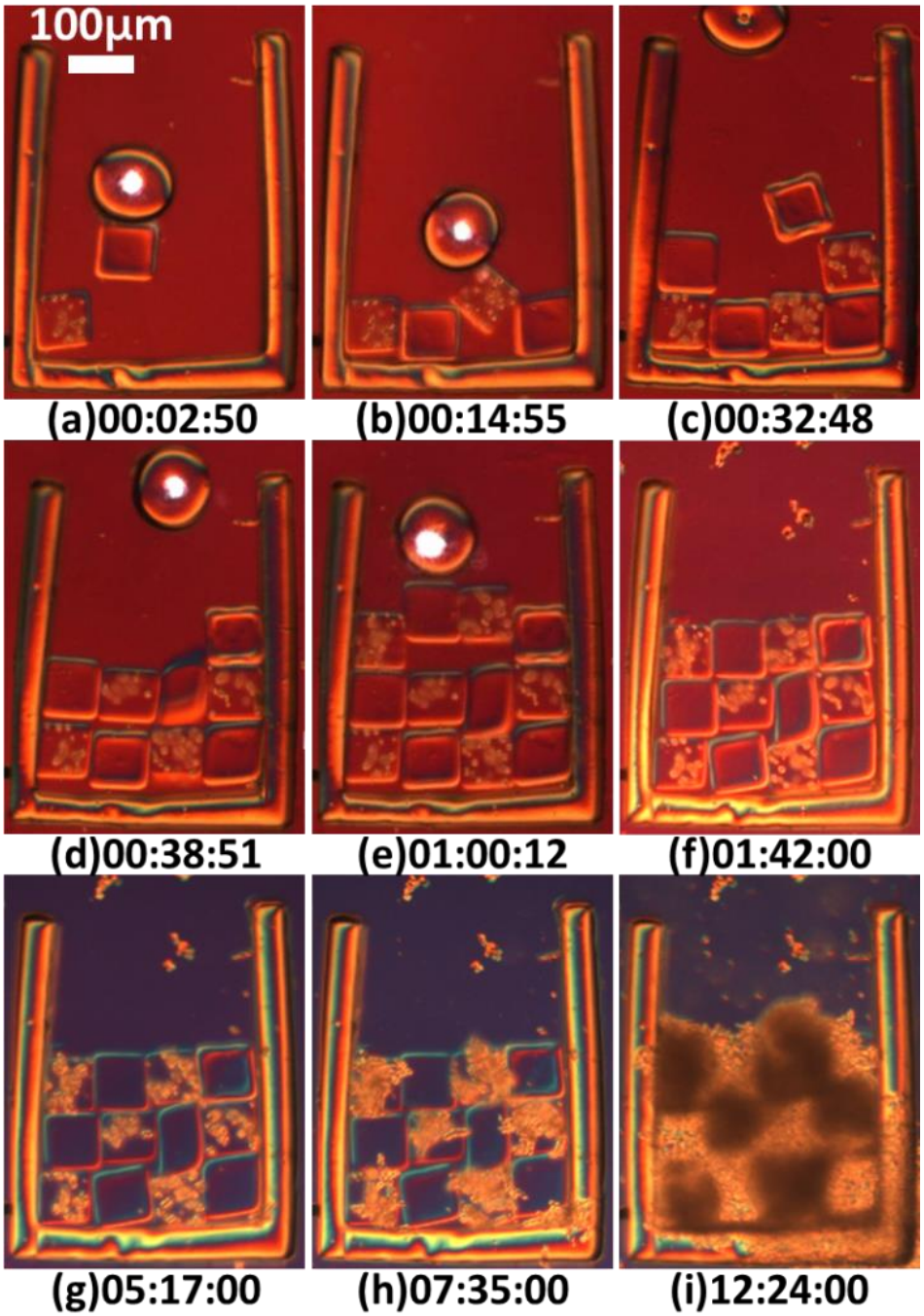

Fig. 4-7 Patterning of 80-µm agarose gel blocks into a 3 × 4 array by a HMDO. A PEGDA frame is used to secure the assembled gel blocks. Half of the blocks contain yeast, visible as small particles within the gel. The other blocks do not initially contain cells. (a-e) The patterning process. (f) The start of the culturing period, after the agarose solution in the reservoir was gelled, and the YPD added. (g-i) Yeast growth. As the cells multiply, the yeast moves into all of the agarose blocks.

Similar agarose microgel blocks as that in Section 3.3.3were assembled. Gel blocks

without yeast (1.5% w/v agarose in PBS) were also made at the same time. These microgels had dimensions of 80 μm × 80 μm × 50 μm. A holding structure was made using the same PEGDA photopolymerization process described earlier. The gel blocks were moved into this holding structure using the HMDO to form a 3 × 4 array of agarose microgel blocks (Fig. 4-7). The blocks were arranged so that the cell-laden blocks alternated with the blocks containing no cells. The average travel distance for these 12 gel blocks to their final positions was 2 mm. Laser pulses of 160 s at 20 Hz were used for the transportation of the gel blocks. The average transportation velocity for the agarose gels without cells was 30 μm/s, or 10 μm/s for the gels containing cells. This relatively low speed is due to friction between the blocks and the substrate, especially for the gel blocks containing yeast.

The overall transportation took about one hour. This transportation time can be greatly reduced with further improvements to this process. When the gel blocks were released from the PDMS mold, many broken pieces of gel blocks and single yeast also entered the fluid reservoir. This made it necessary to hunt for intact gel blocks among the debris. In addition, the HMDO was used to sweep the debris from a path between a gel block and the holding structure before transporting the block. This cleaning step was necessary to avoid having the gel blocks stick to debris lodged on the substrate, but also added time to the process. Filtration of the gel blocks before adding them into the fluid chamber should help with these issues, and reduce the overall transportation time. The final positioning of the gel blocks once they crossed the opening of the holding structure was only 15 minutes in total; most of the transportation time was used by the search for suitable gel blocks and the transportation of those blocks to the holding structure. In addition, fitting the last block in each row into position requires more precise transportation, and thus takes more time (Fig. 4-7b). For example, it only took 17 seconds to position the first block on the right in the bottom row of the block array, starting from when the block is moved into the opening of the holding structure. In contrast, it took 236 seconds to position the last block in the bottom row, the second block from the right in Fig. 4-7b. This transportation time can also be reduced in the future by using a different shape for either the holding structure or the agarose blocks. During the transportation process, the Peltier device was used to heat the substrate to 32 °C. After the transportation, the PBS solution in the fluid reservoir was replaced with 1.5% w/v agarose solution. The substrate was then cooled to 14 °C, gelling the

agarose solution in the reservoir, which helped hold the assembled hydrogel blocks in place. This cooling process lasted for ten minutes, then the substrate was heated to 32°C once again. At this point, the fluid reservoir was supplied with YPD with 1% v/v antibiotics (Penicillin-streptomycin, Invitrogen, Inc). The yeast-cell-laden blocks were incubated at 32 °C on the microscope stage (Fig. 4-7f). The yeast multiplied in the 3D agarose blocks. After about six hours, the yeasts occupied all the space in their original gel blocks, and began to spread to the neighboring blocks (Fig. 4-7h). After 11 hours, the yeasts underwent enough cell divisions to spread throughout the whole agarose block array (Fig. 4-7i). The multiplying yeast now occupied the previously cell-free gel blocks as well. Other cell patterns can be formed by simply rearranging these gel blocks. Moreover, gels using different materials [101], cell types, and shapes [111] may be used to yield other cell patterns for a variety of applications. Chemicals can also be enclosed in the gel blocks [112] and integrated into the gel block array, which can facilitate better control of the chemical environment for controlled cell growth.

4.2 MICRO-TRANSPORTATION BY ABSORBING HMDO (A-HMDO)

4.2.1 INTRODUCTION

The requirement of a light-absorbing substrate for hydrogel micro-transporter actuation poses some limitations on the application of HMDO. For example, typical cell-culture flasks are made of clear polystyrene and do not absorb light. Addressing this issue requires a micro-transportation tool less dependent on the substrate. With this goal in mind, an Absorbing Hydrogel Micro-transporter Driven by OFB (A-HMDO) was developed. Instead of using a light-absorbing substrate, the hydrogel micro-transporter itself absorbs light and converts it into heat, with OFB generated on its surface. This A-HMDO expands the applicability of OFB in biomedical research. Preliminary micro-transportation results of microbeads (Section 4.2.4), cells (Section 4.2.6) and microgels (Section 4.2.7) on a standard glass microscope slide are shown.

4.2.2 EXPERIMENT SETUP

The setup of the A-HMDO system is shown in

Fig. 4-8. A standard glass microscope slide (75 mm × 25 mm × 1 mm) is placed on the specimen stage under an Olympus BXFM upright microscope. A 980-nm infrared laser

(Laserlands, 980MD-0.8W-BL) is mounted on an XYZ stage positioned below the microscope stage. The on-off states of the laser can be switched by a TTL signal from a function generator. The laser is focused by a 5X objective lens (Newport, N.A.: 0.1) into a circular spot with a full-width at half-maximum (FWHM) diameter of 17.6 μm. When the laser was on, the measured average intensity at the focal point is 72 kW/cm^2.

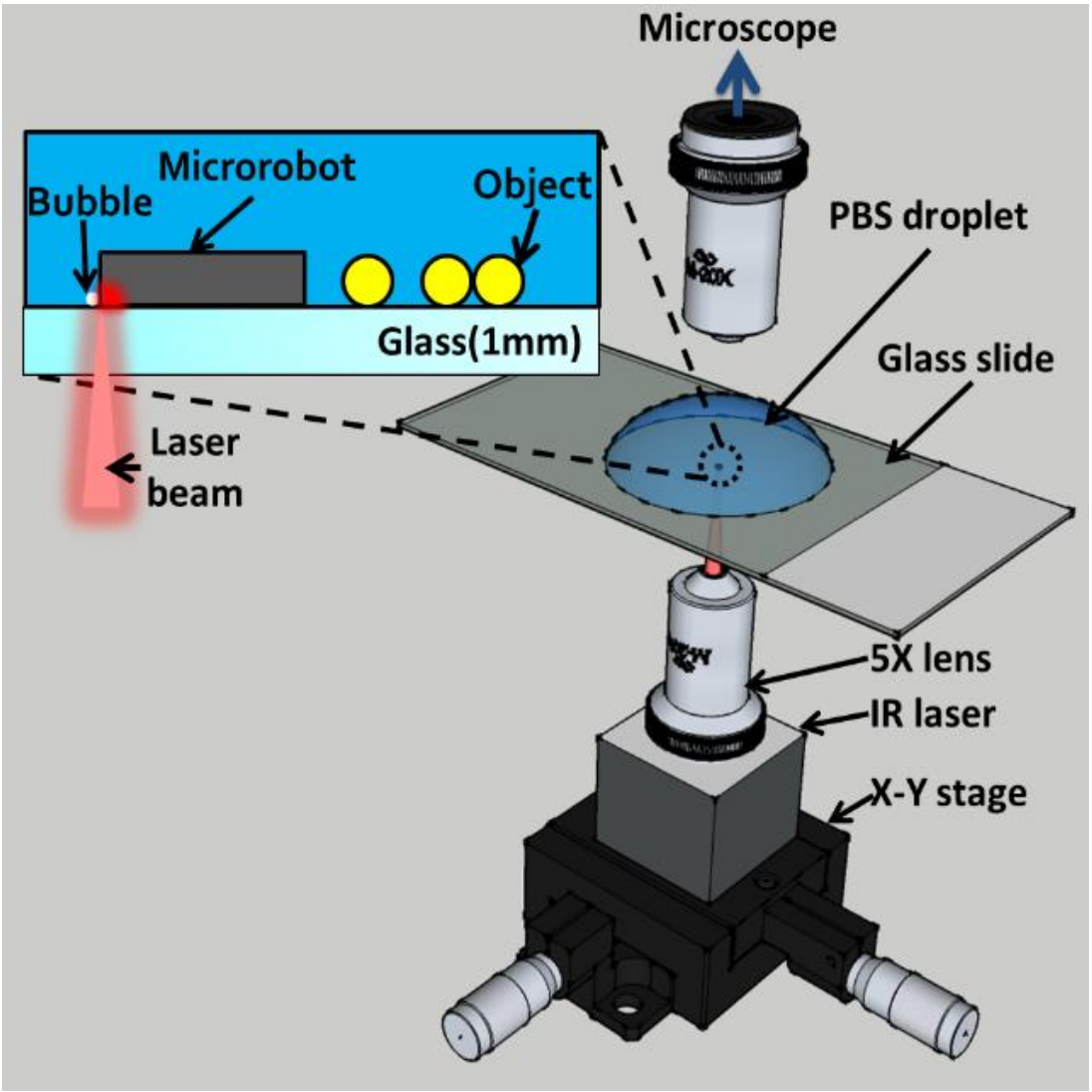

Fig. 4-8 Experimental setup of the Absorbing Hydrogel End-effector Driven by OFB (A-HMDO). The inset shows the side view of the micro-transporter. The 980-nm infrared diode laser was focused on the edges of the absorbing micro-transporter to create bubbles and thermocapillary flow along the bubble surface, actuating the micro-transporters.

4.2.3 A-HMDO ACTUATION

4.2.3.1 ACTUATION MECHANISM

The A-HMDO used in the experiments presented here was made of a T-shaped ink-dyed PEGDA hydrogel, approximately 20 µm in thickness. It was created using the photopolymerization procedure described in Section 4.1.2. The prepolymer consists of a mixture of two parts PEGDA (Sigma Aldrich, typical M_n: 575) with 1% Irgacure 819 photoinitiator (Ciba Specialty Chemicals Inc.), and one part pigmented ink (Higgins Black India ink). India ink is biocompatible [113] and contains carbon black nanoparticles that absorb light. The geometry of the A-HMDO can be divided into two rectangular sections, "A" and "B" (Fig. 4-9). Two types of A-HMDO were tested. The dimensions of each are: Type 1, $W_A = 75$ µm, $L_A = 200$ µm, $W_B = 75$ µm, $L_B = 150$ µm; Type 2, $W_A = 30$ µm, $L_A = 115$ µm, $W_B = 45$ µm, $L_B = 80$ µm. The larger Type 1 A-HMDO is designed for the transportation of objects larger than 10 µm while the Type 2 A-HMDO is intended for the transportation of smaller objects such as yeast.

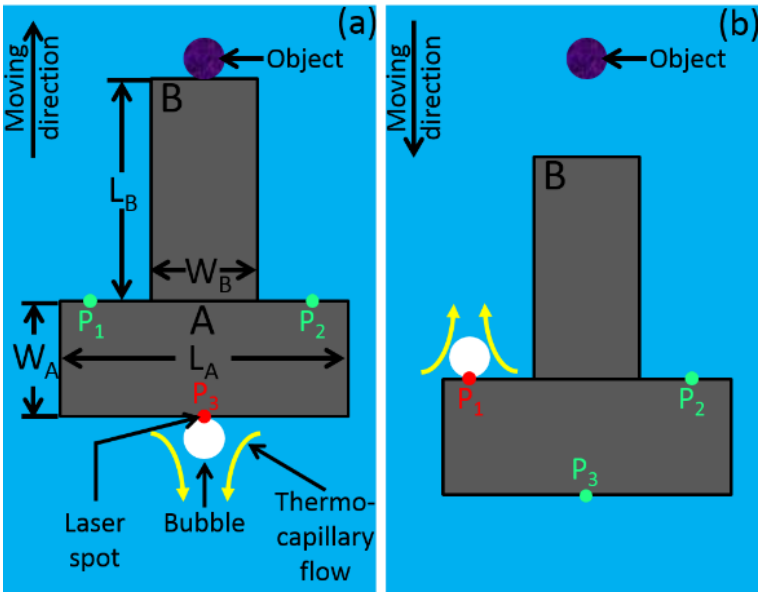

Fig. 4-9 The top view and actuation mechanism of A-HMDO. P_1, P_2 and P_3 are possible laser stimulation points for driving the A-HMDO forward and backward. The point activated by the laser is marked in red. The thermocapillary flow is indicated by the yellow arrows. (a) Laser stimulations at P_3 move the micro-transporter forward (towards the top of the drawing). (b) Laser stimulations that alternates between at P_1 and P_2 move the micro-transporter backward (towards the bottom of the drawing).

To move the A-HMDO forward (towards the top of Fig. 4-9), the laser is focused on the bottom edge of bar "A" (P3 in Fig. 4-9a). The laser-induced heating creates cavitation bubbles at the edge of the micro-transporter structure. The surface of the generated bubble is hotter at the side closest to the edge of bar "A", and is cooler on the side farthest from bar "A". This temperature gradient around the gas/liquid interface drives a thermocapillary flow and pushes the bubble towards the hotter side, which is against the edge of the A-HMDO. Maintaining the focal point at the micro-transporter edge maintains the thermocapillary flow, driving the micro-transporter forward. It should be noted that this mechanism is fundamentally different from the bubble thrust reported in ref. [114]. The orientation of the micro-transporter can be changed by stimulating different areas along the perimeter of the A-HMDO, enabling steering and other functions. The laser can also stimulate the top edge of the bar "A" to move the A-HMDO backwards and away from the object (P1 in Fig. 4-9b). However, continuous stimulation at P1 can cause the A-HMDO rotate counterclockwise. This rotation is prevented by alternating the stimulation between P1 and another point on bar "A" (P2 in Fig. 4-9b).

4.2.3.2 ACTUATION VELOCITY

Two-dimensional A-HMDO motion was demonstrated by moving a Type 1 A-HMDO around a 20-μm-diameter polystyrene bead (Fig. 4-10a). Light diffraction in the photopolymerization system rounded the edges of this particular micro-transporter. The A-HMDO was in a 500-μl droplet of PBS on a glass microscope slide. A 200-Hz pulse train was sent to the laser control circuit to switch the laser on and off. The frame rate of the microscope camera was set to 201 Hz. This made the laser appear on the camera at a frequency of 1 Hz, enabling observation of the laser spot and the optically induced cavitation bubble. With a 250 μs laser pulse width, the micro-transporter finished moving along the circular path in 19 seconds, at an average velocity of 150 μm/s.

The optically induced cavitation bubbles can be observed during the micro-transporter actuation (Fig. 4-10b). Note that, except for the first frame, the laser is not visible, due to the discrepancy between the microscope camera frame rate and the frequency of the control signal. Since PEGDA is hydrophilic, the bubbles detached from the A-HMDO surface between laser pulses, when there was no thermocapillary flow pushing the bubbles against the micro-transporter. The bubbles were then circulated away by the

thermocapillary flow affiliated with the next newly generated bubble (seen in the 70 ms and 130 ms frames in Fig. 4-10b), and dissolved into the medium due to Laplace pressure.

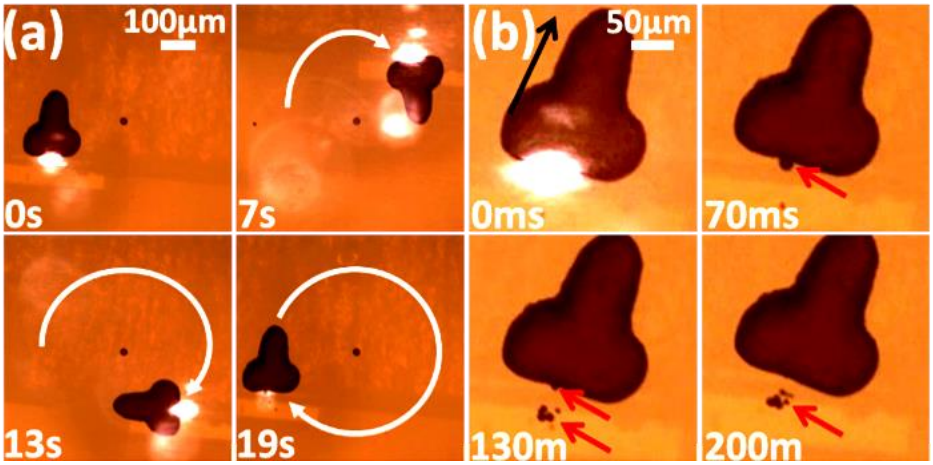

Fig. 4-10 Basic actuation of A-HMDO. (a) Actuation of the A-HMDO relative to a 20-µm-diameter polystyrene bead in the center of the field of view. The movement path is marked by the white arrows. (b) A closer view of the A-HMDO actuation, taken from video frames immediately after the first frame in (a), showing the cavitation bubble created by the laser that enables the thermocapillary flow. The direction of the end-effector movement is marked by a black arrow. The cavitation bubbles are marked by red arrows.

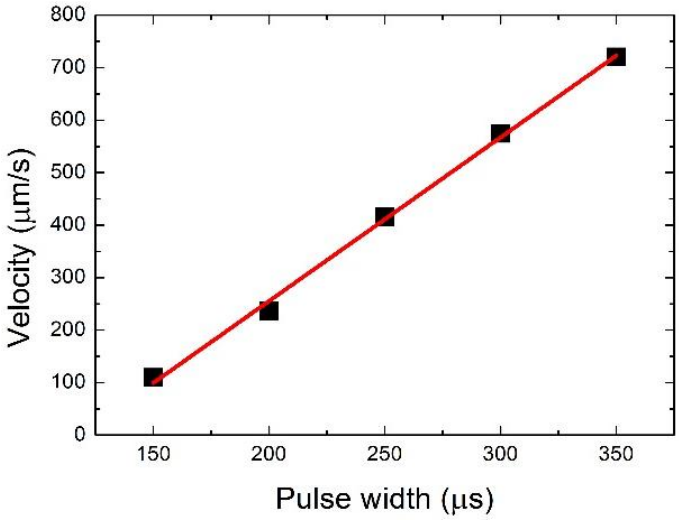

Fig. 4-11 Actuation velocity of a Type 1 A-HMDO in term of the laser pulse width. A red linear trend line was added.

By tuning the pulse width, the duration of the thermocapillary flow in each period of the control signal can be adjusted. As the pulse width is increased, so is the micro-transporter actuation velocity (Fig. 4-11). Thus, if a fine adjustment of the micro-transporter orientation is necessary, the pulse width can be lowered, allowing more precision.

4.2.4 PATTERNING OF POLYSTERENE BEADS

To demonstrate the resolution of the A-HMDO micro-transportation, ten 20-μm-diameter polystyrene beads were assembled into a densely packed "H" pattern, for "Hawaii" Fig. 4-12). The Type 1 A-HMDO was used for this micro-transportation procedure. The pulse width was 350 μs and the entire transportation process took about half an hour.

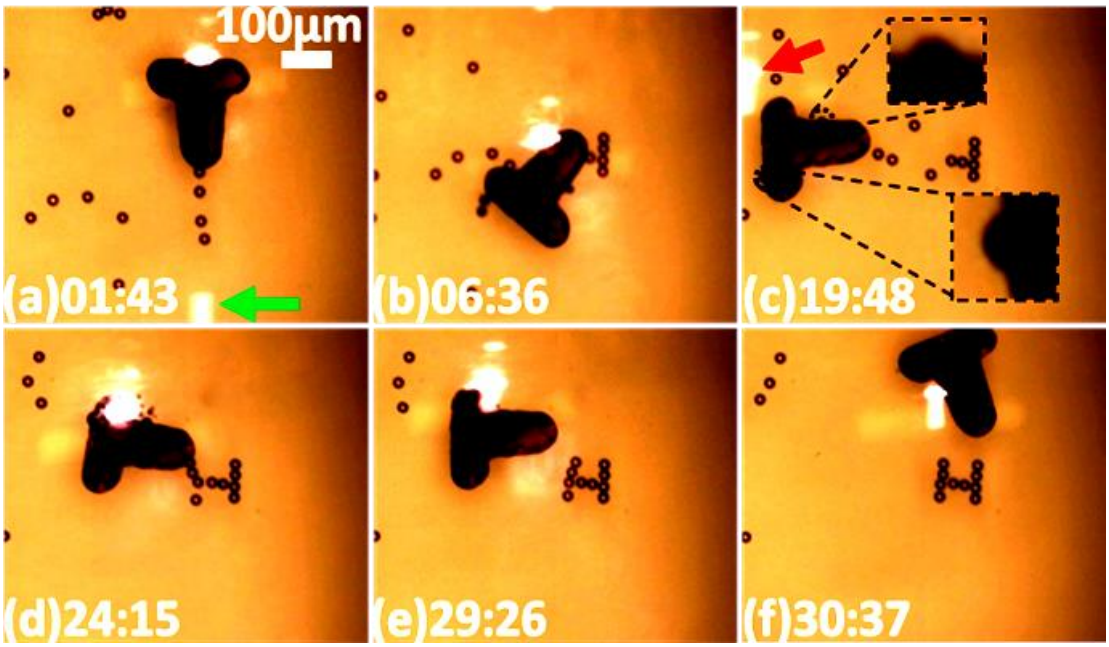

Fig. 4-12 Patterning of 20-μm-diameter polystyrene beads into "H" shape by A-HMDO. The time stamp format is m : s. (a, b) Transportation of the right half of the "H" pattern. The rectangular-shaped light bar marked by the green arrow is an artifact due to the difference between the laser pulse train frequency and the camera capture frame rate. (c-d) Transportation of the left half of the "H" pattern. The laser spot position is marked by a red arrow in (c). The inset shows the bubble trapped at the bottom of the micro-transporter. (e-f) Fine adjustment of the assembled beads

It took less than seven minutes to assemble the first five beads (Fig. 4-12b). However, it took another ten minutes to place the next two beads in the desired location (Fig. 4-12c). This is due to the rounded tip of this micro-transporter (bar "B"). A significant amount of time was consumed as the orientation of the A-HMDO was constantly adjusted to maintain the beads at the center of the tip while moving the micro-transporter in the desired direction. The transportation velocity when pushing a single bead in straight line was up to 44 μm/s. This velocity is slower than the movement of the A-HMDO by itself, partly due to this reorientation issue. The actuation of the A-HMDO was also slowed by the accidental generation of bubbles underneath the A-HMDO. The insets in Fig. 5c highlight two bubbles that were generated underneath the A-HMDO. A bubble created underneath the A-HMDO may lift the micro-transporter off the substrate, making it difficult to maintain the laser focus at the edge of the micro-transporter. If a bubble is created below the micro-transporter, actuation may be temporarily interrupted. The transportation can recover, as long as enough time has elapsed for the bubbles to dissolve into the medium.

The transportation of the "H" was nearly complete after 25 minutes (Fig. 4-12d). Another five minutes was used to pack the beads in a denser arrangement (Fig. 4-12e, f). During this process, the pulse width was decreased to 200 μs to achieve more precise control of the A-HMDO.

4.2.5 TEMPERATURE DISTRIBUTION AROUND THE A-HMDO

To ensure that cells under manipulation are below their maximum physiological temperature (usually 37 °C), the temperature around the A-HMDO during manipulation was sensed using a 5 wt.-% solution of thermoresponsive polymer PNIPAAm (Fig. 4-13) as described in Section 3.5.4. The ambient temperature for this experiment was 20 °C. A laser pulse width of 400 μs was used for this measurement, which is larger than the longest pulse width (350 μs) used in the assembly experiments. The A-HMDO was actuated with the laser as shown in Fig. 4-10b, as this is normally the closest that the laser is positioned to the cells under manipulation. As shown in Fig. 4-13, the PNIPAAm gel was only visible in the region the immediate vicinity of the laser focal point. The PNIPAAm solution did not gel in the other areas around the micro-transporter. Thus, temperature at the tip of bar "B", where the cells contact the micro-transporter, is less than 32 °C. Furthermore, since the viscosity of the PBS is lower than

the PNIPAAm solution, convective heat transfer in PBS should be more rapid, more efficiently cooling the areas around the micro-transporter [115]. We conclude from these PNIPAAm experiments that the temperature around the absorbing hydrogel micro-transporter is safe for the manipulation of living cells.

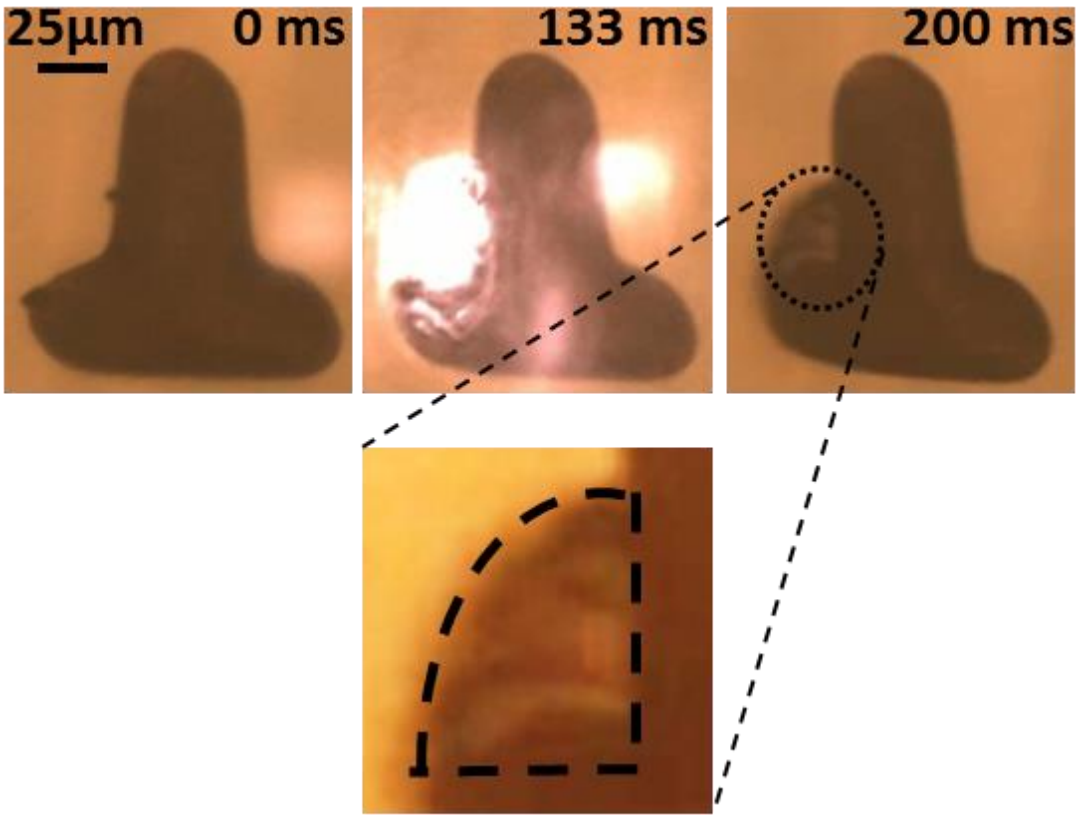

Fig. 4-13 Temperature distribution around the A-HMDO during the actuation. The medium is 5 wt.-% PNIPAAm solution. The laser was turned on at 0 ms. The gelled region visible at 200 ms is outlined in the inset. The gelation process of PNIPAAm distorted the end-effector, but the original geometry of the end-effector was restored after the gel dissipates when the laser heating is over.

4.2.6 PATTERNING OF SINGLE CELL

The A-HMDO has potential as a tool for single-cell transportation. To demonstrate this ability, bakers' yeast was used as a model cell. Three yeasts with an average diameter of 8 µm were aligned by a Type 2 A-HMDO into a straight line (Fig. 4-14).

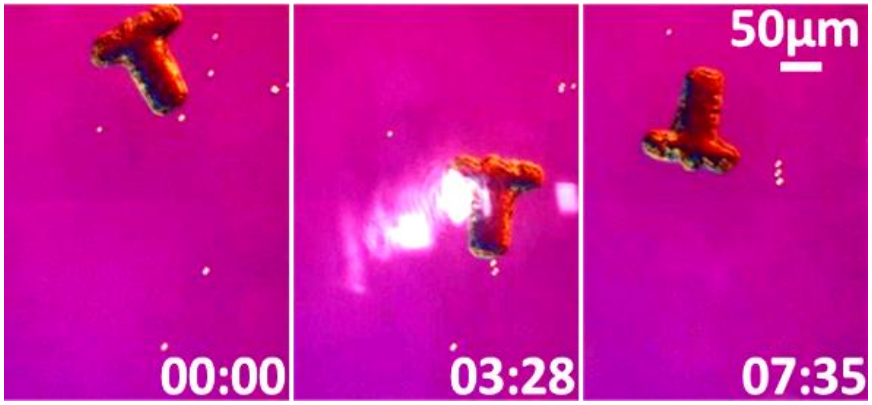

Fig. 4-14 Patterning of single yeast by an A-HMDO. Yeast cells are seen as white dots in the frames. The time stamp format is m : s.

The ambient temperature for this experiment was 20 °C. The transportation took approximately seven and a half minutes, and the peak transportation velocity for pushing the yeast in straight line was 18 µm/s. This was due to the same issues mentioned in regards to manipulating the polystyrene beads. In addition, the positions of the cells were also disturbed by the fluid flows around the A-HMDO during movement [62]. To avoid this, the A-HMDO had to move slowly when it was in close proximity to the assembled cells. This was especially important during the final positioning of cells. After putting a cell into its final location, the A-HMDO actuation was paused for 10 to 20 seconds to allow the cell settle down on the substrate.

4.2.7 COOPERATIVE PATTERNING OF MICROGEL

Agarose microgels were assembled using the absorbing micro-transporters as a proof-of-concept of the transportation of cell-laden microgel constructs (Fig. 4-15).

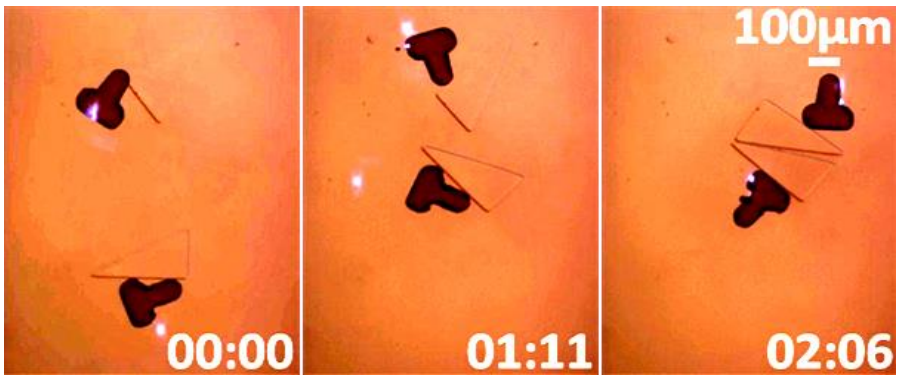

Fig. 4-15 Parallel, cooperative assembly of two triangular agarose microgels by A-HMDO. The time stamp format is m : s.

Triangular agarose (3%, Sigma Aldrich, Type IX-A) microgels were fabricated according to the method described in Section 4.1.7. The triangular agarose has the same dimension as that in Section 2.5. Two Type 1 A-HMDOs were used to transport the agarose microgels in parallel and independently. To enable the operation, an additional laser was added to the setup so that the two lasers projected obliquely onto the glass microscope slide. Each laser was operated by a separate person, addressing a single A-HMDO. The users coordinated A-HMDO movements to arrange two triangular agarose hydrogels into a rectangular shape (Fig. 4-15). The maximum transportation velocity in straight line was 6 μm/s, as the microgels are larger than polystyrene beads and yeasts. To achieve a higher transportation speed, lower-molecular-weight PEGDA forms a more robust hydrogel [116], which permits using longer laser pulse widths for stronger actuation forces.

CHAPTER. 5 CONCLUSION AND FUTURE WORK

5.1 SUMMARY OF OFB MICRO-TRANSPORTATION

In this dissertation, opto-thermocapillary flow-addressed bubbles (OFB) were engineered to be a tool for biological micro-transportation. The OFB does not rely on the magnetic, optical, or electrical properties of the micro-objects to achieve micro-transportation, so the penetration of harmful fields through the micro-object can be avoided. Additionally, the OFB can be generated and eliminated on demand inside liquid media, without the need for micro-fabrication or the introduction of extra materials into the working space.

By using OFB, various micro-objects have been transported and patterned. Its resolution can go down to single cell level (Section 3.5.5). And the transportation force can go up to 14 nN when transporting the glass microebeads (Section 3.3.1). With such ability, cell laden microgels and single cell were patterning in medium or directly inside hydrogel pre-polymers. After being patterned, cells shows a high viability rate or an ability to spread and proliferate, demonstrating the biocompatibility of the OFB.

5.2 FUTURE WORK

5.2.1 OFB WITHOUT THE ABSORBING SUBSTRATE

Although currently the OFB requiring absorbing material for bubble generation, it is inexpensive, commercially available, and biocompatible. Such reliance is also no longer necessary if femtosecond-laser (fs-laser) is induced. Using a fs-laser, the bubble can be generated and actuated by heat from nonlinear absorption [74][83]. This removes the need for optically absorbing materials, which may expand the compatibility of OFB with many types of substrates, including general bio-medical containers or carrier wares such as cell culture flasks, petri dishes, and well plates.

5.2.2 IMPROVEMENT ON CELLULAR PATTERNING

In order to be qualified for general biological micro-transportation, the micro-transportation by OFB has to be tested in more media. Since the thermocapillary flow depends on the surface tension variation on the gas-liquid interface, the presence of surfactants can affect the direction and scale of the flow [117]. Surfactants are present in many cell culture media [118], so their effects should be considered in the future.

In order to make functional *in vitro* tissue, cells have to be able to survive and preferably proliferate inside a bio-matrix [119]. Agarose/collagen beads have been proved to support cell proliferation (Section 3.4.3). Other recently developed hydrogels such as gelatin methacrylate (GelMA) [120] would also be an ideal biomatrix. In addition, the GelMA pre-polymer has a low viscosity, enabling a faster transportation velocity compared to agarose/collagen pre-polymers.

Finally, the mammalian cells that were used here were fibroblast cell lines, chosen for their ease of use and popularity as a model cell in tissue engineering [cite some other papers that use 3T3 cells]. However, other cells besides fibroblasts also have to be patterned since functional organs are usually composed of many co-located cells [104].

5.2.3 PARALLEL AND COOPERATIVE MICRO-TRANSPORTATION

Currently, more than two OFBs have been demonstrated in silicone oil using modulated light beams from the projector (Section 2.7). Two lasers were also used to prove the concept of parallel OFB actuation in water (Section 3.3.4). However, these demonstrations have not pushed the limits of what is possible using optically controlled actuation. To increase the amount of parallel actuation, experimental setups that use a spatial light modulator or scanning mirror are currently under development. By using these two light beam modulation devices, more OFBs are expected to work in parallel and cooperatively inside water based medium. For example, in the OFB single cell transporter, the pulse width currently used (less than 20 μs) is far smaller than the pulse period (greater than 1ms), making it possible to run more than one hundred transportation cases in parallel by using a scanning mirror to direct the laser to different cells within a single period, effectively achieving time-division multiplexing.

When the system capable of addressing multiple OFB is available, the OFB can be tracked by computer vision [50]. With the further help from the robotics control research, such swarm robotics control [121], the OFB based transportation may turn into a fully automated setup. If achieved, desired patterning may be finished by defining final pattern in a CAD software and adding micro-objects into the working space.

5.2.4 3D MICRO-TRANSPORTATION

Currently, the micro-transportation here is two-dimensional. Three-dimensional micro-transportation can make fabrication of *in vitro* tissue with multiple layers possible [37]. However, three-dimensional transportation means the OFB has to move away from the absorbing substrate. Without the help absorbing substrate, the temperature gradient necessary for thermocapillary flow can only be generated by heating the medium or the gas within the bubble [74]. Heating of the medium may adversely affect the bio-micro-objects. Moreover, the heated region has to be under the OFB to counteract the buoyancy force, which means that moving the OFB down to the substrate is challenging. In a preliminary experiment inside silicone oil, a 100-µm-diameter OFB can be addressed in the vertical direction by a 1480-nm laser (400mW, JDSU) when it is 100 µm above a substrate consisting of a standard glass microscope slide. However, the OFB could not be brought into contact with the glass substrate. This is probably due to the depletion of the liquid when the bubble is closer to the substrate, causing less liquid to be heated by the laser (in this system, the laser is absorbed by the liquid, so it directly heats the medium). The decreasing thickness of the liquid layer beneath the OFB and the corresponding loss of heating creates a dead zone that is unreachable by the OFB. Based on these findings, the second method proposed here, directly heating the gas inside the bubble, will be explored in the future.

To transport micro-objects in three dimensions, physical contact transportation can be realized by grasping the micro-objects with multiple bubbles. This requires simultaneous actuation of multiple bubbles, which should be done in parallel with the parallel OFB transportation research (Section 2.7, Section 3.3.4). In addition, non-contact transportation through hydrodynamic flow may also be possible since the convection around the OFB is intrinsically three dimensional, as described in Fig. 3-14.

Finally, the A-HMDO distinguishes itself by its independence from the absorbing substrate. Thus, if A-HMDO fabrication is improved such that OFB generation at the bottom surface of the A-HMDO is possible, it may use the same actuation mechanism as HMDO (Section 4.2.3) to achieve motion in the vertical direction. The OFB at the bottom of the A-HMDO may be able to lift it up and enable movement in 3D.

5.2.5 EXTRA FUNCTIONS

Micro-transportation is only one part of the bio-micromanipulation, which contains many other operations such as cell surgery [122] and sensing [25]. Thus, equipping the OFB with more functions can widen its bio-medical applications.

Cell poration is a cell membrane permeability modification process. The purpose is to deliver exogenous molecules into the cell plasma and modify cell behavior [123]. Poration has been achieved using ultrasound (sonoporation) [124] and electrical fields (electroporation) [125]. In sonoporation, ultrasound-excited bubbles create pores on the surrounding cells [124]. This function may be added to OFB by supplying an acoustic signal. In addition to these two methods, the fluidic flow around a cavitation bubble generated by femtosecond laser is also able to porate the cell [126]. Since the position of the bubble generation can be accurately selected, this mechanism can achieve single-cell poration resolution. It has been found that the fluidic flow around the OFB has similar ability, and this system is currently under development [127].

The hydrogel structure of HMDO provides a safe way to physically contact cell membranes. Such contact may be used to explore the mechanical properties of cell membranes, which is important method of differentiating abnormal cells [25]. For this purpose, the HMDO surface can also be functionalized by different bio-molecules to better interact with the cell membrane. Further, other molecules can be attached to the HMDO surface to sense biological processes in the microscale.

BIBLIOGRAPHY

[1] E. B. Steager, M. Selman Sakar, C. Magee, M. Kennedy, A. Cowley, and V. Kumar, "Automated biomanipulation of single cells using magnetic microrobots," *Int. J. Rob. Res.*, vol. 32, no. 3, pp. 346–359, Mar. 2013.

[2] Polysciences Inc, "2014 Polysciences Catalog." [Online]. Available: http://www.polysciences.com/.

[3] P. Zorlutuna, N. Annabi, G. Camci-Unal, M. Nikkhah, J. M. Cha, J. W. Nichol, A. Manbachi, H. Bae, S. Chen, and A. Khademhosseini, "Microfabricated biomaterials for engineering 3D tissues.," *Adv. Mater.*, vol. 24, no. 14, pp. 1782–804, Apr. 2012.

[4] X. Ding, S.-C. S. Lin, B. Kiraly, H. Yue, S. Li, I.-K. Chiang, J. Shi, S. J. Benkovic, and T. J. Huang, "On-chip manipulation of single microparticles, cells, and organisms using surface acoustic waves.," *Proc. Natl. Acad. Sci. U. S. A.*, vol. 109, no. 28, pp. 11105–9, Jul. 2012.

[5] B. F. Brehm-Stecher and E. A. Johnson, "Single-cell microbiology: tools, technologies, and applications.," *Microbiol. Mol. Biol. Rev.*, vol. 68, no. 3, pp. 538–59, Sep. 2004.

[6] J. S. Liu and Z. J. Gartner, "Directing the assembly of spatially organized multicomponent tissues from the bottom up.," *Trends Cell Biol.*, vol. 22, no. 12, pp. 683–91, Dec. 2012.

[7] E. B. Steager, M. Selman Sakar, C. Magee, M. Kennedy, a. Cowley, and V. Kumar, "Automated biomanipulation of single cells using magnetic microrobots," *Int. J. Rob. Res.*, vol. 32, no. 3, pp. 346–359, Mar. 2013.

[8] K. R. Love, S. Bagh, J. Choi, and J. C. Love, "Microtools for single-cell analysis in biopharmaceutical development and manufacturing.," *Trends Biotechnol.*, vol. 31, no. 5, pp. 280–6, May 2013.

[9] D. Huh, B. D. Matthews, A. Mammoto, M. Montoya-Zavala, H. Y. Hsin, and D. E. Ingber, "Reconstituting organ-level lung functions on a chip.," *Science*, vol. 328, no. 5986, pp. 1662–8, Jun. 2010.

[10] Pharmaceutical Research and Manufactureres of America, "2013 Biopharmaceutical Research Industry Profile," Washington, DC, 2011.

[11] E. J. Suuronen, H. Sheardown, K. D. Newman, C. R. McLaughlin, and M. Griffith, "Building in vitro models of organs.," *Int. Rev. Cytol.*, vol. 244, pp. 137–73, Jan. 2005.

[12] Y. Ling, J. Rubin, Y. Deng, C. Huang, U. Demirci, J. M. Karp, and A. Khademhosseini, "A cell-laden microfluidic hydrogel.," *Lab Chip*, vol. 7, no. 6, pp. 756–62, Jun. 2007.

[13] J. Ramón-Azcón, S. Ahadian, R. Obregón, G. Camci-Unal, S. Ostrovidov, V. Hosseini, H. Kaji, K. Ino, H. Shiku, A. Khademhosseini, and T. Matsue, "Gelatin methacrylate as a promising hydrogel for 3D microscale organization and proliferation of dielectrophoretically patterned cells.," *Lab Chip*, vol. 12, no. 16, pp. 2959–69, Aug. 2012.

[14] T. Billiet, M. Vandenhaute, J. Schelfhout, S. Van Vlierberghe, and P. Dubruel, "A review of trends and limitations in hydrogel-rapid prototyping for tissue engineering.," *Biomaterials*, vol. 33, no. 26, pp. 6020–41, Sep. 2012.

[15] Y. T. Matsunaga, Y. Morimoto, and S. Takeuchi, "Molding cell beads for rapid construction of macroscopic 3D tissue architecture.," *Adv. Mater.*, vol. 23, no. 12, pp. H90–4, Mar. 2011.

[16] C. J. Ferris, K. G. Gilmore, G. G. Wallace, and M. In het Panhuis, "Biofabrication: an overview of the approaches used for printing of living cells.," *Appl. Microbiol. Biotechnol.*, vol. 97, no. 10, pp. 4243–58, May 2013.

[17] J. Yeh, Y. Ling, J. M. Karp, J. Gantz, A. Chandawarkar, G. Eng, J. Blumling, R. Langer, and A. Khademhosseini, "Micromolding of shape-controlled,

harvestable cell-laden hydrogels.," *Biomaterials*, vol. 27, no. 31, pp. 5391–8, Nov. 2006.

[18] X. Liu, R. Fernandes, A. Jurisicova, R. F. Casper, and Y. Sun, "In situ mechanical characterization of mouse oocytes using a cell holding device.," *Lab Chip*, vol. 10, no. 16, pp. 2154–61, Aug. 2010.

[19] U. Mirsaidov, J. Scrimgeour, W. Timp, K. Beck, M. Mir, P. Matsudaira, and G. Timp, "Live cell lithography: using optical tweezers to create synthetic tissue.," *Lab Chip*, vol. 8, no. 12, pp. 2174–81, Dec. 2008.

[20] M. Tanase, N. Biais, and M. Sheetz, "Magnetic tweezers in cell biology.," *Methods Cell Biol.*, vol. 83, pp. 473–93, Jan. 2007.

[21] M. C. Wu, "Optoelectronic tweezers," *Nat. Photonics*, vol. 5, no. 6, pp. 322–324, Jun. 2011.

[22] J. F. Schenck, "Safety of strong, static magnetic fields.," *J. Magn. Reson. Imaging*, vol. 12, pp. 2–19, 2000.

[23] R. Blakemore, "Magnetotactic bacteria," *Science (80-.).*, vol. 190, no. 4212, pp. 377–379, Oct. 1975.

[24] S. Martel, M. Mohammadi, O. Felfoul, Zhao Lu, and P. Pouponneau, "Flagellated Magnetotactic Bacteria as Controlled MRI-trackable Propulsion and Steering Systems for Medical Nanorobots Operating in the Human Microvasculature," *Int. J. Rob. Res.*, vol. 28, pp. 571–582, Apr. 2009.

[25] D.-H. Kim, P. K. Wong, J. Park, A. Levchenko, and Y. Sun, "Microengineered platforms for cell mechanobiology.," *Annu. Rev. Biomed. Eng.*, vol. 11, pp. 203–33, Jan. 2009.

[26] A. Ashkin, "Acceleration and Trapping of Particles by Radiation Pressure," *Phys. Rev. Lett.*, vol. 24, no. 4, pp. 156–159, Jan. 1970.

[27] S. K. Mohanty, A. Rapp, S. Monajembashi, P. K. Gupta, and K. O. Greulich, "Comet assay measurements of DNA damage in cells by laser microbeams and

trapping beams with wavelengths spanning a range of 308 nm to 1064 nm.," *Radiat. Res.*, vol. 157, no. 4, pp. 378–85, Apr. 2002.

[28] G. Thalhammer, R. Steiger, S. Bernet, and M. Ritsch-Marte, "Optical macro-tweezers: trapping of highly motile micro-organisms," *J. Opt.*, vol. 13, no. 4, p. 044024, Apr. 2011.

[29] R. Bowman, A. Jesacher, G. Thalhammer, G. Gibson, M. Ritsch-Marte, and M. Padgett, "Position clamping in a holographic counterpropagating optical trap.," *Opt. Express*, vol. 19, no. 10, pp. 9908–14, May 2011.

[30] A. Ashkin, J. M. Dziedzic, J. E. Bjorkholm, and S. Chu, "Observation of a single-beam gradient force optical trap for dielectric particles," *Opt. Lett.*, vol. 11, no. 5, p. 288, May 1986.

[31] H. Zhang and K.-K. Liu, "Optical tweezers for single cells.," *J. R. Soc. Interface*, vol. 5, no. 24, pp. 671–90, Jul. 2008.

[32] F. Arai, K. Onda, R. Iitsuka, and H. Maruyama, "Multi-beam laser micromanipulation of microtool by integrated optical tweezers," *2009 IEEE Int. Conf. Robot. Autom.*, pp. 1832–1837, May 2009.

[33] S. Chowdhury, A. Thakur, P. Svec, C. Wang, W. Losert, and S. K. Gupta, "Automated Manipulation of Biological Cells Using Gripper Formations Controlled By Optical Tweezers," *IEEE Trans. Autom. Sci. Eng.*, pp. 1–10, 2013.

[34] H. Maruyama, R. Iitsuka, K. Onda, and F. Arai, "Massive parallel assembly of microbeads for fabrication of microtools having spherical structure and powerful laser manipulation," in *2010 IEEE International Conference on Robotics and Automation*, 2010, pp. 482–487.

[35] D. G. Grier, "A revolution in optical manipulation.," *Nature*, vol. 424, no. 6950, pp. 810–6, Aug. 2003.

[36] R. Pethig, "Review article-dielectrophoresis: status of the theory, technology, and applications.," *Biomicrofluidics*, vol. 4, no. 2, pp. 1–36, Jan. 2010.

[37] D. R. Albrecht, G. H. Underhill, T. B. Wassermann, R. L. Sah, and S. N. Bhatia, "Probing the role of multicellular organization in three-dimensional microenvironments.," *Nat. Methods*, vol. 3, no. 5, pp. 369–75, May 2006.

[38] D. R. Albrecht, G. H. Underhill, A. Mendelson, and S. N. Bhatia, "Multiphase electropatterning of cells and biomaterials.," *Lab Chip*, vol. 7, no. 6, pp. 702–9, Jun. 2007.

[39] N. Manaresi, a. Romani, G. Medoro, L. Altomare, a. Leonardi, M. Tartagni, and R. Guerrieri, "A cmos chip for individual cell manipulation and detection," *IEEE J. Solid-State Circuits*, vol. 38, no. 12, pp. 2297–2305, Dec. 2003.

[40] T. Honegger and D. Peyrade, "Moving pulsed dielectrophoresis.," *Lab Chip*, vol. 13, no. 8, pp. 1538–45, Apr. 2013.

[41] S.-M. Yang, T.-M. Yu, H.-P. Huang, M.-Y. Ku, S.-Y. Tseng, C.-L. Tsai, H.-P. Chen, L. Hsu, and C.-H. Liu, "Light-driven manipulation of picobubbles on a titanium oxide phthalocyanine-based optoelectronic chip," *Appl. Phys. Lett.*, vol. 98, no. 15, p. 153512, 2011.

[42] P. Y. Chiou, A. T. Ohta, and M. C. Wu, "Massively parallel manipulation of single cells and microparticles using optical images," *Nature*, vol. 436, no. 7049, pp. 370–372, Jul. 2005.

[43] J. Voldman, "Electrical forces for microscale cell manipulation.," *Annu. Rev. Biomed. Eng.*, vol. 8, pp. 425–54, Jan. 2006.

[44] J. K. Valley, A. Jamshidi, A. T. Ohta, H.-Y. Hsu, and M. C. Wu, "Operational Regimes and Physics Present in Optoelectronic Tweezers," *J. Microelectromechanical Syst.*, vol. 17, no. 2, pp. 342–350, Apr. 2008.

[45] H. Hsu, A. T. Ohta, P.-Y. Chiou, A. Jamshidi, S. L. Neale, and M. C. Wu, "Phototransistor-based optoelectronic tweezers for dynamic cell manipulation in cell culture media.," *Lab Chip*, vol. 10, no. 2, pp. 165–72, Jan. 2010.

[46] G. Zhao, C. L. Teo, D. W. Hutmacher, and E. Burdet, "Force-controlled automatic microassembly of tissue engineering scaffolds," *J. Micromechanics Microengineering*, vol. 20, no. 3, p. 035001, Mar. 2010.

[47] Z. Lu, C. Moraes, G. Ye, C. a Simmons, and Y. Sun, "Single cell deposition and patterning with a robotic system.," *PLoS One*, vol. 5, no. 10, p. e13542, Jan. 2010.

[48] D. J. Cappelleri, Z. Fu, and M. Fatovic, "Caging for 2D and 3D micromanipulation," *J. Micro-Nano Mechatronics*, vol. 7, no. 4, pp. 115–129, Nov. 2012.

[49] A. J. Petruska and J. J. Abbott, "Optimal Permanent-Magnet Geometries for Dipole Field Approximation," *IEEE Trans. Magn.*, vol. 49, no. 2, pp. 811–819, Feb. 2013.

[50] E. Diller, "Micro-Scale Mobile Robotics," *Found. Trends Robot.*, vol. 2, no. 3, pp. 143–259, 2011.

[51] C. Pawashe, S. Floyd, and M. Sitti, "Modeling and Experimental Characterization of an Untethered Magnetic Micro-Robot," *Int. J. Rob. Res.*, vol. 28, no. 8, pp. 1077–1094, Jul. 2009.

[52] D. R. Frutiger, K. Vollmers, B. E. Kratochvil, and B. J. Nelson, "Small, Fast, and Under Control: Wireless Resonant Magnetic Micro-agents," *Int. J. Rob. Res.*, vol. 29, no. 5, pp. 613–636, Nov. 2009.

[53] M. P. Kummer, J. J. Abbott, B. E. Kratochvil, R. Borer, A. Sengul, and B. J. Nelson, "OctoMag: An Electromagnetic System for 5-DOF Wireless Micromanipulation," *IEEE Trans. Robot.*, vol. 26, 2010.

[54] M. S. Sakar, E. B. Steager, A. Cowley, V. Kumar, and G. J. Pappas, "Wireless manipulation of single cells using magnetic microtransporters," in *2011 IEEE International Conference on Robotics and Automation*, 2011, pp. 2668–2673.

[55] S. Tottori, L. Zhang, F. Qiu, K. K. Krawczyk, A. Franco-Obregón, and B. J. Nelson, "Magnetic helical micromachines: fabrication, controlled swimming, and cargo transport.," *Adv. Mater.*, vol. 24, no. 6, pp. 811–6, Feb. 2012.

[56] S. Earnshaw, "On the nature of the molecular forces which regulate the constitution of the luminiferous ether," *Trans. Camb. Phil. Soc*, vol. 7, pp. 97–112.

[57] E. Diller, S. Floyd, C. Pawashe, and M. Sitti, "Control of Multiple Heterogeneous Magnetic Microrobots in Two Dimensions on Nonspecialized Surfaces," *Robot. IEEE Trans.*, vol. 28, no. 1, pp. 172–182, Feb. 2012.

[58] H. Lee, Y. Liu, D. Ham, and R. M. Westervelt, "Integrated cell manipulation system--CMOS/microfluidic hybrid.," *Lab Chip*, vol. 7, no. 3, pp. 331–7, Mar. 2007.

[59] A. Ichikawa, A. Honda, M. Ejima, T. Tanikawa, F. Arai, and T. Fukuda, "In-situ formation of a gel microbead for laser micromanipulation of microorganisms, DNA and virus," in *2006 IEEE International Symposium on MicroNanoMechanical and Human Science*, 2006, pp. 1–6.

[60] D. Kim, A. Liu, E. Diller, and M. Sitti, "Chemotactic steering of bacteria propelled microbeads BT - Bio-Hybrid Systems and Living Machines," *Biomed. Microdevices*, vol. 14, no. 6, pp. 1009–1017, Dec. 2012.

[61] E. B. Steager, a. Agung Julius, M. Kim, V. Kumar, and G. J. Pappas, "Modeling, control and experimental characterization of microbiorobots," *Int. J. Rob. Res.*, vol. 30, no. 6, pp. 647–658, Jan. 2011.

[62] S. Floyd, C. Pawashe, and M. Sitti, "Two-dimensional contact and noncontact micromanipulation in liquid using an untethered mobile magnetic microrobot," *IEEE Trans. Robot.*, vol. 25, no. 6, pp. 1332–1342, Dec. 2009.

[63] J. H. Lee, K. H. Lee, J. B. Chae, K. Rhee, and S. K. Chung, "On-chip micromanipulation by AC-EWOD driven twin bubbles," *Sensors Actuators A Phys.*, vol. 195, pp. 167–174, Jun. 2013.

[64] X. Ding, J. Shi, S.-C. S. Lin, S. Yazdi, B. Kiraly, and T. J. Huang, "Tunable patterning of microparticles and cells using standing surface acoustic waves.," *Lab Chip*, vol. 12, no. 14, pp. 2491–7, Jul. 2012.

[65] Y. Zhao, "Micro bubble manipulation towards single cell handling tool," in *2005 IEEE International Conference on Robotics and Biomimetics - ROBIO*, 2005, vol. 1, pp. 269–273.

[66] S. K. Chung and S. K. Cho, "On-chip manipulation of objects using mobile oscillating bubbles," *J. Micromechanics Microengineering*, vol. 18, no. 12, p. 125024, Dec. 2008.

[67] S. K. Chung and S. K. Cho, "3-D manipulation of millimeter- and micro-sized objects using an acoustically excited oscillating bubble," *Microfluid. Nanofluidics*, vol. 6, no. 2, pp. 261–265, Jul. 2008.

[68] S. K. Chung, J. O. Kwon, and S. K. Cho, "Manipulation of Micro/Mini-objects by AC-Electrowetting-Actuated Oscillating Bubbles: Capturing, Carrying and Releasing," *J. Adhes. Sci. Technol.*, vol. ahead-of-p, no. ahead-of-print, pp. 1–19, Jan. 2012.

[69] A. Hashmi, G. Yu, M. Reilly-Collette, G. Heiman, and J. Xu, "Oscillating bubbles: a versatile tool for lab on a chip applications.," *Lab Chip*, vol. 12, no. 21, pp. 4216–27, Nov. 2012.

[70] S. K. Chung, Y. Zhao, and S. K. Cho, "On-chip creation and elimination of microbubbles for a micro-object manipulator," *J. Micromechanics Microengineering*, vol. 18, no. 9, p. 095009, Sep. 2008.

[71] Y. Xie, C. Zhao, Y. Zhao, S. Li, J. Rufo, S. Yang, F. Guo, and T. J. Huang, "Optoacoustic tweezers: a programmable, localized cell concentrator based on opto-thermally generated, acoustically activated, surface bubbles.," *Lab Chip*, vol. 13, no. 9, pp. 1772–9, May 2013.

[72] E. Diller, Z. Ye, and M. Sitti, "Rotating magnetic micro-robots for versatile non-contact fluidic manipulation of micro-objects BT - 2011 IEEE/RSJ International

Conference on Intelligent Robots and Systems: Celebrating 50 Years of Robotics, IROS'11, September 25, 2011 - September 30, 20," 2011, pp. 1291–1296.

[73] Z. Ye, E. Diller, and M. Sitti, "Micro-manipulation using rotational fluid flows induced by remote magnetic micro-manipulators," *J. Appl. Phys.*, vol. 112, no. 6, pp. 64912–64917, 2012.

[74] S. V. Oshemkov, L. P. Dvorkin, and V. Y. Dmitriev, "Trapping and manipulating gas bubbles in water with ultrashort laser pulses at a high repetition rate," *Tech. Phys. Lett.*, vol. 35, no. 3, pp. 282–285, Mar. 2009.

[75] S. K. Chung, K. Rhee, and S. K. Cho, "Bubble actuation by electrowetting-on-dielectric (EWOD) and its applications: A review," *Int. J. Precis. Eng. Manuf.*, vol. 11, no. 6, pp. 991–1006, Dec. 2010.

[76] Z. R. Gagnon and H.-C. Chang, "Dielectrophoresis of ionized gas microbubbles: Dipole reversal due to diffusive double-layer polarization," *Appl. Phys. Lett.*, vol. 93, no. 22, p. 224101, 2008.

[77] P. H. Jones, E. Stride, and N. Saffari, "Trapping and manipulation of microscopic bubbles with a scanning optical tweezer," *Appl. Phys. Lett.*, vol. 89, no. 8, p. 081113, 2006.

[78] B. L. Lü, Y. Q. Li, H. Ni, and Y. Z. Wang, "Laser-induced hybrid trap for micro-bubbles," *Appl. Phys. B*, vol. 71, no. 6, pp. 801–805, Dec. 2000.

[79] R. S. Subramanian and R. Balasubramaniam, *The Motion of Bubbles and Drops in Reduced Gravity*. Cambridge, UK: Cambridge University Press, 2001, p. 18.

[80] W. Hu, K. S. Ishii, and A. T. Ohta, "Micro-assembly using optically controlled bubble microrobots," *Appl. Phys. Lett.*, vol. 99, p. 094103, 2011.

[81] B. K. Larkin, "Thermocapillary flow around hemispherical bubble," *AIChE J.*, vol. 16, no. 1, pp. 101–107, Jan. 1970.

[82] R. S. Subramanian, "Motion of Drops and Bubbles in Reduced Gravity," *Ind. Eng. Chem. Res.*, vol. 34, no. 10, pp. 3411–3416, Oct. 2006.

[83] N. A. Ivanova and B. A. Bezuglyĭ, “Optical thermocapillary bubble trap,” *Tech. Phys. Lett.*, vol. 32, no. 10, pp. 854–856, Oct. 2006.

[84] A. T. Ohta, A. Jamshidi, J. K. Valley, H.-Y. Hsu, and M. C. Wu, “Optically actuated thermocapillary movement of gas bubbles on an absorbing substrate,” *Appl. Phys. Lett.*, vol. 91, no. 7, p. 074103, 2007.

[85] Y. Zheng, H. Liu, Y. Wang, C. Zhu, S. Wang, J. Cao, and S. Zhu, “Accumulating microparticles and direct-writing micropatterns using a continuous-wave laser-induced vapor bubble.,” *Lab Chip*, vol. 11, no. 22, pp. 3816–20, Nov. 2011.

[86] R. Selver, “Experiments on the transition from the steady to the oscillatory marangoni convection of a floating-zone under various cold wall temperatures and various ambient air temperature effects,” *Microgravity - Sci. Technol.*, vol. 17, no. 4, pp. 25–35, Dec. 2005.

[87] W. M. Haynes, Ed., *CRC Handbook of Chemistry and Physics*. Boca Raton, Florida: CRC Press, 2011.

[88] “Processing.org.” [Online]. Available: http://processing.org/. [Accessed: 16-Sep-2011].

[89] Y. Du, E. Lo, M. K. Vidula, M. Khabiry, and A. Khademhosseini, “Method of Bottom-Up Directed Assembly of Cell-Laden Microgels.,” *Cell. Mol. Bioeng.*, vol. 1, no. 2, pp. 157–162, Jan. 2008.

[90] Y. Du, E. Lo, S. Ali, and A. Khademhosseini, “Directed assembly of cell-laden microgels for fabrication of 3D tissue constructs.,” *Proc. Natl. Acad. Sci. U. S. A.*, vol. 105, no. 28, pp. 9522–7, Jul. 2008.

[91] A. Batorsky, J. Liao, A. W. Lund, G. E. Plopper, and J. P. Stegemann, “Encapsulation of adult human mesenchymal stem cells within collagen-agarose microenvironments.,” *Biotechnol. Bioeng.*, vol. 92, no. 4, pp. 492–500, Nov. 2005.

[92] 3M Electronics Markets Materials Division, "Product Information for Fluorinert Electronic Liquid FC-40," 2010.

[93] R. W. Bowman, G. Gibson, D. Carberry, L. Picco, M. Miles, and M. J. Padgett, "iTweezers: optical micromanipulation controlled by an Apple iPad," *J. Opt.*, vol. 13, no. 4, p. 044002, Apr. 2011.

[94] M.-H. Tan, J. S. Dover, T.-S. Hsu, K. a Arndt, and B. Stewart, "Clinical evaluation of enhanced nonablative skin rejuvenation using a combination of a 532 and a 1,064 nm laser.," *Lasers Surg. Med.*, vol. 34, no. 5, pp. 439–45, Jan. 2004.

[95] I. H. Fine, M. Packer, and R. S. Hoffman, "New phacoemulsification technologies," *J. Cataract Refract. Surg.*, vol. 28, no. 6, pp. 1054–1060, Jun. 2002.

[96] S. S. Shah, M. C. Howland, L.-J. Chen, J. Silangcruz, S. V Verkhoturov, E. a Schweikert, A. N. Parikh, and A. Revzin, "Micropatterning of proteins and mammalian cells on indium tin oxide.," *ACS Appl. Mater. Interfaces*, vol. 1, no. 11, pp. 2592–601, Nov. 2009.

[97] T. Kawahara, M. Sugita, M. Hagiwara, F. Arai, H. Kawano, I. Shihira-Ishikawa, and A. Miyawaki, "On-chip microrobot for investigating the response of aquatic microorganisms to mechanical stimulation.," *Lab Chip*, vol. 13, no. 6, pp. 1070–8, Feb. 2013.

[98] S. Lan, M. Veiseh, and M. Zhang, "Surface modification of silicon and gold-patterned silicon surfaces for improved biocompatibility and cell patterning selectivity," *Biosens. Bioelectron.*, vol. 20, pp. 1697–1708, Mar. 2005.

[99] K. Vollmers, D. R. Frutiger, B. E. Kratochvil, and B. J. Nelson, "Wireless resonant magnetic microactuator for untethered mobile microrobots," *Appl. Phys. Lett.*, vol. 92, p. 144103, 2008.

[100] S. E. Chung, W. Park, H. Park, K. Yu, N. Park, and S. Kwon, "Optofluidic maskless lithography system for real-time synthesis of photopolymerized

microstructures in microfluidic channels," *Appl. Phys. Lett.*, vol. 91, no. 4, p. 041106, 2007.

[101] A. P. McGuigan, D. a Bruzewicz, A. Glavan, M. J. Butte, M. Butte, and G. M. Whitesides, "Cell encapsulation in sub-mm sized gel modules using replica molding.," *PLoS One*, vol. 3, no. 5, p. e2258, Jan. 2008.

[102] K. Haubert, T. Drier, and D. Beebe, "PDMS bonding by means of a portable, low-cost corona system.," *Lab Chip*, vol. 6, no. 12, pp. 1548–9, Dec. 2006.

[103] J. Yeh, Y. Ling, J. M. Karp, J. Gantz, A. Chandawarkar, G. Eng, J. Blumling, R. Langer, and A. Khademhosseini, "Micromolding of shape-controlled, harvestable cell-laden hydrogels.," *Biomaterials*, vol. 27, no. 31, pp. 5391–8, Nov. 2006.

[104] M. Okochi, T. Matsumura, and H. Honda, "Magnetic force-based cell patterning for evaluation of the effect of stromal fibroblasts on invasive capacity in 3Dcultures.," *Biosens. Bioelectron.*, vol. 42, pp. 300–7, Apr. 2013.

[105] J. T. Keane, D. Ryan, and P. P. Gray, "Effect of shear stress on expression of a recombinant protein by Chinese hamster ovary cells.," *Biotechnol. Bioeng.*, vol. 81, no. 2, pp. 211–20, Jan. 2003.

[106] S. Kobayashi, S. D. Crooks, and D. M. Eckmann, "In vitro surfactant mitigation of gas bubble contact-induced endothelial cell death.," *Undersea Hyperb. Med.*, vol. 38, no. 1, pp. 27–39, Aug. 1988.

[107] S. M. O'Shaughnessy and A. J. Robinson, "Numerical investigation of bubble-induced Marangoni convection.," *Ann. N. Y. Acad. Sci.*, vol. 1161, pp. 304–20, Apr. 2009.

[108] G. Fundueanu, M. Constantin, and P. Ascenzi, "Poly(N-isopropylacrylamide-co-acrylamide) cross-linked thermoresponsive microspheres obtained from preformed polymers: Influence of the physico-chemical characteristics of drugs on their release profiles.," *Acta Biomater.*, vol. 5, no. 1, pp. 363–73, Jan. 2009.

[109] D. Lauffenburger, C. Rothman, and S. H. Zigmond, "Measurement of leukocyte motility and chemotaxis parameters with a linear under-agarose migration assay.," *J. Immunol.*, vol. 131, no. 2, pp. 940–7, Aug. 1983.

[110] A. Mendelson, Y. K. Cheung, K. Paluch, M. Chen, K. Kong, J. Tan, Z. Dong, S. K. Sia, and J. J. Mao, "Competitive stem cell recruitment by multiple cytotactic cues.," *Lab Chip*, Jan. 2013.

[111] L. N. Kim, S.-E. Choi, J. Kim, H. Kim, and S. Kwon, "Single exposure fabrication and manipulation of 3D hydrogel cell microcarriers.," *Lab Chip*, vol. 11, no. 1, pp. 48–51, Jan. 2011.

[112] M. S. Sakar, E. B. Steager, A. Cowley, V. Kumar, and G. J. Pappas, "Wireless manipulation of single cells using magnetic microtransporters," in *2011 IEEE International Conference on Robotics and Automation*, 2011, pp. 2668–2673.

[113] B. a Shatz, L. B. Weinstock, P. E. Swanson, and E. P. Thyssen, "Long-term safety of India ink tattoos in the colon.," *Gastrointest. Endosc.*, vol. 45, no. 2, pp. 153–6, Feb. 1997.

[114] J. Wang and W. Gao, "Nano/Microscale motors: biomedical opportunities and challenges.," *ACS Nano*, vol. 6, no. 7, pp. 5745–51, Jul. 2012.

[115] Y. Noguchi, K. Okeyoshi, and R. Yoshida, "Design of Surfactant-Grafted Hydrogels with Fast Response to Temperature," *Macromol. Rapid Commun.*, vol. 26, no. 24, pp. 1913–1917, Dec. 2005.

[116] J. P. Mazzoccoli, D. L. Feke, H. Baskaran, and P. N. Pintauro, "Mechanical and cell viability properties of crosslinked low- and high-molecular weight poly(ethylene glycol) diacrylate blends.," *J. Biomed. Mater. Res. A*, vol. 93, no. 2, pp. 558–66, May 2010.

[117] K. T. Kotz, K. A. Noble, and G. W. Faris, "Optical microfluidics," *Appl. Phys. Lett.*, vol. 85, no. 13, p. 2658, 2004.

[118] S. Zhang, A. Handa-Corrigan, and R. E. Spier, “Foaming and media surfactant effects on the cultivation of animal cells in stirred and sparged bioreactors,” *J. Biotechnol.*, vol. 25, no. 3, pp. 289–306, Sep. 1992.

[119] J. W. Nichol, S. T. Koshy, H. Bae, C. M. Hwang, S. Yamanlar, and A. Khademhosseini, “Cell-laden microengineered gelatin methacrylate hydrogels.,” *Biomaterials*, vol. 31, no. 21, pp. 5536–44, Jul. 2010.

[120] J. Ramón-Azcón, S. Ahadian, R. Obregón, G. Camci-Unal, S. Ostrovidov, V. Hosseini, H. Kaji, K. Ino, H. Shiku, A. Khademhosseini, and T. Matsue, “Gelatin methacrylate as a promising hydrogel for 3D microscale organization and proliferation of dielectrophoretically patterned cells.,” *Lab Chip*, vol. 12, no. 16, pp. 2959–69, Aug. 2012.

[121] L. C. A. Pimenta, N. Michael, R. C. Mesquita, G. A. S. Pereira, and V. Kumar, “Control of swarms based on Hydrodynamic models,” in *2008 IEEE International Conference on Robotics and Automation*, 2008, pp. 1948–1953.

[122] M. Hagiwara, T. Kawahara, L. Feng, Y. Yamanishi, and F. Arai, “High precision magnetically driven microtools with ultrasonic vibration for enucleation of oocytes,” *2010 Int. Symp. Micro-NanoMechatronics Hum. Sci.*, pp. 47–52, Nov. 2010.

[123] S. Lakshmanan, G. K. Gupta, P. Avci, R. Chandran, M. Sadasivam, A. E. S. Jorge, and M. R. Hamblin, “Physical energy for drug delivery; poration, concentration and activation.,” *Adv. Drug Deliv. Rev.*, Jun. 2013.

[124] Z. Fan, H. Liu, M. Mayer, and C. X. Deng, “Spatiotemporally controlled single cell sonoporation.,” *Proc. Natl. Acad. Sci. U. S. A.*, vol. 109, no. 41, pp. 16486–91, Oct. 2012.

[125] A. M. Bodles-Brakhop, R. Heller, and R. Draghia-Akli, “Electroporation for the delivery of DNA-based vaccines and immunotherapeutics: current clinical developments.,” *Mol. Ther.*, vol. 17, no. 4, pp. 585–92, Apr. 2009.

[126] M. Waleed, S.-U. Hwang, J.-D. Kim, I. Shabbir, S.-M. Shin, and Y.-G. Lee, "Single-cell optoporation and transfection using femtosecond laser and optical tweezers.," *Biomed. Opt. Express*, vol. 4, no. 9, pp. 1533–47, Jan. 2013.

[127] Q. Fan, W. Hu, and A. T. Ohta, "Laser-Induced Microbubble Poration of Localized Single Cells," *Lab Chip*, 2014.